



Balkan Journal of Electrical & Computer Engineering

An International Peer Reviewed, Referred, Indexed and Open Access Journal

www.bajece.com

Vol :12

No : 3

Year :2024

ISSN : 2147 - 284X



It is abstracted and indexed in, Index Google Scholarship, the PSCR, Cross ref, DOAJ, Research Bible, Indian Open Access Journals (OAJ), Institutional Repositories (IR), J-Gate (Informatics India), Ulrich's, International Society of Universal Research in Sciences, DRJI, EyeSource, Cosmos Impact Factor, Cite Factor, SIS Scientific Indexing Service, IJIF, iiiFactor. ULAKBİM-TR Dizin.

General Publication Director & Editor-in-Chief
Musa Yılmaz, University of California Riverside, US

Vice Editor
Hamidreza Nazarpouya, Oklahoma State University, US

Scientific Committee
Abhishek Shukla (India)
Abraham Lomi (Indonesia)
Aleksandar Georgiev (Bulgaria)
Arunas Lipnickas (Lithuania)
Audrius Senulis (Lithuania)
Belle R. Upadhyaya (USA)
Brijender Kahanwal (India)
Chandar Kumar Chanda (India)
Daniela Dzhonova-Atanasova (Bulgaria)
Deris Stiawan (Indonesia)
Emel Onal (Turkey)
Emine Ayaz (Turkey)
Enver Hatimi (Kosovo)
Ferhat Sahin (USA)
Gursel Alici (Australia)
Hakan Temeltaş (Turkey)
Ibrahim Akduman (Turkey)
Jan Izykowski (Poland)
Javier Bilbao Landatxe (Spain)
Jelena Dikun (Lithuania)
Karol Kyslan (Slovakia)
Kunihiko Nabeshima (Japan)
Lambros Ekonomou (Greece)
Lazhar Rahmani (Algerie)
Marcel Istrate (Romania)
Marija Eidukeviciute (Lithuania)
Milena Lazarova (Bulgaria)
Muhammad Hadi (Australia)
Muhamed Turkanović (Slovenia)
Mourad Houabes (Algerie)
Murari Mohan Saha (Sweden)
Nick Papanikolaou (Greece)
Okyay Kaynak (Turkey)
Osman Nuri Ucan (Turkey)
Ozgun E. Mustecaplioglu (Turkey)
Padmanaban Sanjeevikumar (India)
Ramazan Caglar (Turkey)
Rumen Popov (Bulgaria)
Tarek Bouktir (Algeria)
Sead Berberovic (Croatia)
Seta Bogosyan (USA)
Savvas G. Vassiliadis (Greece)
Suwarno (Indonesia)
Tulay Adali (USA)
Yogeshwarsing Calleecharan (Mauritius)
YangQuan Chen (USA)
Youcef Soufi (Algeria)

Aim & Scope

The journal publishes original papers in the extensive field of Electrical-Electronics and Computer engineering. It accepts contributions which are fundamental for the development of electrical engineering, computer engineering and its applications, including overlaps to physics. Manuscripts on both theoretical and experimental work are welcome. Review articles and letters to the editors are also included.

Application areas include (but are not limited to): Electrical & Electronics Engineering, Computer Engineering, Software Engineering, Biomedical Engineering, Electrical Power Engineering, Control Engineering, Signal and Image Processing, Communications & Networking, Sensors, Actuators, Remote Sensing, Consumer Electronics, Fiber-Optics, Radar and Sonar Systems, Artificial Intelligence and its applications, Expert Systems, Medical Imaging, Biomedical Analysis and its applications, Computer Vision, Pattern Recognition, Robotics, Industrial Automation.



ISSN: 2147- 284X
Vol: 12
No : 3
Year: Sep 2024

CONTENTS

Research Article

Onur Akar; Estimation of the Effect of Electric Vehicles on the Aging of Distribution Transformers Using Fuzzy Logic, 199-205

Research Article

Zeynep Özpolat, Özal Yıldırım, Murat Karabatak; The Effect of Linear Discriminant Analysis and Quantum Feature Maps on QSVM Performance for Obesity Diagnosis, 206-213

Research Article

Muhammed Cihad Arslanoğlu, Hüseyin Acar, Abdülkadir Albayrak; Face Expression Recognition via transformer-based classification models, 214-223

Research Article

Nezihe Yıldırım; Hardware Implementation of Fully Controlled Bridge Rectifier with Rapid Control Prototyping Approach, 224-230

Research Article

Uğur Yeşilyurt; Multipath Characteristics of Orbital Angular Momentum Vortex Electromagnetic Radio Waves Over an Infinite Ground Plane, 231-239

Research Article

Ferdi Özbilgin, Hüseyin Çalık, Mehmet Cem Dikbaş; Average Wind Speed Prediction in Giresun-Kümbet Plateau Region with Artificial Neural Networks, 240-246

Research Article

Ercan Aykut, İhsan Alshuraida; Grid Integration Strategies for Optimizing Renewable Energy Deployment and Grid Resilience, 247-254

Research Article

Remzi Göçmen, Musa Çıbuk, Erdal Akin; Comparative Analysis of Deep Learning Algorithms in Fire Detection, 255-261

Research Article

Hersh Hasan Taha Al-dawoodi, Hilmi Aygün; A Comparison Study of Some Metaheuristic Methods for Field Oriented Control Based Induction Motors, 262-272

BALKAN JOURNAL OF ELECTRICAL & COMPUTER ENGINEERING

(An International Peer Reviewed, Indexed and Open Access Journal)

Contact

Batman University
Department of Electrical-Electronics Engineering
Bati Raman Campus Batman-Turkey

Web: <https://dergipark.org.tr/en/pub/bajece>

<https://www.bajece.com>

e-mail: bajece@hotmail.com

Estimation of the Effect of Electric Vehicles on the Aging of Distribution Transformers Using Fuzzy Logic

Onur Akar


Abstract— Depending on industrialization and technological advancements worldwide, the demand for electrical energy, recognized as clean and dependable energy, is on the rise. Presently, electric energy consumption has notably increased alongside the rise in Electric Vehicles (EVs). The surge in EVs necessitates a thorough examination of the situation, anticipating the widespread adoption of Electric Vehicle Fast Charging Stations (EVFCS) in the near future and the subsequent escalation of their adverse impact on the grid. To mitigate these negative effects on the grid, proactive measures are essential. EVs function as capacitive loads due to their battery composition, and the harmonics produced during their grid connection detrimentally affect the quality of grid electricity, leading to constraints. Furthermore, the escalating EVFCS loads resulting from the rapid growth in EV numbers distribute the burden on distribution networks, posing a threat to network adequacy and reliability. Therefore, integrating EVFCS with distribution and generation units to minimize overloading, additional losses, and voltage fluctuations in the grid will enhance the efficiency of both systems. In addition, each EVFCS is only connected to the distribution transformer assigned to it or to the distribution transformers considered suitable in the city. Depending on the current drawn by one or more EVFCS linked to the feeder of each transformer, it can lead to overloading in transformers and chemical changes in windings and oils, resulting in the aging of transformers. In this context, a Fuzzy Logic (FL) based estimation is conducted to assess the impact of EVs' charging loads on transformer aging. The FL method utilizes transformer current load, EVFCS load, transformer temperature, and harmonic power quality data. The data utilized are derived from statistical information about a local distribution network and measured values from a feeder, and the aging effects on EVFCS distribution transformers are examined.

Index Terms— Distribution network, fuzzy logic, distribution transformers, transformer aging, electric vehicle fast charging station.

I. INTRODUCTION

IN ORDER to reduce carbon emissions and phase out dependence on oil, conventional engine technologies must be replaced with more efficient and environmentally friendly

ONUR AKAR, Department of Electronics and Automation, Marmara University, Istanbul, Turkey, (e-mail: onur.akar@marmara.edu.tr).

 <https://orcid.org/0000-0001-9695-886X>

Manuscript received June 23, 2024; accepted September 18, 2024.

DOI: [10.17694/bajece.1503781](https://doi.org/10.17694/bajece.1503781)

alternatives [1]. EVs have emerged as a solution to mitigate the negative impacts of traditional cars. EVs undergo fewer energy conversions and experience less energy loss compared to gas-powered vehicles. One of the primary motivations for producing EVs is to curb greenhouse gas emissions and harmful gases that contribute to global warming [2-4]. While the growing adoption of EVs to replace internal combustion engine vehicles decreases carbon dioxide emissions, it also presents challenges. The time needed for full EV charging can be up to 30 hours for home charging, known as Level-1 charging. Home charging typically requires overnight charging, while at regular charging stations it takes 2 to 4 hours; especially for EV fast charging stations designed for long distances, this time is reduced to 30 minutes [5-9]. Furthermore, EVs impact the reliability of the electricity distribution network by introducing uncertain loads on the grid based on battery levels. Charging EVs during peak hours increases the overall energy demand on transformers, potentially leading to transformer overload and degradation of their electromechanical structure and electrical quality [10, 11]. Overloading a transformer leads to an increase in the temperature of its windings and oil. Additionally, the induction flux of the scattered magnetic field rises, causing a surge in eddy currents that heat up and harm the transformer. This scenario is influenced by the current level and temperature, hastening the aging process of the transformer. Moreover, harmonic distortions manifest in the electrical energy system in conjunction with these circumstances [12]. Numerous studies have been conducted to maintain distribution network parameters within specified limits [13, 14]. These studies reveal the application of probabilistic power flow, utilization of various probabilistic models, and execution of stochastic analyses [15-17]. Furthermore, the impact of EVs on distribution networks has been explored; adverse effects such as loading, heating, and aging of transformers have been scrutinized, with assessments made regarding total power loss in the system, the network voltage's adherence to desired levels, voltage instability, and voltage stability [18-24]. The connection of nonlinear loads results in the intake of nonlinear currents into the distribution network, thereby distorting the system's voltage [24, 26]. The primary cause of harmonic distortion in a power distribution system is the increase in power losses, transformer degradation, and potential equipment failure due to temperature elevation [27, 28]. Based on the findings of 130 analyses conducted on a 150 kV power transformer in Indonesia, the aging state of the transformer was compared with its actual age. The determination of the apparent

age and aging condition of the transformer was performed using the Health Index Method [29]. Furthermore, a novel intelligent charging algorithm that controls the PEV through the Monte Carlo method was also investigated to assess the impact of plug-in electric vehicle (PEV) charging on the overhead load under various scenarios aimed at mitigating distribution transformer overloading. The influence of ambient temperatures on the distribution transformer was examined, revealing that PEVs can significantly decrease the thermal aging of the transformer through the implementation of intelligent charging strategies [30]. Another study concluded that electrical and thermal aging in transformers not only leads to rapid transformer failures but also results in degradation of transformer oil. Research has been conducted on the recycling of transformer oil [31-34].

In this study, unlike other studies, using transformer data from an existing real HV/LV distribution network, the changes in power, harmonics, load, and temperature values of distribution transformers in a newly modelled network [25] created by the default EVFCS are analyzed with fuzzy logic (FL). When EVFCS is connected to the normal network, the changes in the transformer are compared. The aging rate of the transformer is investigated.

II. MATERIAL AND METHOD

A. Model distribution network

Istanbul Province has 4 units of 1600 kVA HV/LV transformers connected to Kavacik and Umraniye step-down transformers at various HV levels. These are situated on the lower feeders of the 380/34.5 kV and 125 MVA transformer, supplying the distribution network. Additionally, there are units of 1600 kVA HV/LV transformers on the lower feeders of the 154/34.5 kV and 125 MVA transformer. The technical details of the transformers and default EVFCS load data of a semi-ring

network with 3 HV/LV transformer feeders of 1000 kVA and 1 HV/LV transformer feeder of 1600 kVA at the 34.5/0.4 kV level through a coupling breaker were employed. Figure 1 depicts a single-line diagram of the existing network [25].

B. Distribution network data

Existing urban distribution networks are heavily loaded based on consumer density. Furthermore, the integration of EVFCS leads to an increase in the network's loading rate on the

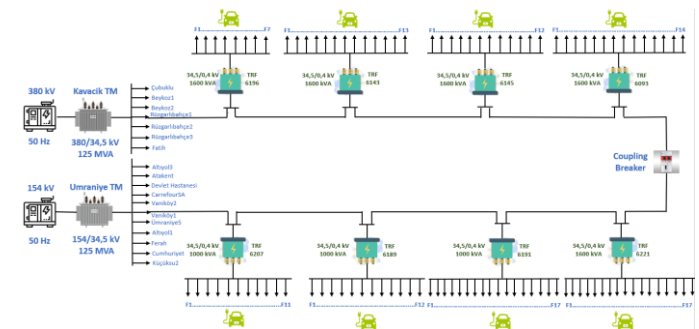


Fig.1. Single line diagram of the selected distribution network transformer, distributed according to the Electric Vehicle's battery charge. Figure 2.a illustrates the grid's loading status with the connection of EVFCS. Moreover, with the growing number of EVFCS, overloading occurs beyond a certain power threshold, resulting in phase imbalances. Analyzing the battery capacities of EVs reveals the impact of harmonics on the system as sinusoidal disturbances, which vary quadratically due to other influencing factors. Since EVs from different manufacturers have varying capacities, the harmonic effects they generate differ. Figure 2.b demonstrates the shift in the network's harmonic state as the number of EVFCS increases, nearly doubling the fluctuations in the standard network. These increased fluctuations further impact the transformer. In

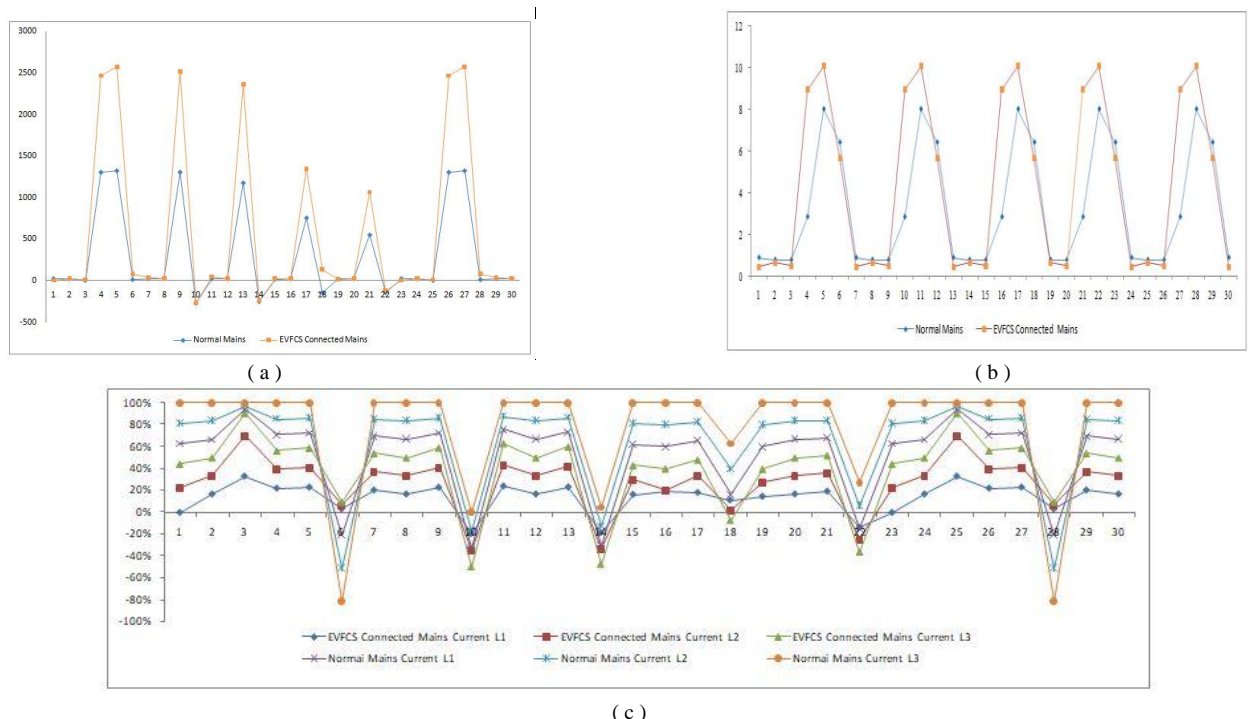


Figure 2. a) Load variation in the network, b) Harmonic variation in the network, c) Graph illustrating the percentage change in network phases when EVFCS is connected to the standard network

addition, when EVs are connected to the charging station, the harmonic loads they generate in the grid result in power losses, leading to adverse effects on charging infrastructure and restricting the number of EVs that can be charged simultaneously. Figure 2.c illustrates the phase variations based on the fluctuation of current drawn from the grid. The imbalance among the phases results in an excessive current draw and subsequent overheating. This rise in temperature will impact the transformer oil and windings, accelerating insulation deterioration, which in turn increases the risk of insulation damage and the likelihood of dielectric failure. Consequently, the transformer experiences wear and aging, making it challenging to manage and minimize losses in aging transformers. Moreover, the phase imbalance caused by the load compels the transformer to consume reactive power, imposing a burden on both the transformer and the network. With the increase in reactive power, the efficiency of both the transformer and the network decreases [25].

C. The FL Method

In this study, transformer aging is analyzed using 4 different input values and 1 output value in the network. The Mamdani fuzzy inference model, a commonly preferred fuzzy model in FL, is utilized. The 4 input values are defined as EVFCS power, network harmonic values, ambient temperature values, and the current load of the distribution network. The desired output value is the aging rate of the transformer, calculated as a percentage. The proposed FL output is illustrated in Figure 3.

For various EVFCSs, EV power (kW), temperature (°C), and grid power load (kW) in each of them are considered inputs to estimate the aging in a given network. The study aims to determine the network output using the input values. Membership functions were established for the input and output

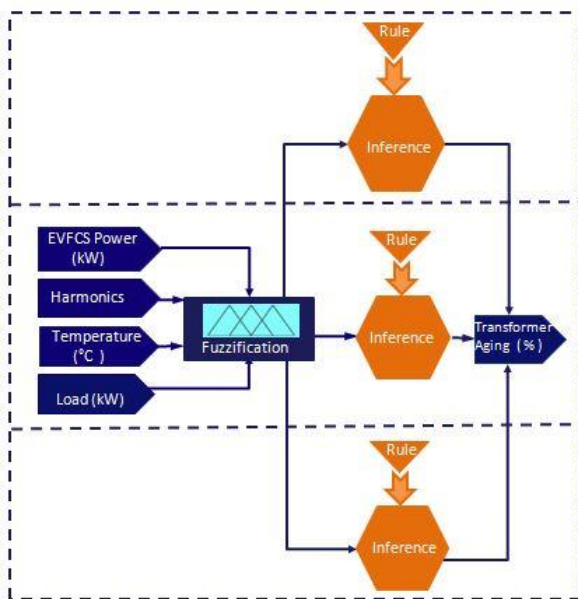
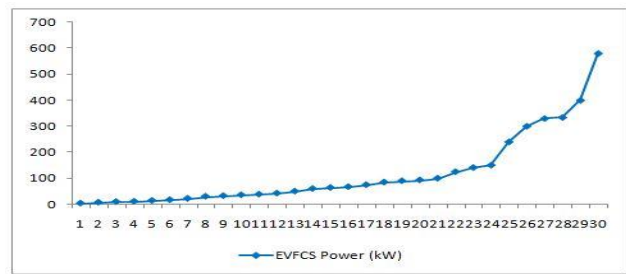
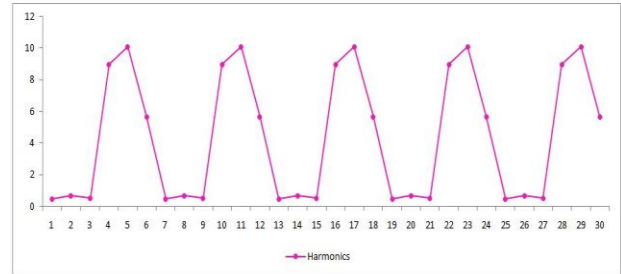


Fig.3. General flow diagram of FL

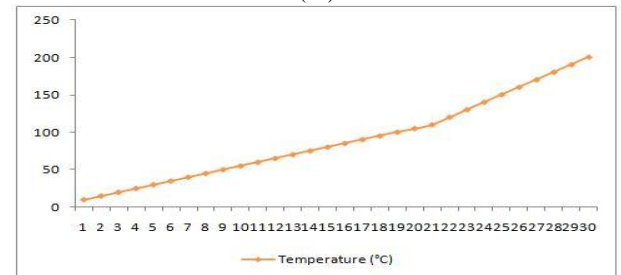
parameters identified in the FL application. The minimum and maximum values of the membership functions are depicted in Figure 4.a–e.



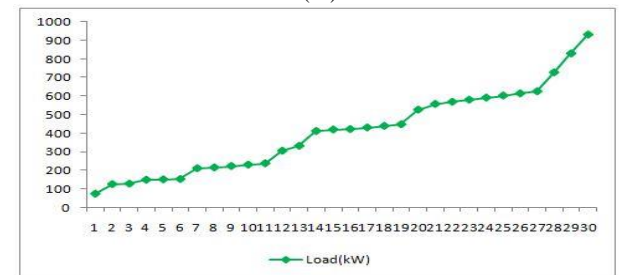
(a)



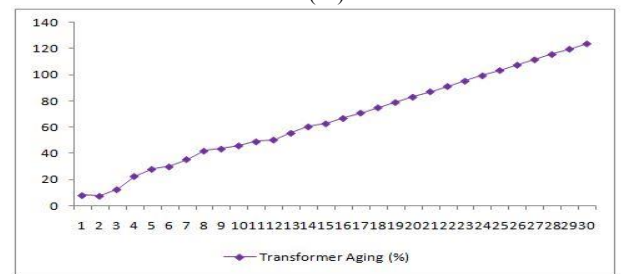
(b)



(c)



(d)



(e)

Fig.4. a) EVFCS power (kW), b) Harmonic, c) Temperature (°C), d) Load (kW), e) Graphical representation of membership function for transformer aging (%)

While creating the membership functions in the parameters used, the membership functions commonly used in the electricity demand forecasting model in the literature were preferred. The membership functions shown in Figures 5–9 define the fuzzy sets A_i and B_i . The triangular membership function in equation (1)-(2) is used for the input and output

variables. The clusters defined in the figures are validated with the membership functions in equation (1)-(2) [35, 36].

$$\mu_A = \mu_A(x; a, b, c) = \left\{ \begin{array}{ll} \frac{(x-a)}{(a-b)} & \text{if } a \leq x < b \\ \frac{(c-x)}{(c-b)} & \text{if } b \leq x \leq c \\ 0 & \text{if } x > c \text{ or } x < a \end{array} \right\} \quad (1)$$

$$A = \sum_i^n \mu_{A_i}(x_i) \Rightarrow \{(x, \mu_A(x))\} \quad (2)$$

EVFCS power, harmonic, current grid load status inputs, and transformer aging rate output are determined using triangular membership functions, each comprising 7 categories: Very Very Small (VVS), Very Small (VS), Small (S), Normal (N), Big (B), Very Big (VB), and Very Very Big (VVB). Graphical representations of the maximum and minimum values of these membership functions can be found in Figs. 5–7.

The triangular membership function of the temperature parameter consists of 7 groups: Very Very Low (VVL), Very Low (VL), Low (L), Normal (N), High (H), Very High (VH), Very Very High (VVH). The graph showing the values of the

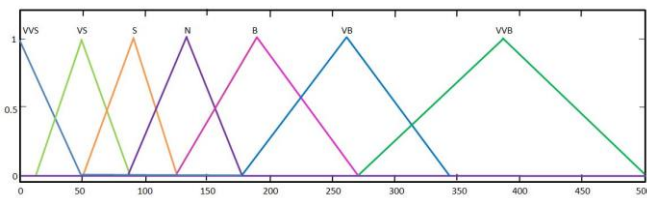


Fig. 5. Membership function for the EVFCS power parameter

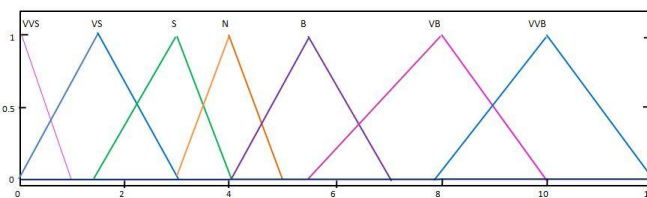


Fig. 6. Membership function for the harmonic parameter

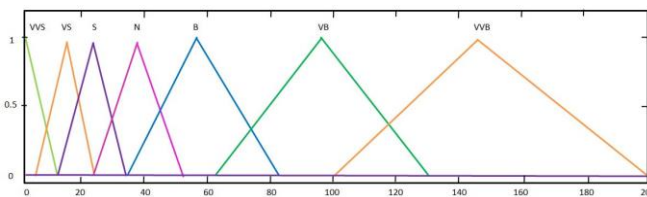


Fig. 7. Membership function for the load parameter

membership function for the temperature parameter is shown in Figure 8.

Transformer aging is represented by triangular membership functions, each comprising 7 distinct groups: Very Very Little Aging (VVLA), Very Little Aging (VLA), Little Aging (LA), Normal Aging (NA), Large Aging (LA), Very Large Aging

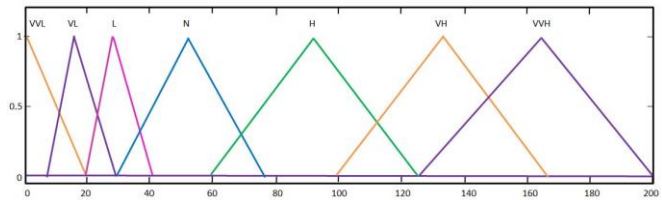


Fig. 8. Membership function for the temperature parameter

(VLA), and Very Very Large Aging (VVLA). These categories are visually depicted in Figure 9.

The membership function table defined according to EVFCS, harmonic, current transformer load, and temperature is as defined in Table I.

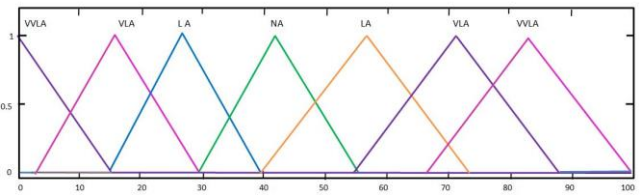


Fig. 9. Membership function for the transformer aging parameter

III. FINDINGS AND DISCUSSION

TABLE. I
TABLE OF RULES SHOWING THE EFFECT OF INPUT VALUES ON OUTPUT VALUES

EVFCS Power, Harmonic, Load	VVS	VS	S	N	B	VB	VVB
Temperature							
VVL	VVSA	VSA	SA	NA	VBA	VBA	VVBA
VL	VSA	VVSA	VSA	VSA	BA	VBA	VVBA
L	VVSA	VSA	VSA	NA	BA	VBA	VVBA
N	VVSA	VSA	SA	NA	BA	BA	VBA
H	BA	BA	BA	BA	VBA	VVBA	VBBA
VH	VBA	BA	VBA	VBA	VVBA	VBBA	VBBA
VVH	VVBA	VVBA	VVBA	VVBA	VVBA	VVBA	VVBA

In the FL method utilized in this research, rules are established based on the membership functions of the input parameters. The input data ranges from 0 to 1000 as numerical values. However, the adjustment to the range of 0 to 1 is determined through rule-based fuzzification. A total of 196 rules were defined for membership functions based on these 4 inputs and 1 output. Following the definition of these rules in the program, the percentage change in transformer aging was analyzed in relation to the input values of harmonic, temperature (°C), EVFCS power (kW), and grid load (kW).

The 3D graph illustrating aging predictions in the transformer system is displayed in Figure 10. This graph depicts the relationship between input values and output values. The steepness of the blue section indicates that transformer aging

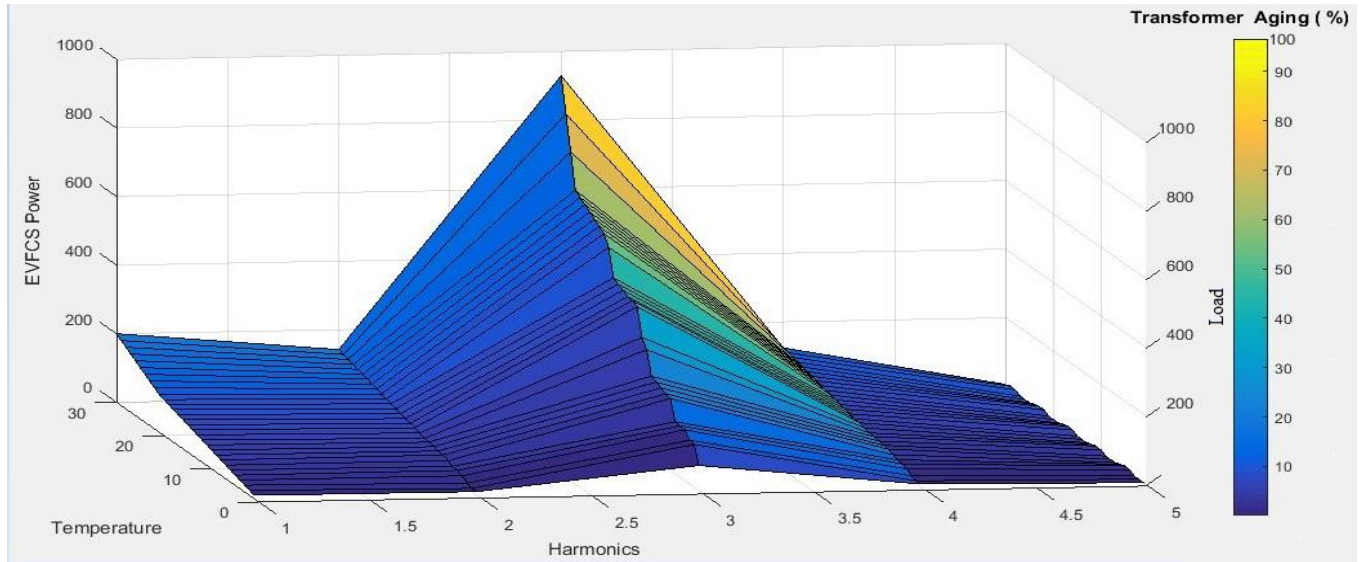


Fig.10. 3D graph of the output obtained according to the input values used in transformer aging

escalates with rising temperatures. Moreover, the heightened intensity of the yellow section suggests that aging in the transformer is influenced by EVFCS power variations. The distortions in the 3D graph, along with the increased yellow intensity, highlight the impact of adding EVFCS power to the load on transformer aging. The presence of distortions in the 3D graphics intensifies with the aging rate of the transformer. In FL, besides the established membership rules, different output values were obtained through testing with various input values in addition to the defined rules in the image. Figures 11.a–d depict the prediction output graphs of the values utilized as parameters for transformer aging prediction. When diverse input values were tested, a high level of agreement was noted between the prediction outcome and the data acquired in response to the test values. Figure 11.a illustrates the variation in transformer aging based on the EVFCS power commissioned. In Figure 11.b, the transformer maintains a constant temperature. However, with the current drawn from the network, the transformer experiences heating. There is a specific decrease observed. Nevertheless, once the current drawn from the network decreases, the temperature stabilizes after reaching a certain point. Yet, if the temperature surpasses

a specific threshold, the aging rate of the transformer escalates, leading to insulation deterioration. If this situation persists, the aging of the transformer will increase, leading to operational failure and necessitating replacement. This is unfavourable due to the associated costs. Figure 11.c illustrates the variation in the transformer's aging rate based on the load. The aging rate of the transformer adjusts according to the load increment. Figure 11.d shows the aging of the transformer due to harmonics. The connection of EVs to the charging station introduces harmonic loads to the grid, resulting in adverse effects. The continuous escalation of harmonic imbalances accelerates the aging process of the transformer, rendering it inoperable. Following numerous tests, the accuracy rate of FL estimation was determined to be 96.973%, in line with the specified criteria. The test verification rate was established at 95.321%. Statistical analysis of the prediction results revealed an error rate of 1.652%. A high degree of similarity was observed between the expected and actual outcomes. The 85th trial yielded results closest to the predictions. As can be seen from the figures examined, as the number of EVFCS connected to the network increases, the load on the transformer also increases proportionally. Additionally, factors

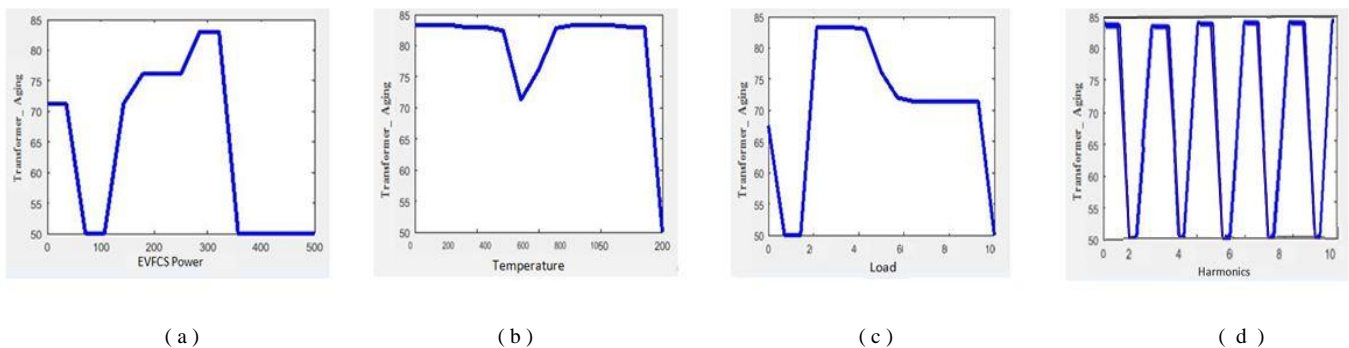


Figure 11. Prediction output graphs of the values used for the transformer aging prediction parameter
 a)Transformer_Aging- EVFCS, b)Transformer_Aging- Temperature, c) Transformer_Aging- Load d) Transformer_Aging- Harmonics

such as load and temperature contribute to the deterioration of transformer insulation, leading to the drawing of reactive power due to phase imbalances. Overloading results in up to 70% wear and tear on the transformer. The 100 kVA transformers in rural areas are insufficient to support EVFCS connections, necessitating an increase in transformer capacity to prevent overloads. In urban networks, overloads occur when both the network experiences a heavy load and EVFCS are introduced, causing premature aging and rendering the transformers inoperable. The increase in harmonics directly correlates with the accelerated wear and tear on the transformer. This continuous deterioration leads to the aging of the transformer over time, increasing the likelihood of replacement, which is a costly process.

However, with the increase in the rate of EVs used, the income level for EV purchase varies according to location, and although it is necessary in terms of efficiency and environmental impacts, it emerges as an additional burden on the network. Load conditions on the grid vary depending on the synchronization, charging power, and duration of the vehicles. Companies operating the distribution system should consider these situations while planning. It has been known that high and unbalanced currents occur in the phases to which single-phase EVFCS are connected. This situation adversely affects the cable heating, losses, and devices connected to the network due to the unbalanced loading of the lines. This situation is not seen very often in the phases to which the three-phase EVFCS is connected. In addition, if fast charging is used, it will bring much more additional load to the grid, that is, the existing transformer, compared to the normal charging situation, so appropriate studies should be carried out and precautions should be taken.

VI. CONCLUSION

In this study, when the results obtained in the estimation with FL were tested with the given approximate values, it was observed that it was achieved at a rate of 95.321%. 1,652% of the errors were obtained based on the defined rules. As a result of the predictions made by classifying the numerical data according to qualitative characteristics in FL, the accuracy rate in prediction with FL was found to be 96.973%. Thanks to the accurate estimation, the aging rate in the transformer can be reduced by determining the rate of aging in the transformer as a percentage. The study has provided the opportunity to determine the aging rate in transformers as a percentage and offers new suggestions to mitigate the factors influencing aging. One suggestion is that smart grids, where instantaneous grid power flow and the physical condition of transformers can be monitored, should be preferred over existing distribution networks to eliminate the negative effects of EVFCS on the grid. It is believed that this study will make a significant contribution to the literature.

REFERENCES

- [1] P. Ahmadi, "Environmental impacts and behavioral drivers of deep decarbonization for transportation through electric vehicles", *J. Clean. Prod.* (2019).
- [2] J. R. Weeberb, M. Moataz, D. H. Christopher, A. Altaf, F. Mark, "How Clean Are Electric Vehicles? Evidence-Based Review of the Effects of Electric Mobility on Air Pollutants, Greenhouse Gas Emissions and Human Health", *Atmospheric Environment*, 185(2018), 64-77.
- [3] L. Calearo, M. Marinelli, & C. Ziras, "A review of data sources for electric vehicle integration studies", *Renewable and Sustainable Energy Reviews*, 151, 111518, 2021.
- [4] U.K. Terzi, et. al. , "A review of commercial electric vehicle charging methods", *Promet - Traffic - Traffico*, vol.32, no.2, pp.291-307, 2020
- [5] I. Diahovchenko, A. Chuprun, & Z. Čonka, "Assessment and mitigation of the influence of rising charging demand of electric vehicles on the aging of distribution transformers", *Electric Power Systems Research*, 221, 109455, 2023.
- [6] A. Srivastava, M. Manas, R. K. Dubey, "Integration of power systems with electric vehicles: A comprehensive review of impact on power quality and relevant enhancements", *Electric Power Systems Research*, 234, 110572, 2024.
- [7] S. Powell, E. Kara, R. Sevlian, G. V. Cezar, S. Kiliccote, & R. Rajagopal, "Controlled workplace charging of electric vehicles: The impact of rate schedules on transformer aging", *Applied Energy*, 276, 115352, 2020.
- [8] US Energy, 2016, US Department of Energy, "Developing Infrastructure to Charge Plug-In Electric vehicles", date received: 11.05.2024.
- [9] F. Kaya, O. Akar. "Short Circuit Effects on HV Feeders of Optimally Located Electric Vehicle Fast Charging Stations", *IEEE Access*, vol.12, 47842-47853, 2024.
- [10] G. P. Tal, D. P. Chakraborty, A. P. Jenn, J. H. P. Lee, D. P. Bunch, "Factors affecting demand for plug-in harging infrastructure: an analysis of plug-in electric vehicle commuters", UC off. Pres. ITS Rep, 2020.
- [11] C.B. Jones, M. Lave, W. Vining, B.M. Garcia, "Uncontrolled electric vehicle charging impacts on distribution electric power systems with primarily residential", commercial or industrial loads', *Energies*, 2021.
- [12] V. Volokhin, I. Diahovchenko, V. Kurochkina, M. Kanálík, "The influence of nonsinusoidal supply voltage on the amount of power consumption and electricity meter readings", *Energetika* 63 (1), 2017.
- [13] O. Sundstrom, C. Binding, "Flexible charging optimization for electric vehicles considering distribution grid constraints", *IEEE Transactions on Smart Grid*, 2012, 3(1), 26-37.
- [14] P. Richardson, D. Flynn, A. Keane, "Optimal charging of electric vehicles in low voltage distribution systems." *IEEE Transactions on Power Systems*, 2012, 27(1), 268-279.
- [15] R. C. Leou, C. L. Su, C. N. Lu, "Stochastic analyses of electric vehicle charging impacts on distribution network", *IEEE Transactions on Power Systems*, 2014, 29(3), 1055-1063.
- [16] T. Au, M.Ortega-Vazquez, "Assessment of plug-in electric vehicles charging on distribution networks", *IEEE Power & Energy Society General Meeting*, Vancouver, Canada, 21 – 25 July 2013.
- [17] G. Li, X. Zhang, "Modeling of plug-in hybrid electric vehicle charging demand in probabilistic power flow calculations", *IEEE Transactions on Smart Grid*, 2012, 3(1), 492-499.
- [18] R. A. Verzijlbergh, M. O. W. Grond, Z. Lukszo, J. G. Slootweg, M. D. Ilic, "Network impacts and cost savings of controlled EV charging", *IEEE Transactions on Smart Grid*, 2012, 3(3), 1203-1212.
- [19] Z. Liu, F. Wen, G. Ledwich, "Optimal planning of electric vehicle charging stations in distribution systems", *IEEE Transactions on Power Delivery*, 2013, 28(1), 102-110.
- [20] S. Weckx, R. D'Hulst, B. Claessens, J. Driesensam, "Multiagent charging of electric vehicles respecting distribution transformer loading and voltage limits", *IEEE Transactions on Smart Grid*, 2014, 5(6), 2857-2867.
- [21] L. Hua, J. Wang, C. Zhou, "Adaptive electric vehicle charging coordination on distribution network", *IEEE Transactions on Smart Grid*, 2014, 5(6), 2666- 2675.
- [22] S. Shafiee, M. Fotuhi-Firuzabad, M. Rastegar, "Investigating the impact of plug-in hybrid electric vehicles on power distribution systems", *IEEE Transactions on Smart Grid*, 2013, 4(3), 1351-1360.
- [23] J. De Hoog, T. Alpcan, M. Brazil, D. A. Thomas, I. Mareels, "Optimal charging of electric vehicles taking distribution network constraints into account", *IEEE Transactions on Power Systems*, 2015, 30(1), 365-375.
- [24] F. Shahnia, A. Ghosh, G. Ledwich, F. Zare, "Predicting voltage unbalance impacts of plug-in electric vehicles penetration in residential low voltage distribution networks", *Electric Power Components and Systems*, 2013, 41(16), 1594-1616.

- [25] F. Kaya, "Analysis of the effects of electric vehicle fast charging stations on the network", M.S. thesis, Dept. Electr. Educ., Marmara Univ., Istanbul, Türkiye, 2023.
- [26] O. Akar, "Estimation through ANN of Voltage Drop Resulting from Overloads on Power Transformers", *European Journal of Technique*, vol.12, no.2, pp.198-203, 2022
- [27] I. Diahovchenko, B. Dolník, M. Kan'alik, J. Kurimský, "Contemporary electric energy meters testing under simulated nonsinusoidal field conditions", *Electr. Eng.* 104 (2022) 1077–1092.
- [28] B. R. Klingenberg, et al. "Fuzzy logic application for time-varying harmonics", in *Time-Varying Waveform Distortions in Power Systems*, 2009.
- [29] W. R. Tamma, R. A. Prasojo, S. Suwarno, "Assessment of high voltage power transformer aging condition based on health index value considering its apparent and actual age", In *2020 12th International Conference on Information Technology and Electrical Engineering (ICITEE)* (pp. 292-296). IEEE, 2020, October.
- [30] A. D. Hilshey, P. D. Hines, P. Rezaei, J. R. Dowds, "Estimating the impact of electric vehicle smart charging on distribution transformer aging", *IEEE Transactions on Smart Grid*, 4(2), 905-913, 2012.
- [31] F. Guerbas, M. Aoudjit and S. Abba, "Comparative Study of Transformer aged oil Reclamation by Fuller's earth and activated Bentonite", *2017 IEEE 19th International Conference on Dielectric Liquids (ICDL)*. IEEE, 2017.
- [32] A. Vatsa, & A. S. Hati, "Insulation aging condition assessment of transformer in the visual domain based on SE-CNN," *Engineering Applications of Artificial Intelligence*, 128, 107409, 2024.
- [33] A. Srivastava, M., Manas, & R. K. Dubey, "Integration of power systems with electric vehicles: A comprehensive review of impact on power quality and relevant enhancements," *Electric Power Systems Research*, 234, 110572, 2024.
- [34] G. Kaliappan, & M. Rengaraj, "Aging assessment of transformer solid insulation: A review. *Materials Today: Proceedings*," 47, 272-277, 2021.
- [35] Z. Ok Davarcı, O. Akar, "Estimation of the electricity to be generated at different wind speeds and turbines through fuzzy logic and ANN, A case study of Balıkesir," *Int J Energy Studies* 2024; 9(1): 115-133, e-ISSN: 2717-7513.
- [36] Z. Ok Davarcı, O. Akar, U.K. Terzi, "Comparison of Road Luminance Data Estimated by Fuzzy Logic and ANN", A Case study of Kocaeli Sakıp Sabancı Caddesi, *European Journal of Technique* , vol.13, no.2, 150-158, 2023.

BIOGRAPHY



Onur AKAR was born in 1981 in Giresun. He received his undergraduate, graduate and doctorate degrees from Marmara University in 2005, 2011 and 2020, respectively. He worked as a lecturer at Istanbul Gedik University between 2010-2020. He served as the Head of Electricity Program at Istanbul Gedik University between 2012-2015. He served as the Head of the Department of Electricity and Energy between 2021-2022 as an assistant professor in the Department of Electricity and Energy of the same university. He is still working as an Assistant Professor Marmara University, Vocational School of Technical Sciences. His research interests include Control Systems, Renewable Energy Systems, Power Systems and Lighting Systems.

The Effect of Linear Discriminant Analysis and Quantum Feature Maps on QSVM Performance for Obesity Diagnosis

Zeynep Ozpolat, Ozal Yildirim and Murat Karabatak


Abstract— Obesity, characterized by an excessive accumulation of body fat, is a significant health issue that predisposes individuals to numerous diseases. Therefore, early intervention and necessary measures in the diagnosis and treatment of obesity are of great importance. In medicine, classical machine learning algorithms are widely used to accelerate the prediction process. However, the increasing volume of data often renders these algorithms insufficient for accurate disease diagnosis. At this point, quantum computing-based algorithms offer more efficient and faster solutions by leveraging quantum physics, which operates contrary to the principles of classical physics. Dimensionality reduction techniques play a critical role in both classical and quantum classifiers. In this study, classical dimensionality reduction methods, namely Linear Discriminant Analysis (LDA) and Principal Component Analysis (PCA), were applied to an obesity dataset. The dataset was subsequently analyzed using Quantum Support Vector Machine (QSVM) and Support Vector Machine (SVM) algorithms. As part of the QSVM studies, three different quantum feature maps, which facilitate the quantum bit transformation of classical bit data, were also compared. The analysis revealed that the proposed LDA-QSVM method achieved 100% accuracy when used with the Z and Pauli X feature maps. This remarkable success, which is rarely seen in the literature on obesity data, underscores the potential of quantum-based algorithms in the diagnosis and treatment of obesity.

Index Terms— Obesity, Linear Discriminant Analysis, Quantum Support Vector Machine, Dimensionality Reduction, Quantum Machine Learning.


I. INTRODUCTION

GLOBALY, OBESITY poses a significant public health concern. Examining the relationship between eating habits and physical condition is important for understanding


Zeynep Ozpolat, is with Department of Software Engineering Mus Alparslan University, Mus, Turkey, (e-mail: z.ozpolat@alparslan.edu.tr).

 <https://orcid.org/0000-0003-1549-1220>

Ozal Yildirim, is with Department of Software Engineering Firat University, Elazig, Turkey, (e-mail: ozalyildirim@firat.edu.tr).

 <https://orcid.org/0000-0001-5375-3012>

Murat Karabatak, is with Department of Software Engineering Firat University, Elazig, Turkey, (e-mail: mkarabatak@firat.edu.tr).

 <https://orcid.org/0000-0002-6719-7421>

Manuscript received April 30, 2024; accepted Sep 07, 2024.

DOI: [10.17694/bajece.1475896](https://doi.org/10.17694/bajece.1475896)

and managing the obesity problem in detail [1]. Examining the relationship between eating habits and physical condition is important for understanding and managing the obesity problem in detail. Obesity not only has negative impacts on the health of individuals, but can also be a major burden on health systems and economies. Therefore, it is important to develop and implement effective strategies to combat obesity. Given that technological advances have raised living standards, it is inevitable that they will help experts in the field of medical diagnosis. Prediction systems, which aim to guide the diagnosis and treatment process of many diseases developed for this purpose, are actively used in obesity [2]. These systems play an important role in determining the obesity risk of individuals and making healthy lifestyle recommendations.

In recent years, when interdisciplinary studies have become popular, the approach between medicine and informatics has led to great advances. Machine learning applications have been widely used for diseases such as obesity that require complex and multifaceted investigations [3]. Thanks to these algorithms, large amounts of data can be analyzed and controls such as risk factors, treatment options and health status of patients can be easily monitored. Machine learning algorithms aim to find patterns and relationships to solve a problem [4]. However, growing data sizes and diversity have started to make this process difficult. For this reason, the concept of quantum computing and quantum machine learning, which has a different perspective of quantum physics, has gained its place today [5]. Thanks to the interesting perspective of quantum physics that allows us to consider every possibility, machine learning algorithms have also started to be actively used in the quantum world [6].

In diseases such as obesity, where many parameters are effective, the diversity in terms of attributes is very high. These attributes need to be reduced to enable more effective use of both classical and quantum algorithms [7]. However, since it is disease data, it would be more appropriate to reduce the number of attributes by using various mathematical operations instead of completely removing an existing attribute from the data set [8]. The most common dimensionality reduction algorithms are Principal Component Analysis (PCA) [9] and Linear Discriminant Analysis (LDA) [10].

Quantum computers are physically available in only a few locations worldwide and are typically accessible through cloud-based or simulation environments. These computers offer users a limited number of quantum bits (qubits) [11]. Unlike classical bits, qubits are fundamental units of quantum information that

can represent multiple states simultaneously. Due to the limited number of qubits available, dimensionality reduction algorithms are crucial for effective data processing in quantum machine learning. Quantum machine learning algorithms utilize dimensionality reduction techniques not only for medical data but also across various other disciplines. Thus, applying dimensionality reduction methods is essential for optimizing the performance of quantum algorithms, just as it is for classical ones. After the relevant data is reduced to the number of qubits presented, it is converted into qubit form with the help of quantum feature maps [12]. Quantum feature maps are obtained using different combinations of quantum gates. Quantum feature maps with different properties are obtained with circuits built using Hilbert space and quantum gates. These feature maps make the datasets usable in quantum state space, facilitating the application of quantum machine learning algorithms.

Many studies have explored the potential of quantum machine learning algorithms in healthcare, and have shown significant progress in areas such as disease detection and classification. Some of these studies include: Kumar et al. [13] presented a QSVM quantum-based machine learning model for the detection of brain tumors. They showed that their proposed QSVM model provides 1.60% times better performance than classical SVM. Aksoy and Karabatak [14] analyzed the classification of EEG signals using QSVM. In their study, they classified EEG signals with QSVM with a performance of 99.47%. In another study [15], the authors achieved 100% success with Pauli X and Pauli Z feature maps for the detection of schizophrenia with EEG signals. Maouaki et al. [16] conducted a study comparing the classification performance of QSVM and classical SVM algorithms to improve prostate cancer detection methods. As a result of their analysis, they achieved 94% performance with ZZFeatureMap. Munşi et al. [17] evaluated the performance of QSVC and Variational Quantum Classifiers (VQC) for chronic heart disease

prediction. They found that the results obtained with QSVC showed a better classification performance compared to VQC.

In this study, the data of patients with obesity were used for classification with QSVM, a quantum-based machine learning algorithm. In order to evaluate the performance of QSVM, comparative analyses were also performed with the classical SVM algorithm with the same standards. Before applying the classical and quantum classification algorithms, the dataset was subjected to dimensionality reduction with PCA and LDA separately. Classical SVM and QSVM algorithms were applied to the new data sets. During the studies, the dimensionally reduced data with LDA and PCA were converted into qubits with Z, ZZ and Pauli X feature maps and classified with QSVM. As a result of the analysis, it was determined that the proposed classification method as LDA-QSVM achieved successful results in predicting obesity disease. Considering the process of quantum-based algorithms, which are still under development, these results are very promising. These findings emphasize the potential of studies in the field of quantum computing for the development of new and effective methods for the treatment and prevention of obesity.

II. MATERIALS AND METHODS

In this study, the classification performance of the QSVM algorithm is examined by testing various parameters on a dataset prepared to detect obesity based on eating habits and physical conditions. Quantum feature maps are used to transform a data set in classical form into qubit form. It has been observed that feature maps create performance differences in the QSVM algorithm used according to the transformations they make. Considering these changes, the performance of the QSVM algorithm is compared. A formal representation of the proposed method is given in Figure 1.

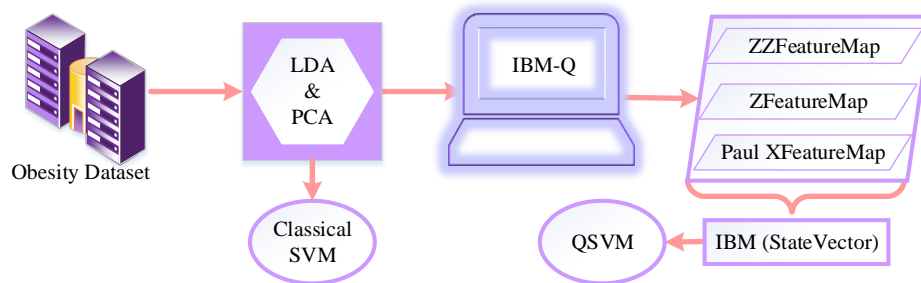


Fig.1. Schematic representation of the proposed method

A. Obesity Dataset

In this study, we use a dataset from the UC Irvine Machine Learning Repository, where obesity classes are created based on physical condition and eating habits [18]. This dataset contains 2111 records collected through questionnaires from patients and non-patients in Mexico, Peru and Colombia. In the dataset with 17 attributes, classification labels were obtained as Underweight, Normal Weight, Overweight Level I, Overweight

Level II, Obesity Type I, Obesity Type II and Obesity Type III labels, which are not included in the data, were created synthetically with the SMOTE filter using Weka [18]. Another 23% of the data was obtained through a web platform. The main purpose of creating this dataset is to determine the obesity level of the person and to help create recommendation systems that can monitor these levels [19]. Information about the attributes of the dataset is given in Table 1 [20].

TABLE I
GENERAL INFORMATION ABOUT THE OBESITY DATASET

Features	Description	Data Type
Gender	Sex	Men-Women
Age	Age	Values between the ages of 14-61
Height	Height (Meters)	1.45-1.98
Weight	Weight (Kilograms)	39-143
Family History With Overweight	Family History of Overweight	Yes-No
FAVC	High Calorie Food Consumption	Yes-No
FCVC	Vegetable Consumption Frequency	FCVC > 2, positive vegetable intake at each meal FCVC ≤ 2, zero vegetable intake in some meals
NCP	Number of Main Meals per Day	1-2-3-4
CAEC	Daily Snack Frequency	No, Sometimes, Often and Always
SMOKE	Smoking Status	Yes-No
CH2O	Daily Water Consumption Amount (Liters)	Between 1-3
SCC	Calorie Tracking	Yes-No
FAF	Physical Activity Frequency (Hours)	Between 0-3
TUE	Technological Tool Usage Time (Hours)	Between 0-2
CALC	Alcohol Consumption	Yes-No-Sometimes
MTRANS	Means of Transportation	Automobile, Motorcycle, Bicycle, Public Transportation, Walking
NObesydad	Obesity Level	Underweight, Normal Weight, Overweight Level I, Overweight Level II, Obesity Type I, Obesity Type II, Obesity Type III

When the data set was analyzed in general, it was observed that there was no missing data. It was determined that the data were homogeneously distributed according to the label groups.

B. Methods

In this paper, two different dimensionality reduction methods were applied to obesity data. The first one is the Principal Component Analysis (PCA) method, which is frequently used in quantum machine learning applications [21]. PCA is a statistical technique that reduces the dimensionality of data by identifying the principal components that capture the maximum variance in the data set. This method calculates the mean and variance of the data points and identifies the directions (principal components) along which the variance is maximized [14]. By projecting the data onto these components, PCA transforms the original data into a new set of uncorrelated variables (principal components), reducing the dimensionality while retaining as much variability as possible. The goal is to create a new data set of the desired size using eigenvalues and eigenvectors that correspond to the principal components. PCA is particularly effective in situations where the goal is to minimize information loss while reducing the complexity of the data.

The second method used is Linear Discriminant Analysis (LDA) [22]. LDA, like PCA, is a linear dimensionality reduction technique that also relies on eigenvalues and eigenvectors. However, LDA differs from PCA in its objective; while PCA focuses solely on maximizing variance within the data, LDA seeks to maximize the separation between different classes. It achieves this by finding the linear combinations of features that best separate the classes in the data. LDA thus takes into account not only the variance within classes but also the variance between classes. This makes LDA particularly useful for supervised learning tasks where the goal is to enhance class separability. As a result, LDA is often preferred in

situations where class discrimination is critical, such as in classification tasks. In this study, the advantage of LDA's ability to enhance class separability is emphasized, highlighting its superiority over PCA in certain contexts.

Furthermore, it is important to note that both PCA and LDA assume that the underlying data distribution is linear. This assumption can sometimes limit their effectiveness, especially in cases where the data exhibits complex, nonlinear relationships. However, despite these limitations, PCA and LDA remain widely used due to their simplicity, computational efficiency, and ability to reduce data dimensionality in a way that preserves essential information. In quantum machine learning, where data often needs to be compressed to fit within the constraints of quantum computing resources, these techniques are particularly valuable.

The data set, which is freed from the curse of dimensionality by using dimension reduction methods, should be made processable in quantum-based algorithms. Quantum feature maps are used for this purpose. In this study, ZZ, Z and Pauli X are chosen as quantum feature maps. ZZFeatureMap aims to create a dataset that can be processed by quantum algorithms by using the Controlled Z gate to convert classical bits into qubits. It performs transformations by providing transitions between pairs of qubits [23]. ZFeatureMap is another feature map that uses the controlled Z gate as in ZZ. The most important difference from ZZFeatureMap is that it performs bit-to-qubit transformations using single-qubit transformations along the Z axis [24]. The underlying structure of the other two feature maps used is the Pauli feature map. PauliZ is known as ZFeatureMap and PauliZZ is known as ZZFeatureMap [25]. The feature map name is determined according to the gates used in the Pauli map. In this study, in addition to the Z and ZZ feature maps, the Pauli X map was used in the analysis. Quantum circuit models of ZZ, Z and Pauli X feature maps were drawn using the Qiskit library as shown in Figure 2. Here, the repetition values of all circuits drawn were chosen as reps=1.

The entanglement parameter, which indicates in which state the entanglement feature present in the ZZ and Pauli X feature maps is selected, was set to “full”.

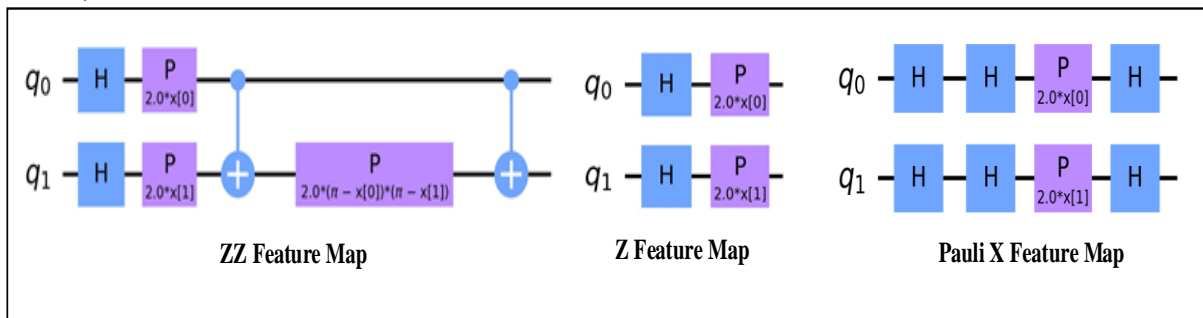


Fig. 2. Quantum circuits for ZZ, Z, and Pauli X feature maps, using Hadamard and Phase gates for data encoding.

Quantum feature maps are structures that transform classical data into qubits for processing in quantum environments. During the transformation process, the data is encoded in Hilbert space. While creating feature maps, circuit systems with different quantum gates are built. Thanks to these circuits, the data converted into qubits can be used in quantum machine learning algorithms [26]. The main factors used in feature map selection are; feature map circuit depth, data matching used in the encoding of classical data, quantum gates, and the processing order of binary qubit combinations [27].

The dataset transformed into qubit form using feature maps is now ready for use in a quantum machine learning application. The Quantum Support Vector Machine algorithm, which is frequently preferred in the literature in quantum machine learning, was preferred in this study [28]. The QSVM algorithm is a quantum-based classification algorithm based on the least squares method used in the classical SVM algorithm [29]. The classical SVM algorithm uses the least squares method to select the most appropriate hyperplane to classify the data into classes. QSVM first performs a coding step with vectors representing the quantum states of the data points. It then processes the data encoded into these quantum states with quantum circuits and performs classification as output. Thanks to the quantum circuit structures used in the QSVM algorithm, it can perform better in the classification of complex datasets [30].

III. EXPERIMENTAL RESULTS

A dataset prepared for the diagnosis of obesity was used in the experimental studies. LDA and PCA algorithms were progressively applied to the obesity data and analyzed. The new datasets created for different dimensions were processed with feature maps to convert them into qubit form. The main objective of the study is to measure the change in the performance of the QSVM algorithm after applying different types of feature maps to the dataset. For this purpose, three different feature maps were used, namely ZZ Feature Map, Z Feature Map and Pauli X Feature Map. While using the Pauli feature map, several combinations were tried and all of the analyses were performed for the case with the highest performance. All of the analyzes are presented comparatively with tables and graphs.

In order to measure the performance of the QSVM algorithm against a classical classification algorithm, analyses were also performed with the SVM algorithm. The dataset was divided into training and test. The test size was set to 40% and random_state was set to 900. Since the feature map used will not have any effect on the classical SVM algorithm, the results related to SVM are given separately. The effect on SVM varies with the LDA and PCA algorithms used when reducing the size of the dataset. For this reason, Table 2 shows the performance and runtime obtained with SVM.

TABLE II
PERFORMANCE EVALUATION OF SVM ALGORITHM ACCORDING TO LDA AND PCA

DR Methods	SVM	Features Number			
		3	4	5	6
LDA	ACC	100.0	100.0	100.0	100.0
	Run Time (sec)	0.01	0.02	0.03	0.04
PCA	ACC	66.98	72.43	72.54	77.87
	Run Time (sec)	0.47	0.36	0.56	0.44

When Table 2 is examined, it is seen that the analysis results obtained with LDA show 100% success for each case in which the size is reduced. The results obtained with PCA fall behind LDA both in terms of runtime and performance.

Obesity data dimensionally reduced using PCA and LDA were converted into qubit form using ZZ, Z and Pauli X feature maps respectively. Then, the quantum classification algorithm

QSVM was applied. When using ZZ and Pauli X feature maps, the parameters of the feature map were chosen as reps=2, entanglement=full, and reps=2 for Z since it has only circuit repetition parameter. The results of the analysis obtained by applying PCA and LDA for each feature map and classifying with QSVM are given in Table 3.

TABLE III
PERFORMANCE AND WORKING TIME OBTAINED IN ANALYZES

Feature Maps	DR Methods	QSVM	Qubit Numbers			
			Q(3)	Q(4)	Q(5)	Q(6)
ZZ	LDA	ACC	60.71	60.71	29.23	29.23
		Run Time (sec)	10884	10989	15879	14967
	PCA	ACC	67.33	71.00	73.72	75.14
		Run Time (sec)	116.77	146.71	170.19	201.55
Z	LDA	ACC	100.0	100.0	100.0	100.0
		Run Time (sec)	97.67	100.97	99.87	107.25
	PCA	ACC	64.61	67.92	70.05	72.66
		Run Time (sec)	106.86	109.47	112.99	117.24
Pauli X	LDA	ACC	100.0	100.0	100.0	100.0
		Run Time (sec)	63.72	69.81	71.93	72.58
	PCA	ACC	62.84	67.57	68.52	71.36
		Run Time (sec)	70.83	75.42	74.28	76.19

The reason for the low performance and high running times in the ZZ feature map is that the dataset structure used is not suitable for processing in this feature map. ZZ feature maps are designed for use with more complex datasets. The circuits created by using the Z gate twice contribute to the solution of complex problems by actively providing the transition between qubits. The main reason for the low performance of the ZZ feature maps in this study is the lack of complex data. Except for the ZZ feature map, the results obtained with LDA in the other two feature maps show that the performance of the QSVM

algorithm is much better than PCA. The performance improvement in dimensionality reduction due to LDA's good discrimination between classes, which has been proven in previous studies, is also evident in this study. In addition to the performance of LDA, the effect of the used feature maps on the performance of QSVM is clearly indicated in this study.

The performance comparison of the ZZ feature map, Z feature map and Pauli X feature map against the QSVM algorithm applied for dimensionally reduced datasets with LDA is given in Figure 3.

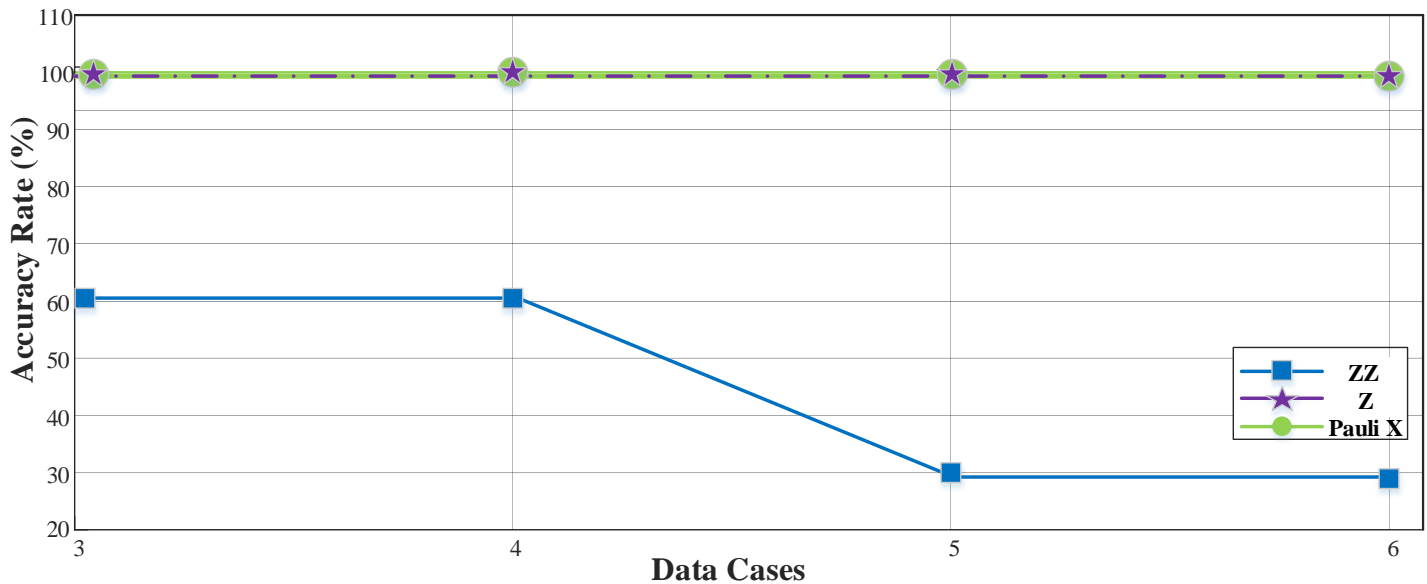


Fig.3. Performance comparisons of ZZ, Z and Pauli X feature maps

When Figure 3 is analyzed, Z and Pauli X feature maps showed 100% performance on the data reduced with the LDA algorithm on the obesity dataset. ZZ feature map caused a decrease in the performance of QSVM on the data generated by

the reduction of LDA on this dataset. When the precision metric was calculated according to the 100% accuracy performances obtained for the Z and Pauli X feature maps, it was found to be 100% for each class. Since both accuracy and precision

performances are 100% in obesity data, it is clear that it can help experts in the decision-making process in disease diagnosis.

IV. DISCUSSION

This study aims to apply a quantum machine learning algorithm to a dataset created for obesity detection. Among quantum machine learning algorithms, QSVM algorithm, which is a widely used algorithm in the literature, is selected. LDA and PCA, which are dimensionality reduction algorithms, were applied to reduce the data size in the obesity dataset, which has a high number of attributes. The new datasets obtained as a result of the application of these algorithms were passed through feature maps in order to apply quantum-based machine learning. The main purpose of this study is to measure the effect of the feature maps on the performance of the QSVM algorithm.

Experimental studies were carried out on the StateVector simulator made available by IBM Quantum Lab. Real computers could not be used due to the queue waiting time on real quantum computers. The StateVector simulator was preferred because it provides faster results compared to other simulators. By using ZZ, Z and Pauli X feature maps respectively, the data set in bit form was converted into qubit form to be used in quantum algorithms. Finally, the QSVM algorithm was applied to the new data sets obtained with different qubit numbers. In order to evaluate the performance of QSVM, dimensionally reduced data were also analyzed with SVM, a classical machine learning algorithm. Some of the studies in the literature using obesity dataset are given in Table 4.

TABLE IV
SOME STUDIES IN THE LITERATURE REGARDING THE OBESITY DATASET USED IN THE STUDY

Studies with Obesity Data Set		
References	Machine Learning Methods	Accuracy (%)
Kaur vd. [31]	RF	95.5
	Bagging	95.03
	XGB	96.45
	GB	96.33
	SVM	87.34
	K-NN	81.42
Putzel ve Lee [32]	Multiclass Classification	73
Solomon vd. [33]	SVM	86.75
	Gaussian NB	88.17
	K-NN	78.23
	LR	86.91
	Decision Tree	94.95
	RF	91.95
	eXtreme Gradiyent Boosting	96.37
	Gradiyent Boost	96.06
	XGBoost	96.06
	MLP	93.38
Solomon vd. Method	97.16	
Nematzadeh vd. [34]	AvgPerseptron (Exhaustive Grid Search)	59.1
	FastForest(Grey Wolf Optimization)	96.9
	FastTree(Grey Wolf Optimization)	99.5
	LbfgsMxEn(Grey Wolf Optimization)	81.8
	LGBM(Grey Wolf Optimization)	99.2
	LineerSVM(Grey Wolf Optimization)	55.4
Mckensy-Sambola vd. [35]	Mckensy-Sambola vd. Method	87.0
Proposed Method	LDA-QSVM (Z Feature Map & Pauli X)	100.0
	PCA -QSVM (ZZ)	71.36

When the studies given in Table 4 are examined, it is seen that there are experiments with good performance in the analysis of the obesity dataset. However, the performance of none of these studies reached the performance of the proposed method. In this study prepared within the scope of this article, it was found that the QSVM algorithm reached maximum performance when LDA, one of the dimensionality reduction methods, was used. In the studies conducted with QSVM on different data sets, dimensionality reduction was generally performed with PCA technique. Compared to the PCA-QSVM method, the use of the LDA-QSVM method resulted in a 29% performance increase. The feature maps used in quantum classification techniques have many variations. Different quantum gates are used in each feature map. Among the feature maps used in this study, the ZZ feature map, each of which is set to two iterations, shows the lowest performance in the LDA-

QSVM method compared to the other two maps. Due to the structural properties of LDA, it causes a decrease in performance when used with the ZZ feature map. The main reason for this is that the ZZ feature map increases the complexity by using double qubits. Since the PCA algorithm has a simpler structure compared to LDA, the feature map used has less impact on the performance of QSVM.

V. CONCLUSION

This study compares the performance of classical and quantum-based machine learning algorithms for the diagnosis of obesity. In order to improve the performance of QSVM, the effects of different combinations of classical dimensionality reduction methods and quantum feature maps on performance are investigated. LDA and PCA algorithms were selected as

classical dimensionality reduction methods. With these algorithms, the data were reduced to 4 different dimensions and transformed into qubit form using quantum feature maps. Three different feature maps, ZZ, Z and Pauli X, were used. In order to compare QSVM with the classical SVM algorithm, SVM was applied to the data in bit form for 4 different dimensions. As a result of these analyses, it was determined that the proposed method as LDA-QSVM achieved 100% performance within the scope of Z and Pauli X feature maps. As a result of the literature review conducted by the authors, there is no study that has achieved this level of success with classical machine learning algorithms using the same obesity dataset. The success of a quantum machine learning algorithm in diagnosing obesity disease has an encouraging value for the use of quantum-based decision support systems in the medical field.

REFERENCES

- [1] T. L. Visscher and J. C. Seidell, 'The Public Health Impact of Obesity', *Annual Review of Public Health*, vol. 22, no. Volume 22, 2001, pp. 355–375, May 2001, doi: 10.1146/annurev.publhealth.22.1.355.
- [2] W. T. Cefalu *et al.*, 'Advances in the Science, Treatment, and Prevention of the Disease of Obesity: Reflections From a Diabetes Care Editors' Expert Forum', *Diabetes Care*, vol. 38, no. 8, pp. 1567–1582, Jul. 2015, doi: 10.2337/dc15-1081.
- [3] 'A Survey on Machine and Deep Learning Models for Childhood and Adolescent Obesity | IEEE Journals & Magazine | IEEE Xplore'. Accessed: Mar. 26, 2024. [Online]. Available: <https://ieeexplore.ieee.org/abstract/document/9627712>
- [4] I. H. Sarker, 'Machine Learning: Algorithms, Real-World Applications and Research Directions', *SN COMPUT. SCI.*, vol. 2, no. 3, p. 160, Mar. 2021, doi: 10.1007/s42979-021-00592-x.
- [5] M. Schuld, I. Sinayskiy, and F. Petruccione, 'An introduction to quantum machine learning', *Contemporary Physics*, vol. 56, no. 2, pp. 172–185, Apr. 2015, doi: 10.1080/00107514.2014.964942.
- [6] T. M. Khan and A. Robles-Kelly, 'Machine Learning: Quantum vs Classical', *IEEE Access*, vol. 8, pp. 219275–219294, 2020, doi: 10.1109/ACCESS.2020.3041719.
- [7] W. Ding and J. Wang, 'A novel approach to minimum attribute reduction based on quantum-inspired self-adaptive cooperative co-evolution', *Knowledge-Based Systems*, vol. 50, pp. 1–13, Sep. 2013, doi: 10.1016/j.knsys.2013.03.008.
- [8] W. Jia, M. Sun, J. Lian, and S. Hou, 'Feature dimensionality reduction: a review', *Complex Intell. Syst.*, vol. 8, no. 3, pp. 2663–2693, Jun. 2022, doi: 10.1007/s40747-021-00637-x.
- [9] B. Ghogh and M. Crowley, 'Unsupervised and Supervised Principal Component Analysis: Tutorial', Aug. 01, 2022, *arXiv: arXiv:1906.03148*. Accessed: Jun. 25, 2023. [Online]. Available: <http://arxiv.org/abs/1906.03148>
- [10] C. Li and B. Wang, 'Fisher Linear Discriminant Analysis'.
- [11] E. H. Houssein, Z. Abohashima, M. Elhoseny, and W. M. Mohamed, 'Machine learning in the quantum realm: The state-of-the-art, challenges, and future vision', *Expert Systems with Applications*, vol. 194, p. 116512, May 2022, doi: 10.1016/j.eswa.2022.116512.
- [12] M. Noori *et al.*, 'Analog-Quantum Feature Mapping for Machine-Learning Applications', *Phys. Rev. Appl.*, vol. 14, no. 3, p. 034034, Sep. 2020, doi: 10.1103/PhysRevApplied.14.034034.
- [13] T. Kumar, D. Kumar, and G. Singh, 'Brain Tumour Classification Using Quantum Support Vector Machine Learning Algorithm', *IETE Journal of Research*, May 2024, Accessed: Sep. 05, 2024. [Online]. Available: <https://www.tandfonline.com/doi/abs/10.1080/03772063.2023.2245350>
- [14] G. Aksoy and M. Karabatak, 'Comparison of QSVM with Other Machine Learning Algorithms on EEG Signals', in *2023 11th International Symposium on Digital Forensics and Security (ISDFS)*, May 2023, pp. 1–5. doi: 10.1109/ISDFS58141.2023.10131123.
- [15] G. Aksoy, G. Cattan, S. Chakraborty, and M. Karabatak, 'Quantum Machine-Based Decision Support System for the Detection of Schizophrenia from EEG Records', *J Med Syst*, vol. 48, no. 1, p. 29, Mar. 2024, doi: 10.1007/s10916-024-02048-0.
- [16] W. E. Maouaki, T. Said, and M. Bennai, 'Quantum Support Vector Machine for Prostate Cancer Detection: A Performance Analysis', Mar. 12, 2024, *arXiv: arXiv:2403.07856*. doi: 10.48550/arXiv.2403.07856.
- [17] M. Munshi *et al.*, 'Quantum machine learning-based framework to detect heart failures in Healthcare 4.0', *Software: Practice and Experience*, vol. 54, no. 2, pp. 168–185, 2024, doi: 10.1002/spe.3264.
- [18] Unknown, 'Estimation of obesity levels based on eating habits and physical condition'. UCI Machine Learning Repository, 2019. doi: 10.24432/C5H31Z.
- [19] F. M. Palechor and A. D. L. H. Manotas, 'Dataset for estimation of obesity levels based on eating habits and physical condition in individuals from Colombia, Peru and Mexico', *Data in Brief*, vol. 25, p. 104344, Aug. 2019, doi: 10.1016/j.dib.2019.104344.
- [20] S. Chen, Y. Dai, X. Ma, H. Peng, D. Wang, and Y. Wang, 'Personalized optimal nutrition lifestyle for self obesity management using metaalgorithms', *Sci Rep*, vol. 12, no. 1, Art. no. 1, Jul. 2022, doi: 10.1038/s41598-022-16260-w.
- [21] C. L. Urdinez Francisco, 'Principal Component Analysis', in *R for Political Data Science*, Chapman and Hall/CRC, 2020.
- [22] L. Ali, I. Wajahat, N. Amiri Golilarz, F. Keshkar, and S. A. C. Bukhari, 'LDA-GA-SVM: improved hepatocellular carcinoma prediction through dimensionality reduction and genetically optimized support vector machine', *Neural Comput & Applic*, vol. 33, no. 7, pp. 2783–2792, Apr. 2021, doi: 10.1007/s00521-020-05157-2.
- [23] 'ZZFeatureMap - Qiskit 0.44.1 documentation'. Accessed: Sep. 26, 2023. [Online]. Available: <https://qiskit.org/documentation/stubs/qiskit.circuit.library.ZZFeatureMap.html>
- [24] 'ZFeatureMap - Qiskit 0.44.1 documentation'. Accessed: Sep. 26, 2023. [Online]. Available: <https://qiskit.org/documentation/stubs/qiskit.circuit.library.ZFeatureMap.html>
- [25] 'PauliFeatureMap', IBM Quantum Documentation. Accessed: Sep. 26, 2023. [Online]. Available: <https://docs.quantum-computing.ibm.com/api/qiskit/qiskit.circuit.library.PauliFeatureMap>
- [26] S. Altares-López, A. Ribeiro, and J. J. García-Ripoll, 'Automatic design of quantum feature maps', *Quantum Sci. Technol.*, vol. 6, no. 4, p. 045015, Aug. 2021, doi: 10.1088/2058-9565/ac1ab1.
- [27] S. Agnihotri, 'Quantum Machine Learning 102 — QSVM Using Qiskit', Medium. Accessed: Sep. 26, 2023. [Online]. Available: <https://shubham-agnihotri.medium.com/quantum-machine-learning-102-qsvm-using-qiskit-731956231a54>
- [28] P. Rebenrost, M. Mohseni, and S. Lloyd, 'Quantum Support Vector Machine for Big Data Classification', *Phys. Rev. Lett.*, vol. 113, no. 13, p. 130503, Sep. 2014, doi: 10.1103/PhysRevLett.113.130503.
- [29] R. Zhang, J. Wang, N. Jiang, and Z. Wang, 'Quantum support vector machine without iteration', *Information Sciences*, vol. 635, pp. 25–41, Jul. 2023, doi: 10.1016/j.ins.2023.03.106.
- [30] Z. Abohashima, M. Elhosen, E. H. Houssein, and W. M. Mohamed, 'Classification with Quantum Machine Learning: A Survey', Jun. 22, 2020, *arXiv: arXiv:2006.12270*. doi: 10.48550/arXiv.2006.12270.
- [31] R. Kaur, R. Kumar, and M. Gupta, 'Predicting risk of obesity and meal planning to reduce the obese in adulthood using artificial intelligence', *Endocrine*, vol. 78, no. 3, pp. 458–469, Dec. 2022, doi: 10.1007/s12020-022-03215-4.
- [32] P. Putzel and S. Lee, 'Blackbox Post-Processing for Multiclass Fairness', Jan. 12, 2022, *arXiv: arXiv:2201.04461*. doi: 10.48550/arXiv.2201.04461.
- [33] D. D. Solomon *et al.*, 'Hybrid Majority Voting: Prediction and Classification Model for Obesity', *Diagnostics*, vol. 13, no. 15, Art. no. 15, Jan. 2023, doi: 10.3390/diagnostics13152610.
- [34] S. Nematzadeh, F. Kiani, M. Torkamaniafshar, and N. Aydin, 'Tuning hyperparameters of machine learning algorithms and deep neural networks using metaheuristics: A bioinformatics study on biomedical and biological cases', *Computational Biology and Chemistry*, vol. 97, p. 107619, Apr. 2022, doi: 10.1016/j.compbiolchem.2021.107619.
- [35] D. Mckensy-Sambola, M. Á. Rodríguez-García, F. García-Sánchez, and R. Valencia-García, 'Ontology-Based Nutritional Recommender System', *Applied Sciences*, vol. 12, no. 1, Art. no. 1, Jan. 2022, doi: 10.3390/app12010143.

BIOGRAPHIES



Zeynep Ozpolat received her undergraduate degree from Firat University, Department of Mathematics in 2012. She completed her master's degree at Firat University, Department of Mathematics. In 2018, she started her doctoral studies at Firat

University Software Engineering Department. She completed her doctorate education in 2023. She is currently working as a faculty member at Mus Alparslan University Software Engineering Department. Research regions; data science, quantum machine learning, deep learning, software engineering



Ozal Yildirim received his doctorate. I am a graduate of Firat University Electrical and Electronics Engineering. He is currently working as an Associate Professor in the Software Engineering Department at Firat University. He has published over 60 articles in international peer-

reviewed journals and conference proceedings. As a result of the research carried out on seven million researchers under the coordination of Stanford University, he was included in the "World's Most Influential Scientists" list. His main research interests include deep learning and medical signal and image processing.



Murat Karabatak received his doctorate. He graduated from Firat University Electrical and Electronics Engineering. He works as a professor in the Department of Software Engineering at Firat University. His main research areas are data mining,

software engineering, database systems and artificial intelligence.

Face Expression Recognition via Transformer-Based Classification Models

M. Cihad Arslanoglu, Huseyin Acar and Abdulkadir Albayrak


Abstract—Facial Expression Recognition (FER) tasks have widely studied in the literature since it has many applications. Fast development of technology in deep learning computer vision algorithms, especially, transformer-based classification models, makes it hard to select most appropriate models. Using complex model may increase accuracy performance but decreasing inference time which is a crucial in near real-time applications. On the other hand, small models may not give desired results. In this study, it is aimed to examine accuracy and data process time performance of 5 different relatively small transformer-based image classification algorithms for FER tasks. Used models are vanilla Vision Transformer (ViT), Pooling-based Vision Transformer (PiT), Shifted Windows Transformer (Swin), Data-efficient image Transformers (DeiT), and Cross-attention Vision Transformer (CrossViT) with considering their trainable parameter size and architectures. Each model has 20-30M trainable parameters which means relatively small. Moreover, each model has different architectures. As an illustration, CrossViT focuses on image using multi-scale patches and PiT model introduces convolution layers and pooling techniques to vanilla ViT model. Model performances are evaluated on CK+48 and KDEF datasets that are well-known and most used in the literature. It was observed that all models exhibit similar performance with literature results. PiT model that includes both Convolutional Neural Network (CNN) and Transformer layers achieved the best accuracy scores 0.9513 and 0.9090 for CK+48 and KDEF datasets, respectively. It shows CNN layers boost performance of Transformer based models and help to learn data more efficiently for CK+48 and KDEF datasets. Swin Transformer performs 0.9080 worst accuracy score for CK+48 dataset and 0.8434 nearly worst score for KDEF dataset. Swin Transformer and PiT exhibit worst and best image processing performance in terms of spent time, respectively. This makes PiT model suitable for real-time applications too. Moreover, PiT model require 25 and 83 second least training epoch to reach these performance for CK+48 and KDEF, respectively.


Index Terms—FER, Transformers, ViT, Classification


I. INTRODUCTION

FACIAL expressions are universal communication skills independent of country, language or ethnicity for the people. Human facial mimics convey a rich information about emotions, behaviors, and so on [1]. Many disciplines study

facial expressions such as psychology [2] and marketing [3]. Tang et al. proposed a real-time system to evaluate the performance of students in a classroom using their facial expressions [4]. Sajjad et al. designed a framework to detect suspicious persons using facial expressions for smart security in law enforcement services [5]. Fu et al. evaluated whether there is a relation between being depressive and facial expressions. They showed that depressive people have poor ability to imitate facial expressions [6]. Since facial expressions play a significant role in many fields, Facial Expression Recognition (FER) has been of keen interest in computer vision and machine learning. Humans represent their facial expressions in many forms like being happy, less happy, or happier. In computer vision and machine learning, however, they are restricted in 6-8 essential form. Ekman and Friesen proposed to use 6 basic forms of emotions, which are anger, disgust, fear, happiness, sadness and surprise [7]. There are many techniques for FER tasks in the literature. However, all of them are categorized in two groups: geometric and appearance-based feature extraction algorithms. While geometric-based methods utilize the face landmarks of humans, appearance-based algorithms use texture, shape, and color-based features. Sheth et al. stated that geometric-based features outperform appearance-based feature extraction techniques [8]. Moreover, combining both appearance and geometric based features improve accuracy for FER tasks [9], [10], [11]. In geometric feature extraction approaches, the aim is to find a relationship between human mimics and facial expressions [12]. Geometric-based FER applications have two steps: face landmark detection and facial expression recognition. In face landmark detection stage, mimic points like eyes, mouth, and nose are detected and many statistical features are calculated such as distance between eyebrow and area of mouth. After the detection stage, obtained features are fed into a classifier to detect facial expression. In appearance-based FER algorithms, texture, color, and shape information are extracted from human face. There are two kinds of appearance-based feature extraction algorithms: deep learning and hand-crafted features. These two approaches have advantages and disadvantages. Hand-crafted feature extraction algorithms are easy to implement in terms of time and complexity. However, they have lack of adaptiveness for different conditions such as environment, human ethnicity, and so on. On the other hand, deep learning algorithms are able to learn these kinds of different cases. This strong learning ability comes with greater complexity. Deep learning methods need more computational power, data and time to yield competitive results. One of the most used deep learning algorithms in computer vision and FER tasks is CNNs. CNNs apply n_{xn}

 **M.Cihad ARSLANOĞLU** is with the Department of Electrical and Electronics Engineering, Engineering Faculty, Dicle University, Diyarbakir, 21280 TURKEY e-mail: cihatdt.21@gmail.com

 **Hüseyin ACAR** is with the Department of Electrical and Electronics Engineering, Engineering Faculty, Dicle University, Diyarbakir, 21280 TURKEY e-mail: hacar@dicle.edu.tr

 **Abdülkadir ALBAYRAK** is with the Department of Computer Engineering, Engineering Faculty, Dicle University, Diyarbakir, 21280 TURKEY e-mail: kadir.albayrak@dicle.edu.tr

Manuscript received May 18, 2024; accepted August 20, 2024. DOI:10.17694/bajece.1486140

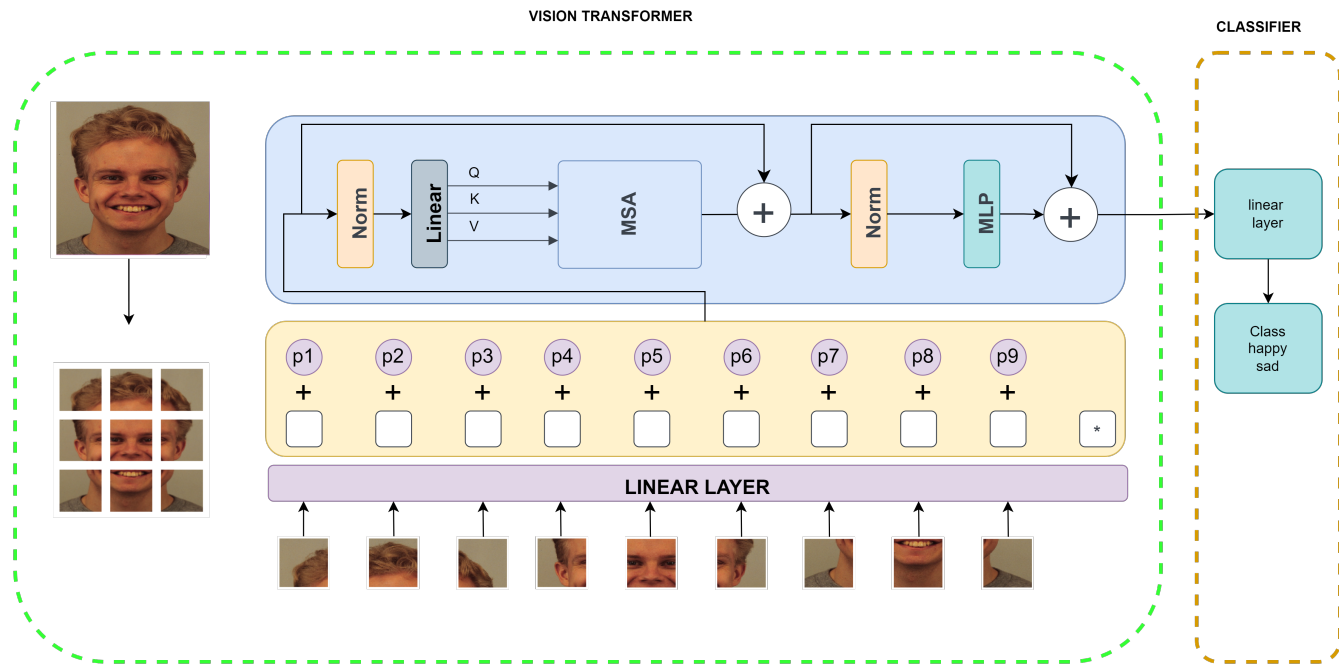


Fig. 1: High level architecture of ViT algorithm. ViT algorithm splits an image into equal sized patches. To calculate global embeddings and reduce data size, a linear layer is applied to each patch. Positional encoding values are added to each patch due to emphasize importance of their positions. These embeddings are given to multi-head attention mechanism and MLP block which includes linear layer and GeLU activation function. At the last stage, embeddings are given to a classifier which is a linear layer.

filters to input images to capture meaningful local features like shape, color, and texture. It uses pooling layers to decrease dimensions of input image to eliminate useless features and decrease computational complexity. CNNs provide more representative and less complex feature vector at the last layer. A classifier is fed with this obtained feature vector to detect facial expression. Vision Transformer (ViT) [13] is a Transformer-based, which is proposed for Natural Language Processing (NLP) task by Vaswani et al. [14], classification algorithm. ViT algorithm focuses on global dependencies of the images unlike CNNs. ViT algorithm divides an image into patches instead of processing it as a whole. Linear layers are applied to these patches to capture most representative features of image and decrease size of raw data. Then, a similarity metric, which is cosine similarity, is calculated between these all patches which is named as attention map. ViT algorithm uses this attention map to eliminate less valuable features like noise and gives a feature vector at the end of the processes. Obtained feature vectors are given to a classifier to detect facial expression of human. Although ViT algorithm outperform CNN based methods, it has a couple of disadvantages. ViT algorithm has $O(N^2)$ computation complexity which makes ViT training harder and time inefficient. Anasosalu et al. introduce a new token mixing operator, which is called RepMixer, to solve time latency problem without accuracy reduction [15]. Liu et al propose a hierarchical shifting window to capture non-overlapping features and local features with linear complexity increment. In this paper, FER accuracy and spent time performance of five different ViT models which are vanilla ViT [13],

Swin Transformer [16], CrossViT[17], PiT [18] and Deit [19] were compared. The performances of these used models are evaluated on two different datasets that are CK+48 and KDEF. The main contributions of this study are listed below:

- Accuracy and image process time performance of five different transformer-based models were compared.
- Each experiments were repeated five times to be sure about performance consistency and experiment reproducibility.
- Loss function plots and accuracy score of used models are evaluated due to reveal overfitting problem.
- Four different evaluation metrics were used to be sure about the results and see if there is a problem about results such as unbalanced data issue.
- Obtained results were compared with the literature.

II. RELATED WORKS

Related works were split into two subtitle that are hand-crafted methods and deep learning approaches. Hand-crafted methods also have different approaches such as appearance and geometric-based feature extraction. However, they were examined under same title that is hand-crafted methods.

A. Hand-crafted Methods

In [20], [21] geometric features are extracted and given to Hidden Markov Model (HMM) and Support Vector Machine (SVM) to classify. Rahul et al. achieves 84.7% accuracy score for Japanese Female Facial Expression (JAFFE) dataset [20].

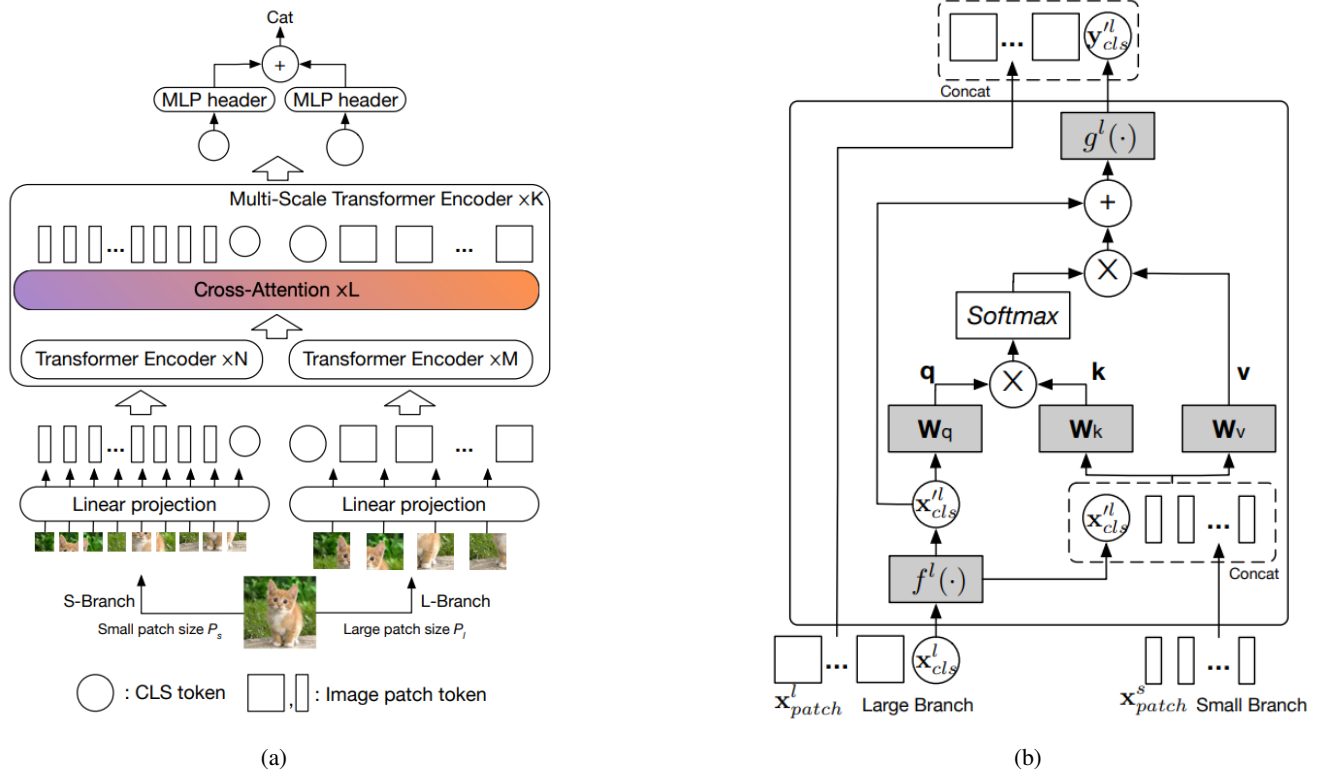


Fig. 2: (a) high level architecture of CrossViT algorithm. (b) high level architecture of cross-attention fusion approach [17]

Chouhayebi et al. states that they obtained 94.5% accuracy score for fusion of private and Bogazici University Head Motion Analysis Project (BUHMAP) datasets [21]. Sharma et al. apply preprocessing Gaussian filter for noise removal and contrast histogram equalization for illumination correction before detecting geometric features and classification [22]. Sharma et al. accomplish 95.5% accuracy score for Multi-media Understanding Group (MUG) dataset. Ibrahim et al. crop face of image that helps to extract most representative features. Then Histogram of Oriented Gradient (HOG) and Local Binary Pattern (LBP) algorithms are applied to extract features of the face. At the classification stage, obtained feature vectors are fed into SVM classifier [23]. Ibrahim et al. achieves 95.17% accuracy score for JAFFE dataset. Kaya et al. align face of image Generalized Procrustes Analysis (GPA) to obtain good face representation. Then many feature extraction methods like HOG, LBP Speedup Robust Features (SIFT), Local Phase Quantization (LPQ) are applied to aligned images. At the classification stage, two classification algorithms which are Extreme Learning Machine (ELM) and Partial Least Squares (PLS) are trained and their decisions are fused in the test stage [24]. The proposed method performs 53.62% accuracy score EmotiW 2015 dataset.

B. Deep Learning Approaches

Liu et al. gives a video to CNN and Global Attention Unit to extract spatial features and use Bidirectional Long Short-Term Memory (BiLSTM) to capture temporal variations from previous layers. At last stage, Attention pooling is applied and

given to classification layer [25]. In the paper, it is stated that the proposed algorithm exhibits 99.54%, 88.33%, 87.06%, and 63.71% accuracy score performance for CK+48, OuluCASIA, MMI, and AffectNet, respectively. Pan et al. extract spatial and temporal features giving frames of a video to two model stacks which consist of CNN and Long Short-Term Memory (LSTM) models sequentially. Obtained feature vectors from two models stacks are aggregated using proposed aggregation layer. A SoftMax activation layer is applied to aggregated feature vectors and classified [26]. Pant et al. declare that proposed method achieves 65.72% and 42.98% accuracy scores for RML and eNTERFACE datasets. Uddin et al. uses depth cameras to capture images instead of conventional RGB cameras. They train a CNN based classification algorithm using hand-crafted features like Local Directional Rank Histogram Pattern (LDRHP), Local Directional Strength Pattern (LDSP), and Generalized Discriminant Analysis (GDA) [27]. Uddin et al. obtained 95.42% and 96.25% accuracy scores for CK and Bosphorus datasets. Minaee et al. states that there is no need very deep CNN models for FER tasks and propose two CNN model that has four and two convolution layers, respectively. Second CNN model is named as localization network. An affine transform applied to feature vectors that is obtained by localization network and multiplied with feature vectors of first model. In the classification stage, a linear layer is applied to the feature vector and classified using linear layer and SoftMax activation function [28]. Minaee et al. achieves 70.02%, 98.0%, 99.3%, and 92.8% accuracy scores for Facial Expression Recognition 2013 (FER2013), CK+48, Facial

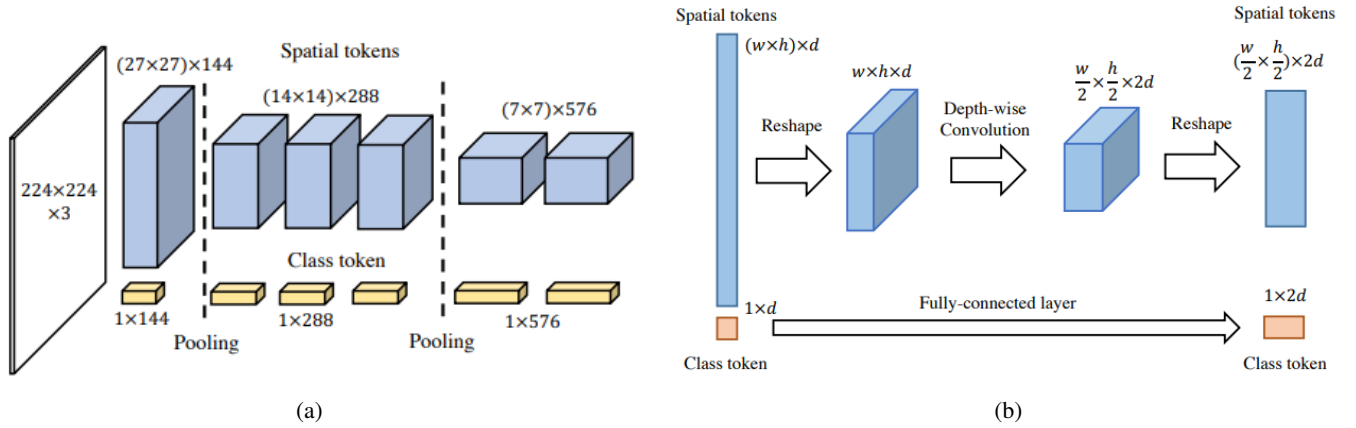


Fig. 3: (a) shows high-level architecture of PiT algorithm. In (b), PiT pooling layer is displayed [18]

Expression Research Group (FERG), and JAFFE datasets.

III. MATERIAL AND METHODS

ViT is a transformer-based image classification algorithm. Dosovitskiy et al. proposed ViT algorithm by inspiring attention mechanism based transformer architecture which is designed for NLP by Vaswani et al. [14]. ViT algorithm has three main stages: patch embedding, attention mechanism and classification. In patch embedding, an image with $W \times H \times C$ size is shaped into $L \times (n \times n) \times C$ where L is patch number, n is patch size, and C is channel size. A linear layer is applied to each to obtain embeddings and reduce patch size. To specify where each patch belongs to, positional encoding values are added to output of linear layer. In attention mechanism, attention matrix, cosine similarity between all patch embeddings, is calculated. Then attention matrix is multiplied by embeddings to weight embeddings. A MLP block which has linear layer and Gaussian Error Linear Unit (GeLU) activation function is applied to embeddings due to enhance embeddings. As a result, these obtained embeddings are given to a classifier at the classification stage. Figure 1 shows high level architecture of ViT algorithm.

A. CrossViT

Vanilla ViT model requires many data for efficient training since it focuses on global dependencies. CrossViT algorithm focuses on both global and local embedding tokens by using two level patch size. In patch embedding phase, CrossViT algorithm splits the image into $m \times m$ and $n \times n$ sized patches. These patches are given to cross-attention module that includes a fusion approach to combine both different sized patches and reduce computation complexity. CrossViT algorithm and cross-attention illustrations are given in Figure 2a and 2b, respectively.

B. PiT

Heo et al. state that adding spatial dimension reduction in ResNet CNN-based deep learning algorithm improves accuracy score and decrease validation loss in training stage [18].

ViT does not have any spatial reduction layer unlike CNN-based algorithms. PiT algorithm uses a pooling layer to utilize advantages of spatial dimension reduction. Proposed pooling layer apply a couple of depth-wise convolution operation in ViT's patch embedding stage and obtain 3D tensors unlike 2D matrix like vanilla ViT. These 3D tensors are reshaped into 2D matrix before transformer architecture and ViT procedure is sustained. High-level architecture of PiT and pooling layer were provided in Figure 3a and 3b, respectively.

C. DeiT

ViT algorithm needs million-level images to learn image representation embeddings efficiently. This makes ViT hard learner and hardware inefficient deep learning model. Touvron et al. proposes a distillation token and label distillation techniques with using teacher-student relation in order to decrease these data and hardware requirements [19]. In DeiT architecture, a distillation token is concatenated with patch embeddings. In backpropagation, layer teacher and student model decisions are combined using soft distillation and hard-label distillation approaches like in Equation 1 and 2, respectively. In Equation 1 and 2, \mathcal{L}_{CE} is cross-entropy, KL is Kullback-Leibler (KL) loss, λ is coefficient to balance KL and cross-entropy, ψ is softmax function, Z_s is student model logits, τ is distillation temperature, Z_t is teacher model logits, and y_t is decision of teacher model.

$$\mathcal{L}_{global} = (1 - \lambda) \cdot \mathcal{L}_{CE}(\psi(Z_s), y) + \lambda \cdot \tau^2 \cdot KL\left(\psi\left(\frac{Z_s}{\tau}\right), \psi\left(\frac{Z_t}{\tau}\right)\right) \quad (1)$$

$$\mathcal{L}_{global}^{hardDistill} = \frac{1}{2} \cdot \mathcal{L}_{CE}(\psi(Z_s), y) + \frac{1}{2} \cdot \mathcal{L}_{CE}(\psi(Z_s), y_t) \quad (2)$$

D. Swin Transformer

Since ViT focuses on all global dependencies between each patch, it has N^2 computational complexity where N is patch size. Moreover, ViT does not focus on hierarchical relations in the image. Liu et al. proposes Swin transformer with shifted

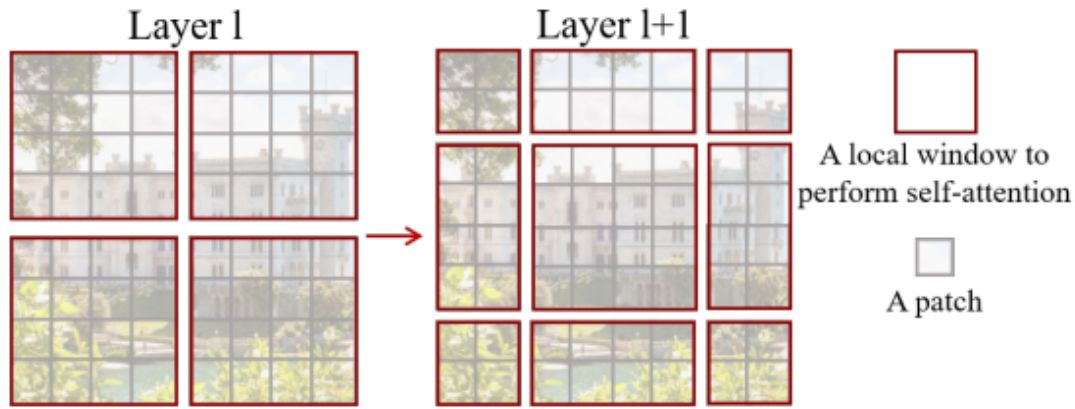


Fig. 4: Non-overlapping shifted window architecture [16]

non-overlapping window and Swin transformer block to reduce computation complexity and reveal hierarchical relations in the image [16]. Given input image is split into patches like ViT but with small patch size like 4x4. Linear layer is applied to each patch with C output size and obtained $\frac{H}{4} \times \frac{W}{4}$ times patch embeddings. In order to reduce attention mechanism computation complexity, a modified attention mechanism, called Swin Transformer Block, is used to calculate relations between patches. Swin transformer block apply conventional transformer block for only some patches that is in a non-overlapping window. Non-overlapping window includes M patches where M is initialized as 4. In the other words, each non-overlapping window possess $4C$ times patch embeddings. This proposed Swin transformer block reduce computation complexity from $4hwC^2 + 2(hw)^2 C$ to $4hwC^2 + 2M^2hwC$ where h and w are height and width of the image, M is patch size in the non-overlapping window, and C is patch embedding size. Later on, merging layer is applied to each window separately. Merge layer concatenate each patch in the non-overlapping window and apply linear layer in order to decrease embedding size to $2C$ from $4C$. This sequential process is applied to n times to output of each swin transformer block with shifting non-overlapping window as illustrated in Figure 4. High-level architecture of Swin transformer is shown in Figure 5.

IV. RESULTS AND DISCUSSION

A. Dataset

To evaluate transformer based five different classification algorithms, two well-known and commonly used datasets that are Karolinska Directed Emotional Faces (KDEF) and Extended Cohn-Kanade (CK+48) were used. Both datasets were split into train and test datasets with 80% and 20% rate, respectively.

1) *KDEF*: KDEF dataset is provided to literature by Karolinska Institute in 2008 [29]. KDEF dataset includes 4900 images that is taken from 35 male and 35 female individuals in laboratory conditions. Each class have same sample size that is 700. Obtained images has same shape and it is 562x762x3 where 562 is width, 762 is height and 3 is channel size. Dataset

has 7 emotion state: afraid, angry, disgusted, sad, happy surprised, and neutral. Captured image is taken in 5 different views: full left profile, half left profile, straight, half right profile, and full right profile. Sample images with different views from KDEF dataset were illustrated in Figure 6. AF, AN, DIS, HAP, NEU, SAD, and SUP abbreviations represent afraid, angry, disgusted, happy, neutral, sad, and surprised, respectively. FLP, HFP, FSP, HRP, and FRP indicates full left profile, half left profile, full straight profile, half right profile, and full right profile.

2) *CK+48*: CK+48 dataset is created by Luckey et al. in 2010 as extension of Cohn-Kanade dataset [30]. The dataset contains 981 images with 48x48x3 shape and seven classes. Class names their sample sizes are following 75 afraid, 135 angry, 177 disgusted, 84 sad, 207 happy, 249 surprised, and 54 neutral. Sample images from CK+48 were given in Figure 7. AF, AN, DIS, HAP, NEU, SAD, and SUP abbreviations represent afraid, angry, disgusted, happy, neutral, sad, and surprised, respectively.

B. Setup

All experiments were done using Python programming language and PyTorch [31] deep learning framework. A couple of important parameters such as input size and patch size were shared in Table I. Input column represents input size of images. Patch column indicates how many patches are extracted from the input image. CrossViT has two patch size since it uses multi-scale patches. Total model trainable parameter numbers and their architectures were cared to select transformer-based classification algorithms. Table I 'params' column display total trainable parameters size of models. 'img/sec [GPU]' and 'img/sec [CPU]' columns mean that how many images are processed in one second with GPU and CPU hardware, respectively. Timm implementation of used deep learning models that is pretrained on Imagenet1k dataset were fine tuned instead of from scratch training. ImageNet1k dataset has 1000 classes with over 1 million images. All models were trained until train accuracy reaches up to 98%. The average number of epochs needed to achieve 0.98 train accuracy score is shared in 'epoch' column of Table II. CrossViT, DeiT, PiT, Swin

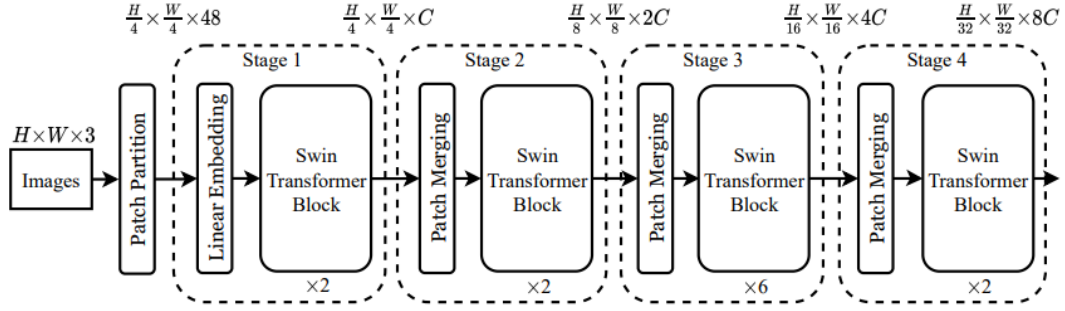


Fig. 5: High-level architecture of Swin Transformer[16]

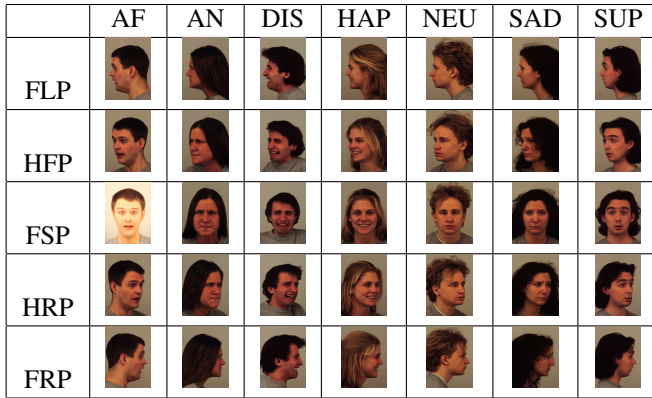


Fig. 6: Sample images from KDEF dataset.

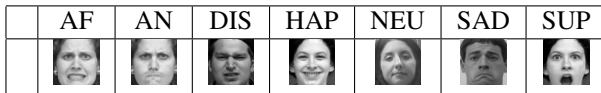


Fig. 7: Sample images from CK+48 dataset.

TABLE I: Parameters of used models

Model	Input	Patch	Embeddings	Head	Depth	params (M)	img/sec [GPU]	img/sec [CPU]
CrossViT	240x240	(12,16)	(192,384)	(6,6)	(1,4,0)	26.9	red	5
DeiT	224x224	16	384	6	12	22.0	120	6
PiT	224x224	16	(48,48,48)	(3,6,12)	(2,6,4)	23.5	160	9
Swin	256x256	16	96	(3,6,12,24)	(2,2,6,2)	28.3	48	2
ViT	224x224	16	192	3	12	22.1	119	6

Transformer, and ViT algorithms achieved a training accuracy of 98% after approximately 12, 32, 25, 93, and 42 epochs, respectively, on the CK+48 dataset. When applied to the KDEF dataset, the ordered algorithms reached the same 98% accuracy after 15, 105, 83, 100, and 106 epochs, respectively. Stochastic Gradient Descent (SGD) optimization algorithm was used with linearly decreased learning rate from 0.1 to 0.01 throughout first 30 epochs. It was observed that training the models with constant learning rate increase training time to reach 98% train accuracy. Batch size was set to 32 for all experiments. All models are trained and tested on Google Colab environment with following hardware specifications: 16GB Random Access Memory (RAM), Intel(R) Xeon(R) CPU @ 2.20GHz and Tesla T4 GPU with 16gb Memory. All experiments were done five times to be sure about consistency and reproducibility of the results.

1) *Evaluation Metrics*: Four metrics that are accuracy, precision, recall, and F1 were used in order to compare performance of used models. Definition of used evaluation metrics were given in Equation 3, 4, 5, and 6. Accuracy score measure how many data is correctly predicted by the model. It is calculated dividing True Positive (TP) plus True Negative (TN) to sum of True Positive (TP), True Negative (TN), False Positive (FP), and False Negative (FN) like in Equation 3. A high accuracy score indicates the model is capable to classify data correctly. Although accuracy score is a suitable metric to evaluate balanced datasets, it is specious when data is not balanced.

$$A = \frac{TP + TN}{TP + TN + FP + FN} \quad (3)$$

Unlike accuracy score, precision focuses on how much model is well to predict target, TP, instead of others like TN. Precision is not affected by unbalanced datasets since it does not focus on other classes except target one. It is calculated as in Equation 4.

$$P = \frac{TP}{TP + FP} \quad (4)$$

Recall score does not take account FP predictions which means how many data is predicted as target class when they are not target class. Its calculation formula was given in Equation 5.

$$R = \frac{TP}{TP + FN} \quad (5)$$

F1 combines both recall and precision score and yields a single value. Since F1 is a tradeoff between recall and precision scores, it provides a more reliable result. It is calculated like in Equation 6.

$$F1 = 2 \cdot \frac{P \cdot R}{P + R} \quad (6)$$

Table I 'img/sec [GPU]' and 'img/sec [CPU]' columns reveal that PiT and Swin Transformer models has most and least image processing capability in a second for GPU and CPU, respectively. While PiT process 160 images in a second, Swin Transformer has 48 image processing capability on GPU hardware. On the other hand, same models process 9 and 2 images in a second for CPU hardware.

Obtained average performance metrics of five different experiments were shared in Table II for both CK+48 and

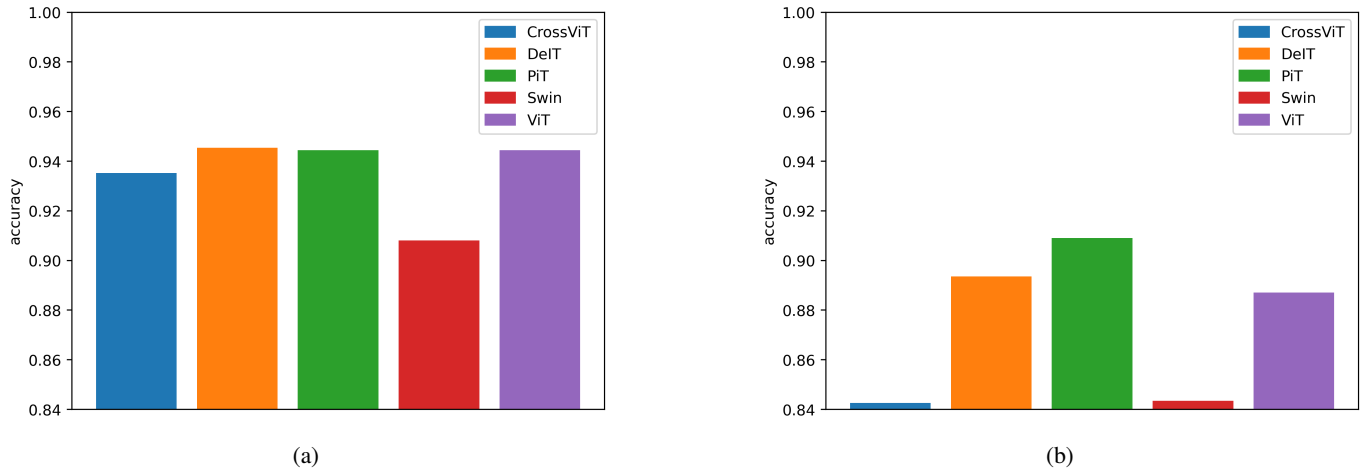


Fig. 8: (a) and (b) represents accuracy scores of CK+48 and KDEF test datasets, respectively.

TABLE II: Performance of models for both CK+48 and KDEF datasets.

	CK+48					KDEF				
	Accuracy	Precision	Recall	F1	epoch	Accuracy	Precision	Recall	F1	epoch
CrossViT	0.9463±0.027	0.9459±0.029	0.9465±0.031	0.9454±0.031	12	0.8426±0.011	0.8447±0.010	0.8426±0.011	0.8426±0.011	15
DeIT	0.9400±0.020	0.9389±0.026	0.9389±0.019	0.9394±0.025	32	0.8935±0.005	0.8944±0.005	0.8936±0.005	0.8935±0.0056	105
PiT	0.9513±0.023	0.9504±0.030	0.9498±0.021	0.9514±0.029	25	0.9090±0.012	0.9101±0.012	0.9091±0.012	0.9089±0.0125	83
Swin	0.9080±0.042	0.8869±0.050	0.8843±0.045	0.9076±0.050	93	0.8434±0.004	0.8449±0.005	0.8435±0.046	0.8428±0.0050	100
ViT	0.9444±0.004	0.9429±0.009	0.9424±0.012	0.9440±0.007	42	0.8871±0.010	0.8871±0.011	0.8872±0.010	0.8866±0.011	106

TABLE III: Studies from the literature

Study	Dataset	Accuracy
Wang et. al [32]	CK+48	0.9284
Subud et. al [33]	CK+48	0.9987
Kim et. al [11]	CK+48	0.9646
Yu et. al [34]	CK+48	0.9410
Hu et. al [35]	CK+48	0.9407
Mohan et. al [36]	CK+48	0.9800
Kumar et. al [37]	CK+48	0.9420
Kas et. al [38]	CK+48	0.9648
This study	CK+48	0.9513
Subud et. al [33]	KDEF	0.9689
Eng et. al [39]	KDEF	0.8095
Puthanidam et. al [40]	KDEF	0.8958
Mohan et. al [36]	KDEF	0.8300
Kumar et. al [37]	KDEF	0.9370
Obait et. al [41]	KDEF	0.9529
Kas et. al [38]	KDEF	0.9020
Yaddaden et. al [42]	KDEF	0.8458
Barra et. al [43]	KDEF	0.8271
This study	KDEF	0.9090

KDEF datasets. The notation in Table II is that accuracy $\pm \sigma$ where σ is standard deviation of 5 experiment. It is clearly seen standard deviation of all results are less than 0.06 which means results are consistent. The best results for both CK+48 and KDEF datasets are obtained by PiT transformer architecture. PiT architecture achieves average best 0.9513 and 0.9090 accuracy scores for CK+48 and KDEF test datasets, respectively. Meanwhile, Table II also shows that the steadiest models, in terms of accuracy standard deviation, are vanilla ViT and Swin for CK+48 and KDEF datasets, respectively. Recall, precision and F1 are also near to accuracy and stable. CrossViT model reaches its the best scores with least epoch compared to other models. Swin Transformer and vanilla ViT algorithms need

the most training epochs for CK+48 and KDEF datasets, respectively. Average scores of five experiments also were displayed in Figure 8a and 8b for CK+48 and KDEF datasets, respectively. Figure 8a and 8b reveals that Swin Transformer architecture exhibit the worst accuracy scores compared to other models. It is also possible to see most unstable models, in terms of accuracy standard deviation, are Swin Transformer and PiT for CK+48 and KDEF datasets, respectively. train loss and accuracy plots at every epoch were shared in in Figure 9 and Figure 10 for CK+48 and KDEF datasets, respectively. Figure 9a and 10a shows that CrossViT achieves the best train accuracy score and least train loss. However, it does not outperform other all models for test datasets.

Model selection in deep learning plays a significant role for many tasks including FER. It has a lot of effects on results and progress such as inference time, training time, test accuracy, and so on. Using complex models may increase the accuracy performance. However, complex models need to expensive hardware requirements and they have more inference time that hinder near real-time processing. Small models may run on low-level hardware. However, generally they are less accurate than complex models. Model selection has direct effect on budget, accuracy performance, inference time, and so on. All possible models should be evaluated to find optimal model to solve aimed tasks. Table I and II shows that although CrossViT has more parameter than DeIT, it is not able to outperform DeIT model. Moreover, Figure 9 and 10 reveal that CrossViT algorithm has lack of generalization capability since it learns train data so fast with less loss values but it is not able to exhibit same performance on test dataset. Although Swin Transformer has most parameter size, it achieves less performance than most of other models for both datasets. It

means using complex model is not solution at every time. Moreover, Swin Transformer has more inference time since it has hierarchical feature extraction and concatenation layers. PiT model, has convolution layers to extract embeddings, outperforms vanilla ViT that means using convolution layers to extract embeddings from the image helps to learn more useful features. Since convolution layers tends to extract local low-level features in its early layers [44], PiT combines local low-level features with ViT's global embedding extraction mechanism. All individual models have near accuracy, precision, recall and F1. Literature results for both CK+48 and KDEF datasets were shared in Table III. First column indicates the study, second column shows which dataset was used and the last column displays accuracy score of the studies. Although some studies perform better and worse compared to used Transformer based algorithms, It is seen that Transformer-based algorithms exhibit similar accuracy score compared to the literature.

In this paper, it is aimed to compare Transformer-based different image classification models for FER task. The five models that have different architectures but almost same trainable parameter sizes were selected. CK+48 and KDEF datasets were used to evaluate FER performance of proposed approaches. Experiment results show that although models have roughly same learnable parameter numbers, model performances and data processing time differ each other. It reveals that model architectures play an important role in performance in terms of accuracy and image processing capability. CNN and Transformer based hybrid PiT model outperforms all other models for both CK+48 and KDEF datasets in terms of accuracy. Moreover, PiT model has most image processing capability in one second. That makes PiT model suitable to use in FER applications. On the other hand, Swin transformer has worst image processing capability in one second. Swin Transformer and ViT model exhibit worst accuracy score for CK+48 and KDEF datasets, respectively. In further studies, domain specific datasets can be used for pretraining stage before transfer learning to increase performance of models. It is also possible to measure and compare accuracy and running time performance of Transformer and CNN based models.

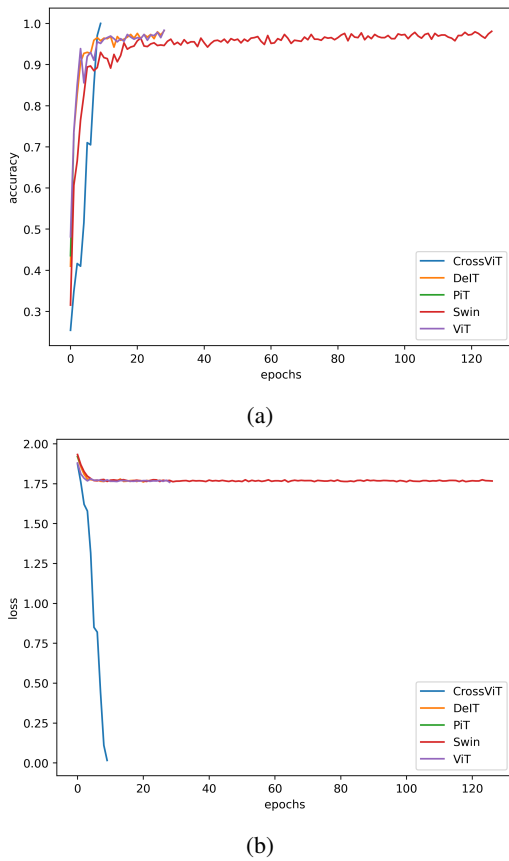


Fig. 9: (a) and (b) represent train accuracy and loss plots with respect to trained epoch for CK+48 dataset.

V. CONCLUSION

Facial Expression Recognition is an important study field in the literature. Human face mimics and their emotions are widely used such as human-computer interaction. To determine best models in terms of accuracy and running speed is important to develop suitable applications.

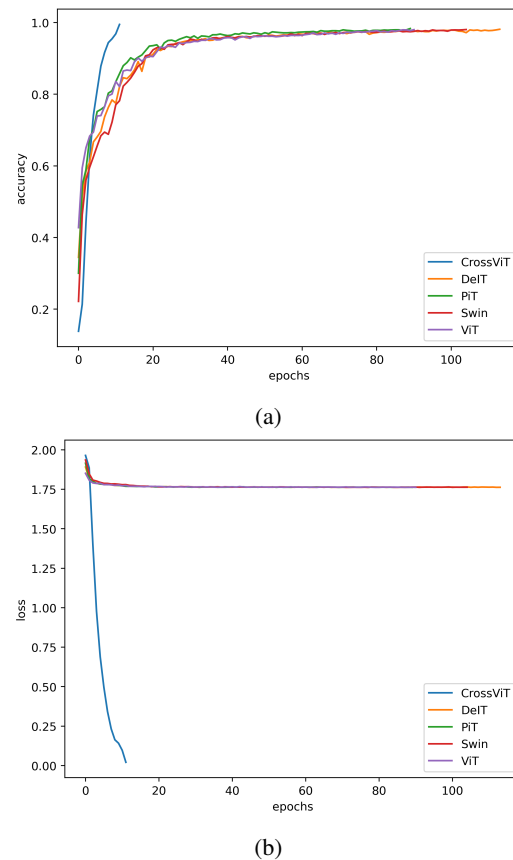


Fig. 10: (a) and (b) represent train accuracy and loss plots with respect to trained epoch for KDEF dataset.

REFERENCES

- [1] P. Ekman, "Facial expression and emotion." *American Psychologist*, vol. 48, no. 4, pp. 384–392, 1993. [Online]. Available: <https://doi.org/doi/10.1037/0003-066X.48.4.384>
- [2] L. E. Ishii, J. C. Nellis, K. D. Boahene, P. Byrne, and M. Ishii, "The importance and psychology of facial expression," *Otolaryngologic Clinics of North America*, vol. 51, no. 6, pp. 1011–1017, 2018-12. [Online]. Available: <https://linkinghub.elsevier.com/retrieve/pii/S003066651830121X>
- [3] G. S. Shergill, A. Sarrafzadeh, O. Diegel, and A. Shekar, "Computerized sales assistants: the application of computer technology to measure consumer interest-a conceptual framework," 2008, publisher: California State University.
- [4] X.-Y. Tang, W.-Y. Peng, S.-R. Liu, and J.-W. Xiong, "Classroom teaching evaluation based on facial expression recognition," in *Proceedings of the 2020 9th International Conference on Educational and Information Technology*, ser. ICEIT 2020. Association for Computing Machinery, 2020-04-23, pp. 62–67. [Online]. Available: <https://doi.org/10.1145/3383923.3383949>
- [5] M. Sajjad, M. Nasir, F. U. M. Ullah, K. Muhammad, A. K. Sangaiah, and S. W. Baik, "Rasberry pi assisted facial expression recognition framework for smart security in law-enforcement services," *Information Sciences*, vol. 479, pp. 416–431, 2019-04. [Online]. Available: <https://linkinghub.elsevier.com/retrieve/pii/S0020025518305425>
- [6] G. Fu, Y. Yu, J. Ye, Y. Zheng, W. Li, N. Cui, and Q. Wang, "A method for diagnosing depression: Facial expression mimicry is evaluated by facial expression recognition," *Journal of Affective Disorders*, vol. 323, pp. 809–818, 2023-02. [Online]. Available: <https://linkinghub.elsevier.com/retrieve/pii/S016503272201388X>
- [7] P. Ekman and W. V. Friesen, "Constants across cultures in the face and emotion," *Journal of Personality and Social Psychology*, vol. 17, pp. 124–129, 1971, place: US Publisher: American Psychological Association.
- [8] N. A. Sheth and M. M. Goyani, "A comprehensive study of geometric and appearance based facial expression recognition methods," *Int J Sci Res Sci Eng Technol*, vol. 4, no. 2, pp. 163–175, 2018-01-20. [Online]. Available: <https://ijsrset.com/IJSRSET184229>
- [9] T. Gwyn, K. Roy, and M. Atay, "Face recognition using popular deep net architectures: A brief comparative study," *Future Internet*, vol. 13, no. 7, p. 164, 2021.
- [10] A. Saeed, A. Al-Hamadi, R. Niese, and M. Elzobi, "Frame-based facial expression recognition using geometrical features," *Adv. in Hum.-Comp. Int.*, vol. 2014, p. 4-4, 2014-01-01. [Online]. Available: <https://doi.org/10.1155/2014/408953>
- [11] J.-H. Kim, B.-G. Kim, P. P. Roy, and D.-M. Jeong, "Efficient facial expression recognition algorithm based on hierarchical deep neural network structure," *IEEE Access*, vol. 7, pp. 41 273–41 285, 2019, conference Name: IEEE Access.
- [12] A. Barman and P. Dutta, "Facial expression recognition using distance and shape signature features," *Pattern Recognition Letters*, vol. 145, pp. 254–261, 2021-05. [Online]. Available: <https://linkinghub.elsevier.com/retrieve/pii/S0167865517302246>
- [13] A. Dosovitskiy, L. Beyer, A. Kolesnikov, D. Weissenborn, X. Zhai, T. Unterthiner, M. Dehghani, M. Minderer, G. Heigold, S. Gelly *et al.*, "An image is worth 16x16 words: Transformers for image recognition at scale," *arXiv preprint arXiv:2010.11929*, 2020.
- [14] A. Vaswani, N. Shazeer, N. Parmar, J. Uszkoreit, L. Jones, A. N. Gomez, L. Kaiser, and I. Polosukhin, "Attention is all you need," 2023-08-01. [Online]. Available: <http://arxiv.org/abs/1706.03762>
- [15] P. K. A. Vasu, J. Gabriel, J. Zhu, O. Tuzel, and A. Ranjan, "FastViT: A fast hybrid vision transformer using structural reparameterization," 2023-08-17. [Online]. Available: <http://arxiv.org/abs/2303.14189>
- [16] Z. Liu, Y. Lin, Y. Cao, H. Hu, Y. Wei, Z. Zhang, S. Lin, and B. Guo, "Swin transformer: Hierarchical vision transformer using shifted windows," in *Proceedings of the IEEE/CVF international conference on computer vision*, 2021, pp. 10012–10022.
- [17] C.-F. Chen, Q. Fan, and R. Panda, "CrossViT: Cross-attention multi-scale vision transformer for image classification," 2021-08-22. [Online]. Available: <http://arxiv.org/abs/2103.14899>
- [18] B. Heo, S. Yun, D. Han, S. Chun, J. Choe, and S. J. Oh, "Rethinking spatial dimensions of vision transformers," 2021-08-17. [Online]. Available: <http://arxiv.org/abs/2103.16302>
- [19] H. Touvron, M. Cord, M. Douze, F. Massa, A. Sablayrolles, and H. Jégou, "Training data-efficient image transformers & distillation through attention," 2021-01-15. [Online]. Available: <http://arxiv.org/abs/2012.12877>
- [20] M. Rahul, N. Kohli, R. Agarwal, and S. Mishra, "Facial expression recognition using geometric features and modified hidden markov model," *International Journal of Grid and Utility Computing*, vol. 10, no. 5, pp. 488–496, 2019-01, publisher: Inderscience Publishers. [Online]. Available: <https://www.inderscienceonline.com/doi/abs/10.1504/IJGUC.2019.102018>
- [21] H. Chouhayebi, J. Riffi, M. A. Mahraz, A. Yahyaouy, H. Tairi, and N. Alioua, "Facial expression recognition based on geometric features," in *2020 International Conference on Intelligent Systems and Computer Vision (ISCV)*, 2020-06, pp. 1–6.
- [22] G. Sharma, L. Singh, and S. Gautam, "Automatic facial expression recognition using combined geometric features," *3D Res*, vol. 10, no. 2, p. 14, 2019-04-01. [Online]. Available: <https://doi.org/10.1007/s13319-019-0224-0>
- [23] D. A. Ibrahim, D. A. Zebari, F. Y. H. Ahmed, and D. Q. Zeebaree, "Facial expression recognition using aggregated handcrafted descriptors based appearance method," in *2021 IEEE 11th International Conference on System Engineering and Technology (ICSET)*, 2021-11, pp. 177–182, ISSN: 2470-640X.
- [24] H. Kaya, F. Gürpınar, S. Afshar, and A. A. Salah, "Contrasting and combining least squares based learners for emotion recognition in the wild," in *Proceedings of the 2015 ACM on International Conference on Multimodal Interaction*. ACM, 2015-11-09, pp. 459–466. [Online]. Available: <https://dl.acm.org/doi/10.1145/2818346.2830588>
- [25] D. Liu, X. Ouyang, S. Xu, P. Zhou, K. He, and S. Wen, "SAANet: Siamese action-units attention network for improving dynamic facial expression recognition," *Neurocomputing*, vol. 413, pp. 145–157, 2020-11-06. [Online]. Available: <https://www.sciencedirect.com/science/article/pii/S092523122031050X>
- [26] X. Pan, G. Ying, G. Chen, H. Li, and W. Li, "A deep spatial and temporal aggregation framework for video-based facial expression recognition," *IEEE Access*, vol. 7, pp. 48 807–48 815, 2019. [Online]. Available: <https://ieeexplore.ieee.org/document/8674456/>
- [27] M. Z. Uddin, W. Khaksar, and J. Torresen, "Facial expression recognition using salient features and convolutional neural network," *IEEE Access*, vol. 5, pp. 26 146–26 161, 2017. [Online]. Available: <http://ieeexplore.ieee.org/document/8119492/>
- [28] S. Minaee, M. Minaei, and A. Abdolrashidi, "Deep-emotion: Facial expression recognition using attentional convolutional network," *Sensors*, vol. 21, no. 9, p. 3046, 2021-04-27. [Online]. Available: <https://www.mdpi.com/1424-8220/21/9/3046>
- [29] M. G. Calvo and D. Lundqvist, "Facial expressions of emotion (KDEF): Identification under different display-duration conditions," *Behav Res*, vol. 40, no. 1, pp. 109–115, 2008-02-01. [Online]. Available: <https://doi.org/10.3758/BRM.40.1.109>
- [30] P. Lucey, J. F. Cohn, T. Kanade, J. Saragih, Z. Ambadar, and I. Matthews, "The extended cohn-kanade dataset (CK+): A complete dataset for action unit and emotion-specified expression," in *2010 IEEE Computer Society Conference on Computer Vision and Pattern Recognition - Workshops*. IEEE, 2010-06, pp. 94–101. [Online]. Available: <http://ieeexplore.ieee.org/document/5543262/>
- [31] A. Paszke, S. Gross, F. Massa, A. Lerer, J. Bradbury, G. Chanan, T. Killeen, Z. Lin, N. Gimelshein, L. Antiga, A. Desmaison, A. Köpf, E. Yang, Z. DeVito, M. Raison, A. Tejani, S. Chilamkurthy, B. Steiner, L. Fang, J. Bai, and S. Chintala, "PyTorch: An imperative style, high-performance deep learning library," 2019-12-03. [Online]. Available: <http://arxiv.org/abs/1912.01703>
- [32] L. Wang, Z. He, B. Meng, K. Liu, Q. Dou, and X. Yang, "Two-pathway attention network for real-time facial expression recognition," *Journal of Real-Time Image Processing*, vol. 18, no. 4, pp. 1173–1182, 2021.
- [33] S. Subudhiray, H. K. Palo, and N. Das, "Effective recognition of facial emotions using dual transfer learned feature vectors and support vector machine," *International Journal of Information Technology*, vol. 15, no. 1, pp. 301–313, 2023.
- [34] J. X. Yu, K. M. Lim, and C. P. Lee, "Move-cnns: Model averaging ensemble of convolutional neural networks for facial expression recognition." *IAENG International Journal of Computer Science*, vol. 48, no. 3, 2021.
- [35] Q. Hu, C. Wu, J. Chi, X. Yu, and H. Wang, "Multi-level feature fusion facial expression recognition network," in *2020 Chinese Control And Decision Conference (CCDC)*. IEEE, 2020, pp. 5267–5272.
- [36] K. Mohan, A. Seal, O. Krejcar, and A. Yazidi, "Fer-net: facial expression recognition using deep neural net," *Neural Computing and Applications*, vol. 33, no. 15, pp. 9125–9136, 2021.
- [37] N. Kumar HN, A. S. Kumar, G. Prasad MS, and M. A. Shah, "Automatic facial expression recognition combining texture and shape features from

prominent facial regions,” *IET Image Processing*, vol. 17, no. 4, pp. 1111–1125, 2023.

- [38] M. Kas, Y. Ruichek, R. Messoussi *et al.*, “New framework for person-independent facial expression recognition combining textural and shape analysis through new feature extraction approach,” *Information Sciences*, vol. 549, pp. 200–220, 2021.
- [39] S. Eng, H. Ali, A. Cheah, and Y. Chong, “Facial expression recognition in jaffe and kdef datasets using histogram of oriented gradients and support vector machine,” in *IOP Conference series: materials science and engineering*, vol. 705, no. 1. IOP Publishing, 2019, p. 012031.
- [40] R. V. Puthanidam and T.-S. Moh, “A hybrid approach for facial expression recognition,” in *Proceedings of the 12th International Conference on Ubiquitous Information Management and Communication*, 2018, pp. 1–8.
- [41] A. J. Obaid and H. K. Alrammahi, “An intelligent facial expression recognition system using a hybrid deep convolutional neural network for multimedia applications,” *Applied Sciences*, vol. 13, no. 21, p. 12049, 2023.
- [42] Y. Yaddaden, M. Adda, and A. Bouzouane, “Facial expression recognition using locally linear embedding with lbp and hog descriptors,” in *2020 2nd International Workshop on Human-Centric Smart Environments for Health and Well-being (IHSH)*. IEEE, 2021, pp. 221–226.
- [43] S. Barra, S. Hossain, C. Pero, and S. Umer, “A facial expression recognition approach for social iot frameworks,” *Big Data Research*, vol. 30, p. 100353, 2022.
- [44] M. D. Zeiler and R. Fergus, “Visualizing and understanding convolutional networks,” in *Computer Vision—ECCV 2014: 13th European Conference, Zurich, Switzerland, September 6–12, 2014, Proceedings, Part 1 13*. Springer, 2014, pp. 818–833.



Abdülkadir Albayrak completed his bachelor’s, master’s, and doctoral studies in the field of computer engineering and developed algorithms based on traditional and deep learning methods for the classification of biomedical images and the detection of cellular structures (cancerous or normal cells) within these images for his theses. He has published many research articles in SCI-indexed journals, and has presented papers at various conferences. He achieved 2nd place worldwide in the competition titled “mitosis detection in histopathological images” organized by ICPR (International Conference Pattern Recognition). He is currently postdoctoral research fellow at the Department of Laboratory Medicine and Pathology.



Muhammed Cihad Arslanoğlu graduated from the Department of Electrical and Electronics Engineering at Dicle University for his undergraduate studies and is currently continuing his graduate studies in the same department. He has been involved in programming since high school and during his undergraduate studies, he developed numerous applications in image processing, artificial intelligence, and web technologies. Additionally, he works full-time as an Artificial Intelligence and Computer Vision specialist at Dicle Electricity Distribution Company.”



Hüseyin Acar received the B.S. degree in Electronics Engineering from Uludağ University, Bursa, Turkey, in 2006 and M.S. degree in Electrical-Electronics Engineering from Dicle University, Diyarbakır, Turkey, in 2010. He received the Ph.D. degree in Electrical-Electronics Engineering from Dicle University, Diyarbakır, Turkey, in 2020. He is currently an assistant professor at Dicle University Electrical-Electronics Engineering. His research interest includes machine learning, image processing, remote sensing, and embedded systems.

Hardware Implementation of Fully Controlled Bridge Rectifier with Rapid Control Prototyping Approach

Nezihe Yildiran


Abstract— In industrial applications, rapid prototyping of digital controls is important in terms of time, cost, and easier design steps. Especially the complexity of different power electronic converter circuits and their necessity of providing various operating conditions make digital control inevitable. However, developing a digital control system has many unknown details. In-the-loop simulation techniques evolved to simplify this stage during the last few decades. In this paper, a fully controlled bridge rectifier is designed and implemented by using a rapid control prototyping approach; its steps are accelerated with processor-in-the-loop and hardware-in-the-loop tests. Launchpad F28379D from Texas Instruments is used as an interface between the designed rectifier hardware circuit and MATLAB/Simulink Embedded Coder platform. Additionally, a driver control board is developed to provide switching signals and analog to digital measurements. The performance of the system is experimentally tested on a developed 500W rectifier prototype with a closed loop PI controller for voltage regulation at different parametric variations, such as step response, dynamic response, different load types. Step response rise time is 25ms, while the system continues stable operation under load change from 60% to 90% in 35ms.

Index Terms— Bridge Rectifier, In-the-loop simulation, Power Electronics, Rapid Prototyping.

I. INTRODUCTION

THE NEED for embedded systems is increasing and daily diversifying in the market. Each complex system includes several embedded systems used for various purposes such as power electronic converters, monitoring systems, battery management systems, and alert systems. Rectifiers, one of the common embedded systems, are employed in low, medium, and high-power applications with a wide range of voltage and current ratings. Although switch mode power supplies are being started to use attaining regulated DC output, there is still a need for efficient and high-performance rectifiers. Rectifiers with various types of configurations operate to convert AC source to

Nezihe Yildiran, is with Department of Energy Systems Engineering, Bahcesehir University, Istanbul, 34349, Turkey, (e-mail: nezihe.kucukyildiran@bau.edu.tr).

 <https://orcid.org/0000-0002-5902-1397>

Manuscript received April 6, 2024; accepted July 25, 2024.
DOI: [10.17694/bajece.1466201](https://doi.org/10.17694/bajece.1466201)

DC output in [1-3]. One of the common rectifier topologies is known as conventional rectifiers or line commutated rectifiers with low switching frequency in [4]. Conventional rectifiers, which are protecting their prevalence in the industry, are used in a wide variety of applications such as uninterruptible power supplies, synchronous motor field current control, the control of low power DC motors, and battery charging. These converters assure high reliability, simplicity, and fewer switching devices in [5-7]. The average load changes in a closed loop control in [1-4]. The embedded systems must react very fast against any disturbance and guarantee stability for different operating conditions.

Regarding this, physical device implementation is expensive and not feasible without simulation studies. Various simulation techniques are improved with different configurations and can be classified into two groups: offline simulation platforms and real time simulation. In the context of real time simulation, the transition between the simulation and physical hardware has been simplified with in-the-loop simulation techniques. Classification of techniques are Model-in-the-Loop (MIL), Software-in-the-Loop (SIL), Processor-in-the-Loop (PIL), and Hardware-in-the-Loop (HIL) in [8-10]. The plant model and controller logic are simulated in a simulation program without hardware in MIL. SIL describes the simulation of a plant model with a digital controller model, while PIL is a test approach to design the controller running in an external digital platform. HIL is a technique to test the plant or controller running in a real time simulator, interacting with a real plant or controller, so HIL became an inevitable point for the initialization of microprocessors. Furthermore, HIL is a way to bridge the gap between simulation and real systems to test real operational conditions. Also, it supports the flexible testing platform for the first implementation. During the design, testing, and assembling of digital controls for power systems and power electronics, real time simulation, especially HIL testing is accepted as an effective approach in terms of cost, time, and reliability. The difficulty in the product design of the embedded systems can be diminished by using HIL implementation.

The design approach of controllers has significantly changed over the years. As a result, the reliability of designs is enhanced, and the design cycle is shortened in [11]. Many instances of in-the-loop simulation techniques have been examined in the literature with different aspects. A test platform for T-type converter is implemented in real time simulator from OPAL-

RT in [12]. In [13], the examination and simulation of the buck converter by using discrete time mathematical model in HIL with FPGA are presented. A power hardware-in-the-loop (PHIL) testbed for grid-connected electric vehicle (EV) charger including modelling details is implemented in [14]. A boost converter and an H-bridge inverter with their state feedback control system have been evaluated using Real Time Virtual Test Bed in [15]. The classification of important real time tools for in-the-loop testing with respect to cost, sampling rate capability, software needs, and usability is mentioned with specific examples in [16]. Similarly, the history of real-time simulators is summarized, and important features are comprehensively reported in [17]. The architecture for real-time control is introduced elaborately and a controller is designed for PIL testing of three bi-directional DC-DC converters in electric vehicles to obtain a convenient power balance in [18]. Similarly, buck converter prototype is examined based on HIL simulation [19]. Besides the applications of power electronic converter management and controller design in the literature, in-the-loop testing methods are also significant for smart grid and microgrid studies due to their complexity in [20, 21]. HIL simulation is used to test low voltage grid-integrated multilevel converter stability [22]. A grid-connected wind energy system is analyzed with HIL testing using optimized design parameters [23].

Real-time microcontroller expansion boards of different companies are utilized to implement the control platform during in-the-loop tests. Among the widespread alternatives, dSpace controllers, field programmable gate array (FPGA), and Texas Instruments C2000 series microcontrollers are well known examples. Several studies have presented the design and implementation of a control platform with in-the-loop tests using dSpace hardware in [8, 16], FPGA in [13, 15, 24, 25], and C2000 microcontrollers in [12, 18, 26, 27]. Microcontrollers can be programmed through MATLAB Simulink Embedded Coder in addition to attaining gate pulses with feedback control in [26]. As a recent application, HIL and experimental study are presented to control three phase voltage source inverters using C2000, PLECS, and RT-Box systems [28].

This paper attempts to present the contribution of in-the-loop techniques during the digital controller design by examining a single-phase full wave thyristor-controlled line commutated rectifier. The study is improved one more step and tested on real hardware. Discrete tests are also evaluated for the designed rectifier. The contributions of this paper are to design a driver control board to expand the capabilities of the launchpad and to validate the design by testing a 500W rated rectifier. The driver control board consists of circuits for measurements, gate triggering, and zero cross detection. Operational amplifiers are integrated for voltage measurements.

The rest of the paper is organized as follows. The comprehensive system architecture and its key elements are explained in Section 2. Section 3 describes the test platform configuration details. Then, Section 4 presents the experimental performance of single-phase full bridge rectifier implementation. Section 5 concludes the paper.

II. SYSTEM ARCHITECTURE

The system overall block diagram is given in Figure 1. A step-down transformer is integrated at the input side of the system to be able to adjust the output voltage of the rectifier circuit within the determined values. A fully controlled bridge rectifier is used for experimental validation so that the load current is continuous and ripple free. The fully controlled bridge converter consists of four thyristors of TH1, TH2, TH3, and TH4 are turned on by their gate signal and naturally turns off when a reverse voltage appears across it. In this case, the average output voltage can be determined by the following equation.

$$V_{out}^{avg} = \frac{1}{\pi} \int_{\alpha}^{\pi} V_{max} \sin(\omega t) d\omega t = \frac{2V_{max}}{\pi} \cos\alpha \quad (1)$$

Capacitors are added to the output of the rectifier circuit as a filter to mitigate the output voltage ripple. A power supply board with multiple levels of voltage is utilized to supply integrated circuits on the control board, the zero-cross circuit, and the trigger circuit. The control board is designed to attain proper integration between the subcircuits of the boards. The zero cross circuit detects the points when the voltage crosses zero in either direction. The detection of the zero cross points is important to trigger the switching devices at the right time during continuous operation. The trigger circuit comprises four separate gate drive circuits for thyristors including gate pulse transformers, transistors, resistors, capacitors, and diodes. The trigger circuit converts the created PWM signals of the control board into a proper pulse signal train that can trigger the thyristors. The presented system includes an F28379D launchpad with dual core 32-bit floating-point microcontroller. The microprocessor board incorporates high-speed serial channels and uses Universal Serial Bus (USB) as an interface that is useful for interprocessor communications.

III. TEST PLATFORM CONFIGURATION

The launchpad or similar rapid prototyping systems use the same microprocessor family products as their industrial counterparts, so a prototype can be successfully developed and prepared. Furthermore, the developed software can be also integrated simply with the actual system. Coding in the program of code composer studio (CCS) generally used is harder to design and needs more time; therefore, embedded coder enables faster controller design than hand-write code. Whereas C-code at the quality of hand-written source code can be generated with less effort and at the level of an excellent programmer. Automatic generation of software code can be attained via MATLAB/Simulink Embedded Coder feature in a more practicable way.

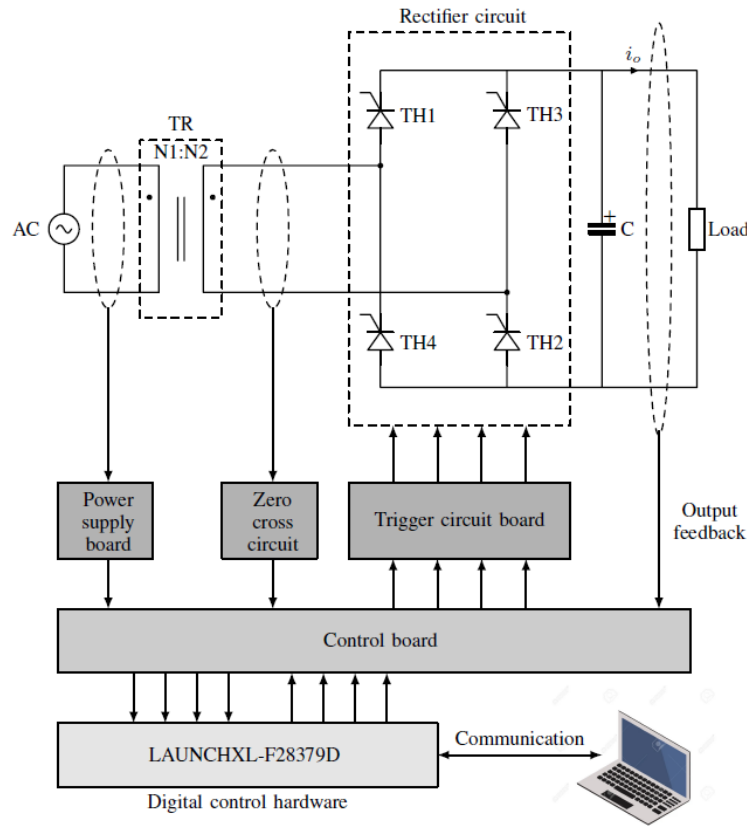


Fig. 1. System overall block diagram.

A simulation model of the controller with digital to analog signals (feedback) is created in Matlab/Simulink and then “Generator of production code (Hardware) Embedded Coder Support Package for TI 2000” is used for generating C-code and real time test with parameter tuning feature. The application of embedded coder includes initialization of target, I/O settings for target, the configurations of analog to digital converter (ADC), enhanced pulse width modulator (ePWM), and general-purpose input/output (GPIO) blocks, etc. Thanks to this method, minimum integration time and cost can be achievable in serial production. The graphical programming language of MATLAB helps to obtain simpler development even for complex systems. The time for programming and control design is reduced because the code is generated automatically. The following subsections deal with the peripheral requirements for the microprocessor.

A. ADC Configuration

Four independent ADC modules with the resolutions of 16-bit differential or 12-bit single-ended can be configured to sample analog pins and convert them to digital data. The value of output voltage and current feedback, detection of zero crosses, and the determination of phase quantities are determined by configured ADC pins. The output data type is selected as uint16 and the gain, offset, linearity of the data, and the conversion of the data to the measured units are set by using ADC calibration routines and limited between the saturation

ranges. The scheme of the ADC configuration is shown in Figure 2.

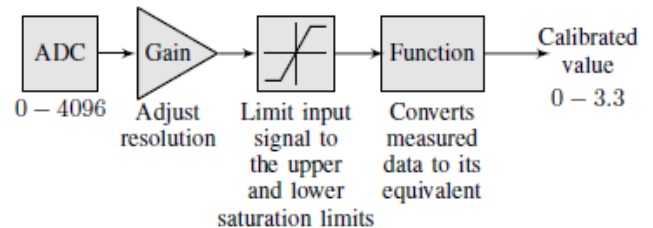


Fig. 2. The scheme of the ADC configuration.

B. ePWM Configuration

Pulse width modulation (PWM) is a prevalent technique that produces variable width pulses to adjust the amplitude of the feedback signal. The F28379D microprocessor has 16 ePWM modules with two outputs, being able to generate PWM waveforms with various adjustable functionalities. Three modules are configured with up-down count mode and dual edge symmetric waveform properties in the proposed system. Module output frequency is computed according to the following equation.

$$f_{PWM} = \frac{ePWM \text{ clock frequency}}{2 \times TBCLK \text{ prescaler} \times \text{timer period}} \quad (2)$$

Where TBCLK is the time base clock. ePWM clock frequency is defined as 100MHz for each module. The first module is activated with an on/off switch which is connected to GPIO122 as the trip zone source, and it is used to control the gate signals compatible with zero cross signal. *TBCLK prescaler divider* is 16 and the timer period is 62,500 for the module to attain a 50Hz signal, the grid frequency. The counter compare parameters of the block are specified to adjust pulse widths according to output voltage feedback. The remaining two modules are used to trigger the thyristors in pairs. In that case, the *TBCLK prescaler divider* is 1 and the timer period is 50,000 for the frequency of 1kHz signals, the switching frequency.

C. GPIO Configuration

The GPIO peripheral configures the general-purpose input/output pins to control and detect the interaction with other components. The state of the input can be detected by reading the state of an internal register when configured as an input. Otherwise, it can be written to an internal register to control the state driven on the output pin when configured as an output. On-off control of the system and the protections are connected via GPIOs in the presented system.

D. Controller Design

The system must manage constant output voltage, current, and reliable operation in terms of sudden load variations

according to requirements. Therefore, a control system must be integrated to satisfy the expected goals despite different operating conditions and disturbances. Throughout the controller development process, the model can move through MIL, SIL, PIL, and HIL testing stages.

In real run-time, the model is divided into two separate parts, the plant model and the controller for the *HIL* stage. The plant model is removed and generated code on the target is attached to the physical hardware during prototyping tests. At the *HIL* stage, physical hardware is connected to the Simulink environment in external mode to operate simultaneously, collect data in each step of the simulation, and tune the controller parameters. Then, the system can be analyzed and tested when whole parts are set up as hardware.

A proportional-integral (PI) controller is implemented to achieve robust output voltage despite parametric variations due to its easy implementation and fast response. The control is carried out by changing the firing angle of thyristors. The control structure is given in Figure 3. PI controller block is used after the comparison of measured output value with reference. The output of the controller block is used in the angle calculation function with the reference of measured input voltage determined zero crosses. The output of the function is proper to activate the thyristor trigger circuit. The plant transfer function is implemented in in-the-loop simulation stages before the prototype. The values of output voltage and output current are measured with the routine of ADC configuration.

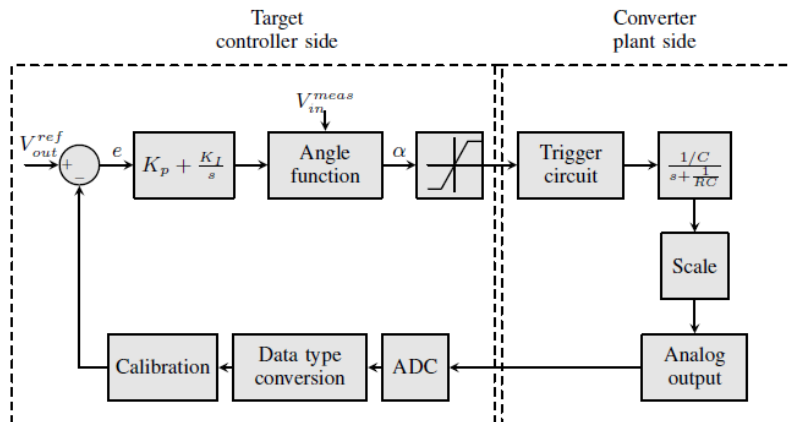


Fig. 3. Control structure.

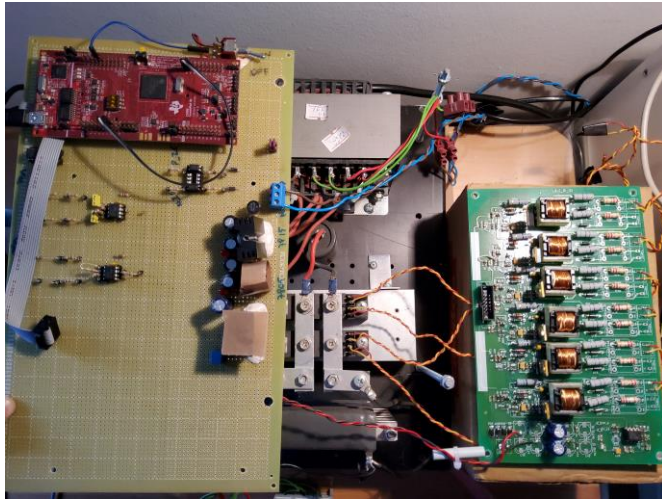
The same controller is tested in the system and directly implemented as final hardware, so the development time of the converter is improved. The interface algorithm determines how the signals are exchanged between simulation platform and physical system. The PIL and HIL simulations eliminated several iterations of pre-prototype hardware.

IV. EXPERIMENTAL RESULTS

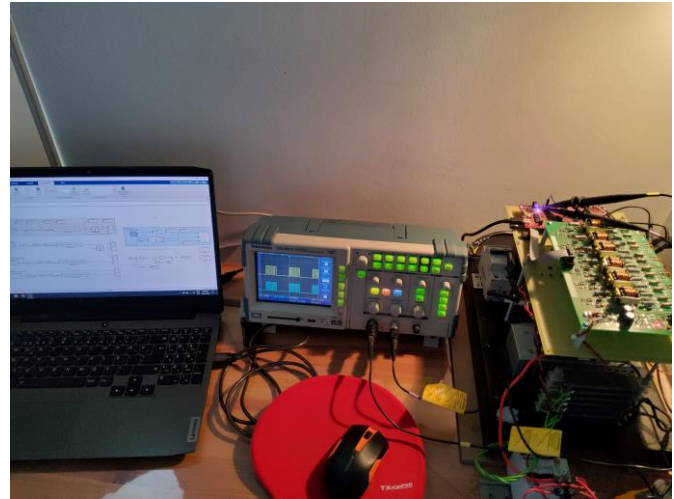
The validation of the proposed system is tested with a 500W power rated rectifier prototype with its peripheral circuits at various load levels. The experimental setup is given in Figure 4a and Figure 4b. Additionally, the specifications of the prototype are presented in Table I.

TABLE I
SYSTEM SPECIFICATIONS

Parameters	Values
Rated input voltage	220V _{ac}
Input voltage frequency	50Hz
Rated output voltage	48V _{dc}
Output power	500W
Input transformer ratings	220V/60V 1kW 50Hz
Output filter capacitance	2 x 470uF 100V _{dc}
Thyristor modules	MCC44-12io1B
Switching frequency	1kHz



(a) Designed electronic cards and components detailed view.



(b) Overall system.

Fig. 4. Experimental setup.

The system rated voltage is $220V_{ac}$ with $\pm 10\%$ range, while the output rated voltage is adjusted to $48V_{dc}$. Figure 4a shows the designed electronic cards of the power supply board, control board, trigger circuit board, and launchpad besides the thyristor block and input transformer on the heat sink. Figure 4a presents the proposed system with whole components of complete experimental system, laptop communication, and oscilloscope connection. The setup is tested with a load of six parallel connected 25Ω resistance groups.

switching case. Figure 7 shows channel A of EPWM1 and channel A of EPWM3 triggered by channel B of EPWM1 during full cycle switching operation. Channel B of EPWM2 and EPWM3 are the same as channel A to trigger thyristor pairs. The channel A outputs of EPWM2 and EPWM3 in closed loop operation with 50% load is given in Figure 8.

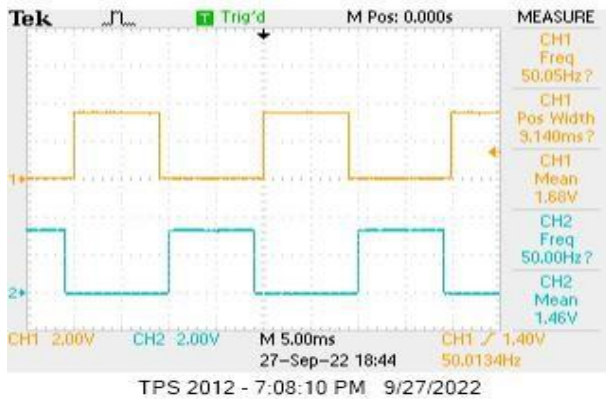


Fig. 5. EPWM1 block outputs in open loop operation.

Three of the existing sixteen pulse width modulation modules of the launchpad were configured to trigger four thyristors according to zero cross references in the proposed system. The first module was configured with respect to zero cross signal, while the others were configured by using the first module signal as a trip zone source for thyristors switching. EPWM1 outputs given in Figure 5 show the 50Hz frequency PWM outputs that are synchronized with zero crosses, and the signals are attained in the open loop operation with the full cycle switching process. Figure 6 shows channel A of EPWM1 and channel A of EPWM2 triggered by channel A of EPWM1 for zero cross and switching signal adaptation during full cycle

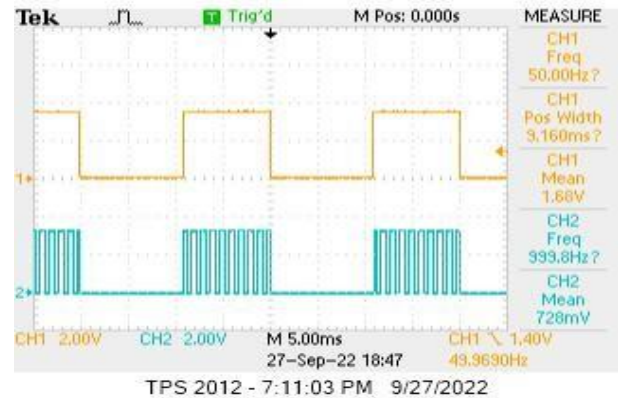


Fig. 6. Channel A outputs of EPWM1 and EPWM2 in open loop operation.

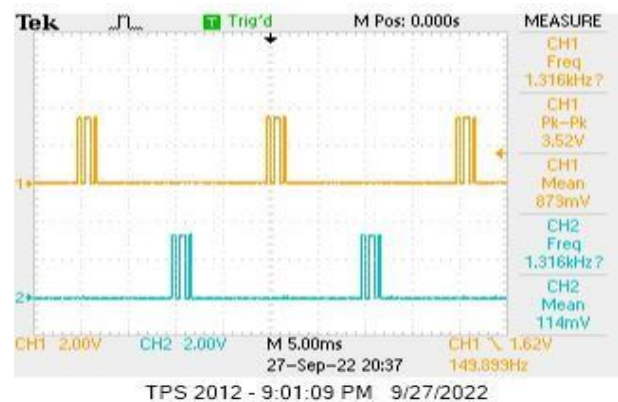


Fig. 7. Channel A outputs of EPWM1 and EPWM3 in open loop operation.

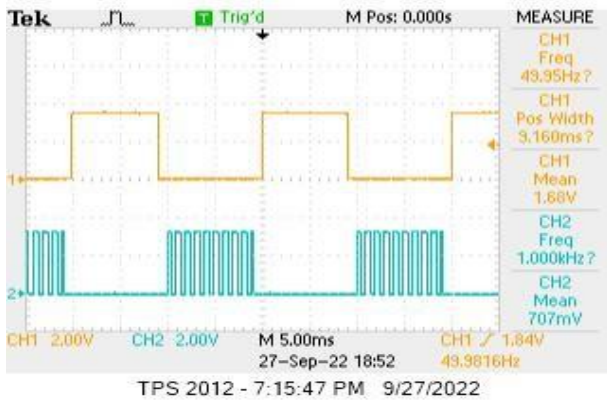


Fig. 8. Channel A outputs of EPWM2 and EPWM3 in closed loop operation with 50% load.

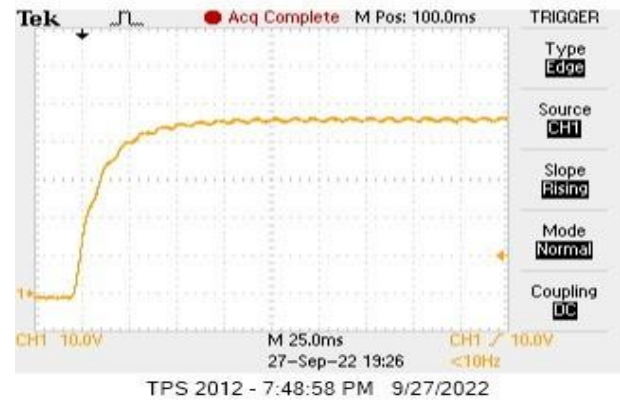


Fig. 10. Step response of the closed-loop control.

The operation of experimental setup is improved with additional features for reliable operation. Therefore, one of the general-purpose input/output pins, GPIO122 is configured as an input to turn on/off the rectifier circuit by controlling the PWM signals manually with a switch or remotely with software codes. When on command has activated, the PWM signals are initialized within 20ms. The initialization of the PWM channels with ON signal is shown in Figure 9. In addition, some protections such as over temperature and output short circuits are reserved with a similar method.

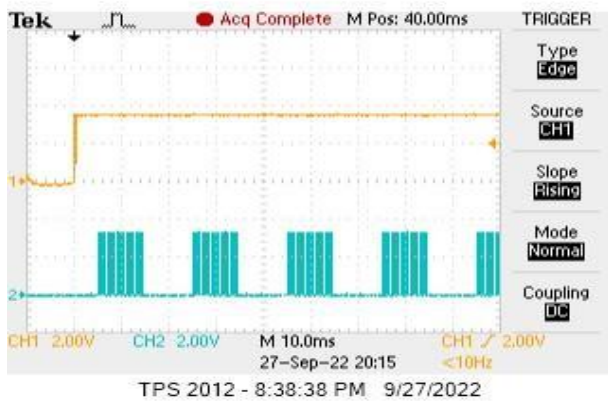


Fig. 9. PWM initialization with on command.

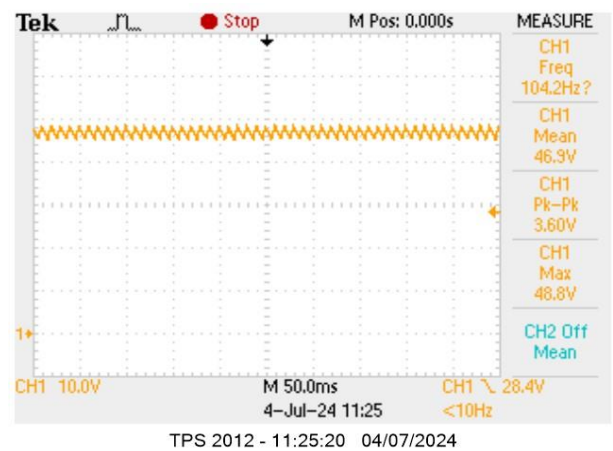


Fig. 11. The output voltage waveform with RL load at full load.

The dynamic response of the designed rectifier is also investigated for further analysis. Figure 12 shows the dynamic response of the designed converter when output load changes from 60% to 90% load level. The output voltage remains constant against output load increment. The ripple voltage value is 2.6V.

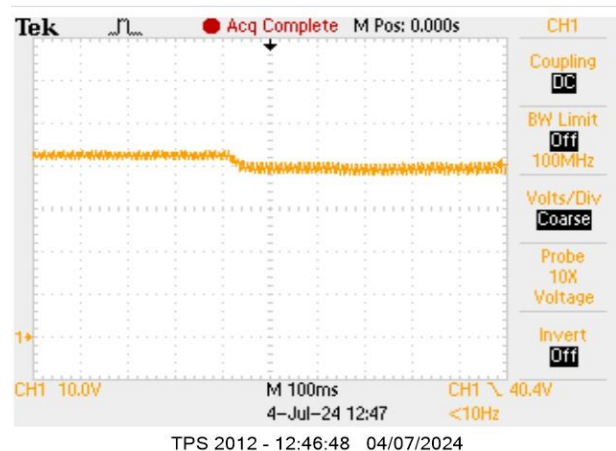


Fig. 12. Output voltage under dynamic changes from 60% to 90% load increase.

Figure 10 shows the step response of the closed loop control at 10% load level when the controller gains K_p and K_i are tuned as 3 and 300, respectively. The controller parameters are determined with the help of PIL and HIL simulations and the gains that show the best performance in the step response and load regulation is defined as the prototype controller gains. The settling time of the system is around 25ms and there is no oscillation in the step response performance.

The system is tested and evaluated with inductive load at maximum load level. The load has a resistance of 12.5Ω and the inductance of $160\mu\text{H}$. The output voltage waveform with RL load is given in Figure 11.

V. CONCLUSION

The difficulties in the design process steps, the lack of time, the risk of damage, and cost concerns cause the new developments through the way to real hardware. The approach of developing digital controls for power electronics has been described in this paper. The proposed test platform for rapid prototyping of a single-phase conventional rectifier is examined. Finally, the validated test results were employed to analyze the performance of a conventional rectifier. The experimental results were presented to confirm the system and controller performance. The performance of the system was experimentally tested on a developed 500W rectifier prototype with a closed loop PI controller. The step response of the output voltage was examined, and the rise time of the response was obtained as 25ms. The prototype was tested with resistive and inductive load. Both load types presented stable operation. Finally, the dynamic performance was investigated under load change from 60% to 90%.

This paper presents an open road map for academic studies and industry. The system can be used in lectures to explain the principles of power electronic converters, and it could be possible to teach the learning outcomes also as online because the importance of online supported studies arose during the pandemic period.

REFERENCES

- [1] M. H. Rashid, "Power Electronics Circuits, Devices and Applications." New Delphi, India: Prentice Hall, 2004.
- [2] P. Bimbhra, "Power Electronics." New Delphi, India: Khanna Publishers, 2012.
- [3] G. Mithal and D. M. Gupta, "Industrial and Power Electronics." New Delphi, India: Khanna Publishers, 2006.
- [4] J. Rodríguez, P. Lezana, S. Kouro, and A. Weinstein, "11 - single-phase controlled rectifiers," in Software engineering—from auxiliary to key technologies, M. H. Rashid, Ed. Boston: Butterworth-Heinemann, 2011, pp. 183–204.
- [5] M. S. Hamad, M. I. Masoud, and B. W. Williams, "Medium-voltage 12-pulse converter: Output voltage harmonic compensation using a series apf," IEEE Transactions on Industrial Electronics, vol. 61, no. 1, pp. 43–52, 2014.
- [6] H. Akagi, "Large static converters for industry and utility applications," Proceedings of the IEEE, vol. 89, no. 6, pp. 976–983, 2001.
- [7] B. K. Bose, "Power Electronics and AC Drives." NJ, USA: Prentice Hall, 1986.
- [8] A. Monti, E. Santi, R. Dougal, and M. Riva, "Rapid prototyping of digital controls for power electronics," IEEE Transactions on Power Electronics, vol. 18, no. 3, pp. 915–923, 2003.
- [9] J. Nibert, M. E. Herniter, and Z. Chambers, "Model-based system design for mil, sil, and hil," World Electric Vehicle Journal, vol. 5, no. 4, pp. 1121–1130, 2012.
- [10] C. Buccella, C. Cecati, and H. Latafat, "Digital control of power converters—a survey," IEEE Transactions on Industrial Informatics, vol. 8, no. 3, pp. 437–447, 2012.
- [11] L. Mikova, M. Kelemen, I. Virgala, and T. Liptak, "Model based design of embedded systems," Journal of Automation and Control, vol. 5, no. 2, pp. 64–68, 2017.
- [12] J. Martins, S. Spataru, T. Kerekes, D. Sera, P. Douglass, G. Yang, and K. Moth, "Test platform for rapid prototyping of digital control for power electronic converters," in IECON 2019 - 45th Annual Conference of the IEEE Industrial Electronics Society, vol. 1, 2019, pp. 2056–2061.
- [13] J. Mina, Z. Flores, E. Lopez, A. Perez, and J.-H. Calleja, "Processor-in-the-loop and hardware-in-the-loop simulation of electric systems based in fpga," in 2016 13th International Conference on Power Electronics (CIEP), 2016, pp. 172–177.

- [14] I. Jayawardana, C. N. M. Ho, and Y. Zhang, "A comprehensive study and validation of a power-hil testbed for evaluating grid-connected ev chargers," IEEE Journal of Emerging and Selected Topics in Power Electronics, vol. 10, no. 2, pp. 2395–2410, 2022.
- [15] B. Lu, X. Wu, H. Figueroa, and A. Monti, "A low-cost real-time hardware-in-the-loop testing approach of power electronics controls," IEEE Transactions on Industrial Electronics, vol. 54, no. 2, pp. 919–931, 2007.
- [16] R. Grepl, "Real-time control prototyping in matlab/simulink: Review of tools for research and education in mechatronics," in 2011 IEEE International Conference on Mechatronics, 2011, pp. 881–886.
- [17] M. D. Omar Faruque, T. Strasser, G. Lauss, V. Jalili-Marandi, P. Forsyth, C. Dufour, V. Dinavahi, A. Monti, P. Kotsampopoulos, J. A. Martinez, K. Strunz, M. Saeedifard, X. Wang, D. Shearer, and M. Paolone, "Real-time simulation technologies for power systems design, testing, and analysis," IEEE Power and Energy Technology Systems Journal, vol. 2, no. 2, pp. 63–73, 2015.
- [18] B. dos Santos, R. E. Araujo, D. Varaj' ao, and C. Pinto, "Rapid prototyping framework for real-time control of power electronic converters using simulink," in IECON 2013 - 39th Annual Conference of the IEEE Industrial Electronics Society, 2013, pp. 2303–2308.
- [19] A. S. Vijay, S. Doolla, and M. C. Chandorkar, "Real-time testing approaches for microgrids," IEEE Journal of Emerging and Selected Topics in Power Electronics, vol. 5, no. 3, pp. 1356–1376, 2017.
- [20] S. Buso and T. Caldognetto, "Rapid prototyping of digital controllers for microgrid inverters," IEEE Journal of Emerging and Selected Topics in Power Electronics, vol. 3, no. 2, pp. 440–450, 2015.
- [21] J. Lim, K. Heo, C. Jeon, H. Kim, and J. Jung, "Development of power hardware-in-the-loop simulation testbed to verify lvdc grid stability using offline damping impedance design," Journal of Electrical Engineering and Technology, vol. 19, pp. 3297–3308, 2024.
- [22] T. Taluo, L. Ristic, M. Agha-Kashkooli, and M. Jovanovic, "Hardware-in-the-loop testing of brushless doubly fed reluctance generator under unbalanced grid voltage conditions," International Journal of Electrical Power and Energy Systems, vol. 158, pp. 1–11, 2024.
- [23] H. Bai, G. Huang, C. Liu, Y. Huangfu, and F. Gao, "A controller hil testing approach of high switching frequency power converter via slower-than-real-time simulation," IEEE Transactions on Industrial Electronics, vol. 71, no. 8, pp. 8690–8702, 2024.
- [24] Y. Luo, M. A. Awal, W. Yu, and I. Husain, "Fpga implementation for rapid prototyping of high-performance voltage source inverters," CPSS Transactions on Power Electronics and Applications, vol. 6, no. 4, pp. 320–331, 2021.
- [25] J. Badar, F. Akhter, H. M. Munir, S. S. H. Bukhari, and J.-S. Ro, "Efficient real-time controller design test bench for power converter applications," IEEE Access, vol. 9, pp. 118880–118892, 2021.
- [26] A. Elrajoubi, S. S. Ang, and A. Abushaiba, "Tms320f28335 dsp programming using matlab simulink embedded coder: Techniques and advancements," in 2017 IEEE 18th Workshop on Control and Modeling for Power Electronics (COMPEL), 2017, pp. 1–7.
- [27] J. Aravena, D. Carrasco, M. Diaz, M. Uriarte, F. Rojas, R. Cardenas, and J. C. Travieso, "Design and implementation of a low-cost real-time control platform for power electronics applications," Energies, vol. 13, no. 6, 2020.
- [28] R. M. Milasi, "A nonlinear adaptive control for a bidirectional dc-ac converter with parameter uncertainties," IEEE Transactions on Industrial Electronics, vol. 71, no. 8, pp. 9551–9558, 2024.

BIOGRAPHY

Nezihe Yıldırım received the B.Sc. and M.Sc. degrees in electrical engineering in 2004 and 2007, respectively, from the Istanbul Technical University (ITU), Istanbul, Turkey. She received Ph.D. degree at Bahcesehir University, Istanbul, Turkey in 2018. She has experience in power electronics research and development from the different companies between 2004-2012. She is Assistant Prof. Dr. in Energy Systems Engineering Department at Bahcesehir University. Her current research interests include modeling and control of power electronic converters, modeling renewable energy sources, and power electronic applications of smart grid.

Multipath Characteristics of Orbital Angular Momentum Vortex Electromagnetic Radio Waves Over an Infinite Ground Plane

Ugur Yesilyurt

Abstract—In this paper, the effect of an infinitely sized ground plane on the orbital angular momentum (OAM) vortex electromagnetic (EM) radio waves is investigated. Although the effect of an infinite ground on OAM wave propagation and communication has already been numerically examined in the literature using the method of moments (MoM), this study analyzes this situation analytically and obtains the final form expressions derived theoretically. The multipath characteristics of OAM waves in a superconducting ground plane are theoretically presented considering both horizontal and vertical polarization conditions. In addition to direct radiation to an observation point in the far-field from the array antenna, many reflected radiations from the ground plane are also transmitted. The most fundamental reflected radiation is analyzed over a uniform circular array (UCA), adopting electromagnetic image theory. Furthermore, the transmitted field expressions obtained by considering both the circular array parallel to the ground plane and the circular array upright to the ground plane are formulated in a general analytical form for an OAM wave on a superconducting ground plane. In addition, numerical simulations are applied to exemplify the properties of OAM waves in the superconducting ground plane, unlike the isolated medium.

Index Terms—Antenna arrays, infinite ground plane, orbital angular momentum (OAM), multipath propagation.

I. INTRODUCTION

BESIDES linear momentum, an electromagnetic (EM) wave can carry two types of angular momentum related to rotational dynamics: spin angular momentum and orbital angular momentum. Unlike spin angular momentum (SAM), which describes the polarization state of electromagnetic radiation, orbital angular momentum (OAM) is concerned with spatial phase distribution. OAM, which has a special physical property in addition to conventional linear momentum and SAM, can offer new degrees of freedom [1], [2], [3], [4]. Thus, the vortex electromagnetic waves carrying OAM have been a rapidly growing area of research that has attracted great interest in many fields over the past few years. Different from frequency, time, phase, amplitude, and polarization, OAM, which is a new degree of freedom, has distinctive advantages such as secure transmission and information transmission speed and capacity [5], [6], [7], [8], [9], [10], [11].

An OAM vortex EM wave is usually an EM wave with a "doughnut"-like intensity shape where the electric field intensity is zero at the center. Compared to plane waves,

Ugur Yesilyurt is with the Department of Electrical and Electronic Engineering, Engineering and Architecture Faculty, Erzurum Technical University, Erzurum, 25050, Turkey e-mail: ugur.yesilyurt@erzurum.edu.tr

EM waves carrying OAM possess a spiral wave phase front structure. For this reason, EM waves carrying OAM are frequently referred to as spiral, vortex, helical, or twisting waves. Phase fronts with different OAM modes generate different spiral electromagnetic waves. The modes of OAM are mutually orthogonal to each other, and this orthogonality greatly increases the efficiency of spectrum utilization and degrees of freedom [12], [13], [14], [15], [16].

After the investigation in 1992 that helical phase-fronted light beams can carry the OAM, the vortex EM waves have been widely used in optics [12]. B. Thidé et al. demonstrated that OAM is not limited to electromagnetic waves at light frequencies, by introducing the operation of OAM beams to the radio frequency (RF) field for the first time in 2007 [17]. Thus the potential of using OAM for communication has found application in the range of radio frequencies lower than light. Many methods have been improved in the literature to produce OAM radio waves, including antenna arrays, spiral reflectors, spiral phase plates, and metasurface [18], [19], [20], [21], [22]. Furthermore, due to its high controllability and good beamforming ability, a uniform circular array (UCA) is extensively utilized in OAM beam production. In order to produce an OAM beam in a UCA, the same amplitude and appropriate phase-shifted feed network must be applied to each element. By using incrementally gradual phase generators between adjacent antennas at the UCA, beams with various OAM modes can be generated [23], [24], [25], [26]. In addition, OAM beams are formed using the concentric circular array (CCA) structure, which consists of more than one circular array with different radii and the same center [27], [28]. Unlike UCAs which need external phase shift networks for neighboring elements, it is possible to obtain OAM with helical circular subarray (HCSA) forms with helical phase alignments [29].

Usually, only the direct propagation is analyzed analytically, considering the propagation of the OAM wave in an isolated environment. In real life, unlike an isolated environment, vortex electromagnetic waves not only come from antenna elements directly to the observation point but also reflected waves from the ground plane. Thus, the effect of multipath propagation of vortex EM waves carrying OAM is an important issue to be investigated, and the effect of an infinite ground on OAM wave propagation and communication was studied using the method of moments (MoM) in [30]. In the literature, an analytical investigation of multipath propagation of linear arrays has been made [31], [32]. In this study, the

analytical investigation is made for the case where UCA is positioned on the ground plane to examine the effect of an infinite ground on OAM wave propagation. Therefore, interesting simulation results have been obtained by analytically examining the multipath propagation of vortex EM waves in the superconducting ground plane based on a theoretical basis. The multipath properties of OAM waves in a superconducting ground plane, both parallel and upright positioning of the UCA to the ground plane are theoretically evaluated. Contrary to an isolated environment as a result of the constructive and destructive effect of multiple propagations at the observation point, it slices the "donut"-like OAM pattern. Similarly, the vortex EM wave helical phase fronts are also segmented symmetrically with respect to the ground plane normal. In conclusion, this study has contributed to the literature through theoretical investigation and three-dimensional simulations considering the multipath effect of the OAM wave and the ground plane design of the UCA.

II. THE MULTIPATH RADIATION OF OAM WAVE OVER THE INFINITE GROUND PLANE

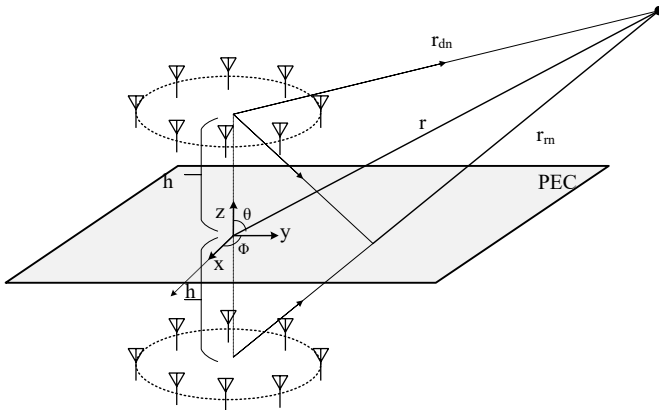


Fig. 1. UCA placed parallel at a given height (h) from an infinitely sized superconducting ground plane

The simple two-way propagation configuration of vortex EM waves carrying OAM is demonstrated in Figure 1. A circular array of N elements is parallel to the ground position along a circular ring of radius a . The UCA has h height from the superconducting ground plane placed in the x - y plane. To achieve the OAM wave, the UCA configuration is basically phased the array with a $2\pi l/N$ phase difference between the elements; where l represents the OAM mode number (topological charge). For the image theory analytical application, hypothetical array elements are constructed symmetrically according to the ground position (depth h below the ground plane) with the approach that the ground plane is infinitely sized superconducting ground. In addition to the direct path to the observation point, there are many reflected paths from the ground plane. The multipath property of the OAM wave, which comprises the direct and the most fundamental reflected path, is examined. The electric field of

the OAM wave propagating in the direct path under the far-field approach can be mathematically written as:

$$E_d = \sum_{n=0}^{N-1} I_n \xi_n(\theta_{dn}, \phi_{dn}) \frac{e^{j\omega_0(t - \frac{r_{dn}}{c})}}{r_{dn}} e^{jl\phi_n}, \quad (1)$$

where, I_n represents n^{th} element excitation amplitude, $\xi_n(\theta_{dn}, \phi_{dn})$ denotes the n^{th} element far-field pattern at the direct path, r_{dn} is the n^{th} array element direct path, and $\omega_0 = 2\pi f_0$ is the center operating frequency. $\phi_n = 2\pi n/N$ represents the n^{th} element excitation phase ($n = 0, 1, \dots, N-1$). In terms of the phase term, the r_{dn} delay term is denoted by

$$r_{dn} \cong r - \langle \hat{\mathbf{a}}_r, \mathbf{r}_n \rangle, \quad (2)$$

where, $\langle \cdot, \cdot \rangle$ denotes the inner product operator, $\hat{\mathbf{a}}_r = \sin\theta\cos\phi\hat{\mathbf{a}}_x + \sin\theta\sin\phi\hat{\mathbf{a}}_y + \cos\theta\hat{\mathbf{a}}_z$ represents the unit vector in the way of the observation point, and $\mathbf{r}_n = a\cos\phi_n\hat{\mathbf{a}}_x + a\sin\phi_n\hat{\mathbf{a}}_y + h\hat{\mathbf{a}}_z$ (where h is the height from the array center to the ground plane and a is the circle radius.) is the position vector for the n^{th} real element of the array. The r_{dn} delay term is denoted by:

$$r_{dn} \cong r - \langle \hat{\mathbf{a}}_r, (a\cos\phi_n\hat{\mathbf{a}}_x + a\sin\phi_n\hat{\mathbf{a}}_y + h\hat{\mathbf{a}}_z) \rangle \cong r - a\sin\theta\cos(\phi - \phi_n) - h\cos\theta. \quad (3)$$

By substituting Equation (3) into Equation (1), the electric field propagating in the direct path of the OAM wave becomes:

$$E_d = e^{j\frac{\omega_0}{c}(tc-r)} \sum_{n=0}^{N-1} I_n \xi_n(\theta_{dn}, \phi_{dn}) \frac{1}{r_{dn}} e^{j\frac{\omega_0}{c}[a\sin\theta\cos(\phi - \phi_n) + h\cos\theta]} e^{jl\phi_n}. \quad (4)$$

On the other hand, image theory is used to obtain the electric field expression of the most fundamental OAM wave reflected by the ground. The hypothetical array elements are constructed symmetrically according to the ground position (according to image theory), and this OAM wave propagating directly from the hypothetical array antenna to the observation point is equivalent to the most fundamental OAM wave reflected by the superconducting ground plane. In addition, in the horizontal and vertical polarization cases, the hypothetical array antenna polarization is the opposite and the same as the original polarization of the real array antenna, respectively. Therefore, the electric field of the most fundamental OAM wave reflected by the ground is given by:

$$E_r = \frac{h_p}{v_p} \sum_{n=0}^{N-1} I_n \xi_n(\theta_{rn}, \phi_{rn}) \frac{e^{j\omega_0(t - \frac{r_{rn}}{c})}}{r_{rn}} e^{jl\phi_n}, \quad (5)$$

where, v_p denotes vertical polarization, and h_p and denotes horizontal polarization. r_{rn} is the direct path to the observation point of UCA's n^{th} hypothetical source, and r_{rn} is also the path of the most fundamental OAM wave reflected from the ground plane. In terms of the phase term of the reflected OAM wave, the r_{rn} delay term is denoted by:

$$r_{rn} \cong r - \langle \hat{\mathbf{a}}_r, \mathbf{r}'_n \rangle, \quad (6)$$

where, $\mathbf{r}'_n = a \cos \phi_n \hat{\mathbf{a}}_x + a \sin \phi_n \hat{\mathbf{a}}_y - h \hat{\mathbf{a}}_z$ is the position vector for the n^{th} hypothetical element of UCA. The r_{rn} delay term is given by:

$$\begin{aligned} r_{rn} &\cong r - \langle \hat{\mathbf{a}}_r, (a \cos \phi_n \hat{\mathbf{a}}_x + a \sin \phi_n \hat{\mathbf{a}}_y - h \hat{\mathbf{a}}_z) \rangle \\ &\cong r - a \sin \theta \cos(\phi - \phi_n) + h \cos \theta. \end{aligned} \quad (7)$$

The electric field directly emitted from the hypothetical UCA is defined as follows by putting the r_{rn} delay term in the Equation (5):

$$\begin{aligned} E_r &= \frac{h_p}{v_p} e^{j \frac{\omega_0}{c} (tc-r)} \sum_{n=0}^{N-1} I_n \xi_n(\theta_{rn}, \phi_{rn}) \\ &= \frac{1}{r_{rn}} e^{j \frac{\omega_0}{c} [a \sin \theta \cos(\phi - \phi_n) - h \cos \theta]} e^{j l \phi_n}, \end{aligned} \quad (8)$$

The intervals of the hypothetical and real UCA elements to the observation point can be taken to be approximately ($r_{dn} \approx r_{rn} \approx r$) equal for the amplitude terms under the far-field approach ($r \gg a, h$). Similarly, the element positions of the UCA can be taken the same for the real and hypothetical array elements under the far-field ($\theta_{dn} \approx \theta_{rn} \approx \theta$ and $\phi_{dn} \approx \phi_{rn} \approx \phi$). Considering that all the elements in UCA are identical, the $\xi_n(\theta_{dn}, \phi_{dn})$ and $\xi_n(\theta_{rn}, \phi_{rn})$ expressions can be approximately equated to $\xi(\theta, \phi)$. The total electric field of the OAM waves transmitted to the observation point along both the line-of-sight path and the most fundamental path reflected from the ground plane can be approximately expressed as:

$$\begin{aligned} E_t &\approx \frac{e^{j \frac{\omega_0}{c} (tc-r)}}{r} \sum_{n=0}^{N-1} I_n \xi(\theta, \phi) e^{j \frac{\omega_0}{c} (a \sin \theta \cos(\phi - \phi_n))} e^{j l \phi_n} \\ &\quad \times \left[e^{j \frac{\omega_0}{c} (h \cos \theta)} \frac{h_p}{v_p} e^{-j \frac{\omega_0}{c} (h \cos \theta)} \right]. \end{aligned} \quad (9)$$

As a result, the expression of the total electric field for vertical and horizontal polarization at the observation point is

$$\begin{aligned} E_t &\approx \underbrace{\frac{e^{j k_0 (tc-r)}}{r} \xi(\theta, \phi)}_{\text{field of an element}} \underbrace{\sum_{n=0}^{N-1} I_n e^{j k_0 (a \sin \theta \cos(\phi - \phi_n))} e^{j l \phi_n}}_{\text{circular array factor}} \\ &\quad \times \underbrace{\left[\frac{2j \sin(k_0 h \cos \theta) h_p}{2 \cos(k_0 h \cos \theta) v_p} \right]}_{\text{multipath factor}}. \end{aligned} \quad (10)$$

where $k_0 = \omega_0/c$ represents the free space wave number.

The total electric field of the UCA located parallel to the superconducting ground plane involves a uniform circular array factor, element field, and multipath factor containing the most fundamental reflected path and the direct path. The multipath factor varies depending on the k_0 free space wave number, the θ elevation angle, and the h height (distance between the

ground plane and array), but also changes depending on the polarization (h_p and v_p).

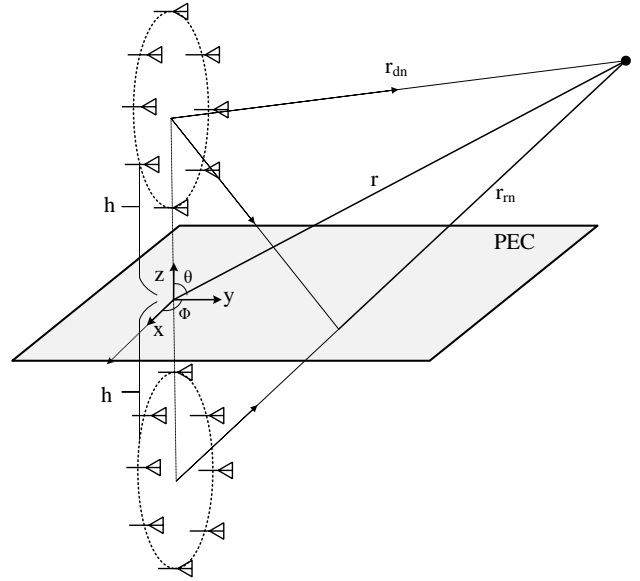


Fig. 2. UCA placed upright at a given height (h) from an infinitely sized superconducting ground plane

As seen in Figure 2, the N -element circular array is located at a h height from the superconducting ground plane and equidistant along a circular ring upright to the ground position. Similarly, the configuration of the UCA basically gives the array with a $2\pi l/N$ phase difference between the neighboring elements to obtain the OAM beam. Also, unlike parallel positioning, upright positioning also occurs symmetrically with respect to the ground position, with hypothetical array elements at different h depths below the ground plane. The OAM electric field propagating along the line of sight under the far-field approach when the UCA is located uprightly to the ground is given as:

$$E_d = \sum_{n=0}^{N-1} I_n \xi_n(\theta_{dn}, \phi_{dn}) \frac{e^{j \omega_0 (t - \frac{r_{dn}}{c})}}{r_{dn}} e^{j l \phi_n}, \quad (11)$$

In terms of the phase term, the $r_{dn} \cong r - \langle \hat{\mathbf{a}}_r, \mathbf{r}_n \rangle$ delay term is given by:

$$\begin{aligned} r_{dn} &\cong r - \langle \hat{\mathbf{a}}_r, (a \cos \phi_n \hat{\mathbf{a}}_x + (h - a \sin \phi_n) \hat{\mathbf{a}}_z) \rangle \\ &\cong r - a \sin \theta \cos \phi \cos \phi_n + a \cos \theta \sin \phi_n - h \cos \theta, \end{aligned} \quad (12)$$

where h is the interval from the array center to the ground plane. The reference plane of the ϕ_n angle is the x -axis. By combining the equation (12) with the equation (11), the electric field expression for the directly propagating OAM wave for the UCA situation located uprightly to the ground is defined by:

$$E_d = e^{j\frac{\omega_0}{c}(tc-r)} \sum_{n=0}^{N-1} I_n \xi_n(\theta_{dn}, \phi_{dn}) \frac{1}{r_{dn}} e^{j\frac{\omega_0}{c}[a\sin\theta\cos\phi\cos\phi_n - a\cos\theta\sin\phi_n + h\cos\theta]} e^{jl\phi_n}, \quad (13)$$

In the situation of UCA located upright to the ground plane, the most fundamental OAM electric field reflected by the ground plane is the same as that of the line-of-sight electric field propagated from the hypothetical arrays. The most fundamental electric field reflected by the ground plane in both the vertical and horizontal polarization states can be expressed as:

$$E_r = \frac{h_p}{v_p} \sum_{n=0}^{N-1} I_n \xi_n(\theta_{rn}, \phi_{rn}) \frac{e^{j\omega_0(t-\frac{r_{rn}}{c})}}{r_{rn}} e^{jl\phi_n}, \quad (14)$$

In terms of the phase term of the OAM wave reflected from the UCA located upright to the ground plane, the $r_{rn} \cong r - \langle \hat{\mathbf{a}}_r, \mathbf{r}'_n \rangle$ delay term can be expressed as:

$$\begin{aligned} r_{rn} &\cong r - \langle \hat{\mathbf{a}}_r, (a\cos\phi_n \hat{\mathbf{a}}_x + (-h - a\sin\phi_n) \hat{\mathbf{a}}_z) \rangle \\ &\cong r - a\sin\theta\cos\phi\cos\phi_n + a\cos\theta\sin\phi_n + h\cos\theta. \end{aligned} \quad (15)$$

The most fundamental electric field reflected by the ground plane of the UCA located upright to the ground position, together with the r_{rn} delay term, can be expressed as follows:

$$E_r = \frac{h_p}{v_p} e^{j\frac{\omega_0}{c}(tc-r)} \sum_{n=0}^{N-1} I_n \xi_n(\theta_{rn}, \phi_{rn}) \frac{1}{r_{rn}} e^{j\frac{\omega_0}{c}[a\sin\theta\cos\phi\cos\phi_n - a\cos\theta\sin\phi_n - h\cos\theta]} e^{jl\phi_n}, \quad (16)$$

Under the same conditions stated for the parallel placed UCA ($r_{dn} \approx r_{rn} \approx r$ and $\xi_n(\theta_{dn}, \phi_{dn}) \approx \xi_n(\theta_{rn}, \phi_{rn}) \approx \xi(\theta, \phi)$), the total electric field including the direct and most fundamental reflected radiations of the UCA located upright to the ground position can be expressed as:

$$\begin{aligned} E_t &\approx \frac{e^{j\frac{\omega_0}{c}(tc-r)}}{r} \sum_{n=0}^{N-1} I_n \xi(\theta, \phi) \\ &e^{j\frac{\omega_0}{c}(a\sin\theta\cos\phi\cos\phi_n - a\cos\theta\sin\phi_n)} e^{jl\phi_n} \\ &\times \left[e^{j\frac{\omega_0}{c}(h\cos\theta)} \frac{h_p}{v_p} e^{-j\frac{\omega_0}{c}(h\cos\theta)} \right]. \end{aligned} \quad (17)$$

The final electric field at the observing point of the UCA located upright to the ground for vertical and horizontal polarization is expressed by:

$$\begin{aligned} E_t &\approx \underbrace{\frac{e^{jk_0(tc-r)}}{r} \xi(\theta, \phi)}_{\text{field of an element}} \\ &\underbrace{\sum_{n=0}^{N-1} I_n e^{jk_0(a\sin\theta\cos\phi\cos\phi_n - a\cos\theta\sin\phi_n)} e^{jl\phi_n}}_{\text{circular array factor}} \\ &\times \underbrace{\left[\begin{array}{c} 2j\sin(k_0 h \cos\theta)_{h_p} \\ 2\cos(k_0 h \cos\theta)_{v_p} \end{array} \right]}_{\text{multipath factor}}. \end{aligned} \quad (18)$$

The total electric field of the UCA located upright to the superconducting ground plane differs from that of the parallel-located UCA in terms of the circular array factor. The multipath factor with multipath propagation features, which consists of two propagation paths, is the same for both array positions and varies with h height.

Based on the Nyquist sampling theorem, the largest OAM mode l_{max} that the UCA can produce depends on the number of elements in the array. Therefore, the maximum-mode OAM vortex beam number that can be obtained from the N -element UCA must satisfy the condition $N \geq 2|l_{max}| + 1$. Therefore, the parameter affecting the maximum number of modes that can be obtained from the OAM is the UCA element number [29].

On the other hand, the number of slices that can be obtained from OAM in the range $\theta \in [0, \frac{\pi}{2}]$ is determined as approximately $\frac{2h}{\lambda} + 1$ and $\frac{2h}{\lambda}$ for vertical and horizontal polarization cases, respectively. Similarly, the parameters that affect the maximum number of slices that can be obtained from OAM are the h height of the array elements from the ground plane and the λ wavelength [31], [32].

The number of UCA elements N and the height h , which is the distance between the ground plane and the array, are of critical importance, as they directly affect the number of users or devices that can be practically multiplexed and served without interference in certain communication systems.

III. NUMERICAL EXAMPLES

In this section, numerical examples are given to demonstrate and compare the multipath propagation performances of UCA located parallel and upright to the ground. The results are obtained simply by evaluating the most basic two-way analytical electric fields including the direct and most fundamental reflected constituent in Section 2. To illustrate the multipath characteristic of the OAM wave, let us first consider a parallel-positioned circular array ($a = 0.7\lambda$ radius and $h = 5\lambda$ height) with respect to the infinitely sized superconducting ground plane. The UCA with $f_0 = 5$ GHz center operating frequency is evaluated in the horizontal polarization situation. In addition, the $\phi_n = 2\pi n/N, n = 1, 2, 3, \dots, N$ phase is applied to each array element to obtain an OAM wave with the mode-1 ($l = 1$). The effect of frequency on multipath characteristics is present [9]. However, in this study, the height h is given in terms of wavelength λ to study the effect of height. Therefore, the same result is obtained at different frequencies.

As a result of the interference of OAM waves reaching the observing point with the direct and most fundamental reflected path, null values occur that divide the OAM beam into slices. Both the number and position of these nulls that slice the OAM beam in the elevation plane depend on the multipath characteristic (the $2\cos(k_0 h \cos\theta)$ term for the vertical polarization case is the multipath factor and the $2j\sin(k_0 h \cos\theta)$ term for the horizontal polarization case is the multipath factor). UCA's OAM radiation beam varies with the h height between the array and the ground position and the k_0 free space wave number. For the case where the absence of a ground plane, the three-dimensional (r, θ, ϕ) snapshot graph of the OAM beam with mod-1 obtained from the UCA located parallel to the x-y plane at a $h = 5\lambda$ height from the origin is given in the Figure 3(a). In the OAM radiation pattern of the UCA, where there is no ground plane, no nulls are occurred in the elevation plane, resulting in a stable OAM wave.

However, slices occur in the OAM radiation beam of the parallel-positioned UCA with respect to the infinitely sized superconducting ground plane. As seen in the three-dimensional (3-D) instantaneous graph in Figure 3(b), more than one ring is formed in the OAM radiation pattern due to the multipath characteristic. The number of these rings varies according to the h height variable between the array and the ground position. The OAM radiation pattern of the parallel-positioned UCA (at a height of $h = 5\lambda$) with respect to the infinitely sized superconducting ground plane is shown in Figure 3(b). Furthermore, with the effect of the multipath characteristic, approximately $\frac{2h}{\lambda} + 1$ and $\frac{2h}{\lambda}$ OAM pattern slices occur in the vertical and horizontal polarization states, respectively, in the $\theta \in [0, \frac{\pi}{2}]$ range. It is seen in the Figure 3(b) that the OAM radiation beam slice number in the $\theta \in [0, \frac{\pi}{2}]$ range of the UCA located parallel at a height of $h = 5\lambda$ for the horizontal polarization case is $\frac{2(5\lambda)}{\lambda} = 10$.

In addition, OAM beams produced by UCA with radius $a = 0.7\lambda$ located at the height of $h = 5\lambda$ from the origin for the isolated medium without ground plane are sampled at $z = 1\text{km}$ from the origin. The sampled OAM intensity pattern and helical phase wavefronts are illustrated in Figure 4(a) and Figure 4(b), respectively. In both cases, the obtained observation window plane with a width of 1 km in the x-y direction is upright to the beam axis. Figure 4(a) shows that in an isolated medium without a ground plane, a "doughnut" shaped intensity pattern of the $l = 1$ mode OAM wave is obtained. On the other hand, Figure 4(b) shows the spiral phase wavefront for the $l = 1$ mode OAM beam, where the phase change from 0 to 2π corresponds to a change in color from blue to red.

By sampling the radiation pattern of the parallel-positioned UCA (radius $a = 0.7\lambda$ and at a height of $h = 5\lambda$) with respect to the infinitely sized superconducting ground plane, the intensity pattern and helical phase wavefronts of the $l = 1$ mode OAM beams for the ground plane case are obtained similarly. In Figure 5, more than one ring-shaped distribution is observed both in the intensity pattern (Figure 5(a)) and in the phase wavefront (Figure 5(b)), with the observation plane with a width of 1 km in the x-y direction formed by the sample window at $z = 1$ km.

Since the h height value is a variable of the multipath factor ($2\cos(k_0 h \cos\theta)$ for the vertical polarization, $2j\sin(k_0 h \cos\theta)$ for the horizontal polarization), it is clear that if the UCA has various heights, it will have different positions and a number of OAM pattern slices. Figure 6(a) shows the 3-D OAM beam pattern of the UCA located parallel to the $h = 3\lambda$ height from the infinitely sized superconducting ground plane. As seen in the Figure 6(a), 6 ($\frac{2(3\lambda)}{\lambda} = 6$) slices of OAM pattern are formed in the $\theta \in [0, \frac{\pi}{2}]$ range of the UCA located at a $h = 3\lambda$ height. The intensity pattern of the UCA, which is $h = 3\lambda$ above the ground plane in Figure 6(b), and the phase wavefront of the UCA, which is $h = 3\lambda$ above the ground plane in Figure 6(c) are observed with the observation window with a width of 1 km in the x-y direction formed by the sample window at $z = 1$ km. The phase wavefront and the intensity pattern with the "donut" shaped distribution of the OAM wave formed by the UCA at the $h = 3\lambda$ height over the ground are divided into two slices. The number of the OAM main pattern slices consists of 3 slices for $h = 5\lambda$ in the previous example, depending on the h height.

Similarly, the 3-D OAM beam pattern of the parallel-positioned UCA (at a height of $h = 7\lambda$) with respect to the infinitely sized superconducting ground plane is shown in Figure 7(a). It is clearly seen from Figure 7(a) that 14 OAM radiation beam slices are formed in the $\theta \in [0, \frac{\pi}{2}]$ interval for the situation where the UCA is located at a $h = 7\lambda$ height from the ground position. It is seen that the "ring" shaped distribution intensity pattern and phase wavefront of the main OAM wave generated by the UCA at a $h = 7\lambda$ height over the ground plane is divided into four slices. It can also be seen from the various examples above that the number of main OAM radiation beam slices varies in relation to the h height.

On the other hand, let's examine the multipath propagation effects of the OAM wave by considering the same circular array upright to the ground plane (Figure 2) and at the height of $h = 5\lambda$ over the infinitely sized superconducting ground plane. First, where the ground plane is not considered, the center of the UCA located upright to the x-y plane is located at a $h = 5\lambda$ height from the origin. The three-dimensional snapshot graph of the OAM beam with mode-1 obtained for the case where the ground plane is not taken into account is examined in Figure 8. It can be seen from Figure 8 that the UCA located upright to the x-y plane generates the stable OAM beam with mod-1 in the y-direction. Figure 8(a) shows the half wave shape of the OAM beam, while Figure 8(b) shows the full OAM beam. As can be seen from both figures, a uniform OAM beam is obtained in the y-axis direction, which is the normal of the UCA, in an isolated environment where there is no ground plane.

The 3-D OAM beam of UCA, which is located upright to the $h = 5\lambda$ height from the ground plane, has reflections from the superconducting ground plane with infinite dimensions in addition to direct propagation. In the case of multipath propagation, where there is the most fundamental reflected radiation as well as direct radiation, the radiated OAM beam is affected by the multipath factor. Therefore, in the OAM radiation generated by the UCA located upright to the ground plane, similarly, nulls are formed in the elevation plane that

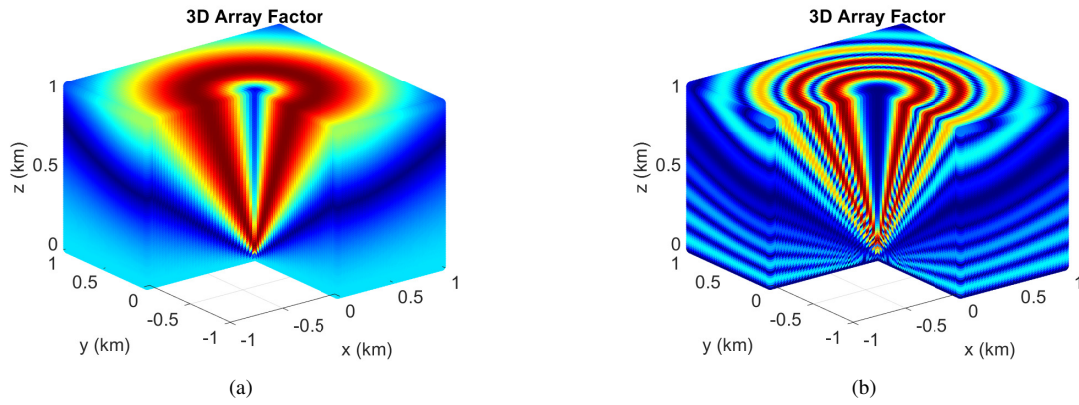


Fig. 3. 3-D OAM beam pattern snapshot graph of UCA with mod-1, relative to the interval r at constant angle $\theta = 0$ and $\phi = 0$ (a) in the case where there is no ground plane, (b) in the case of the ground plane.

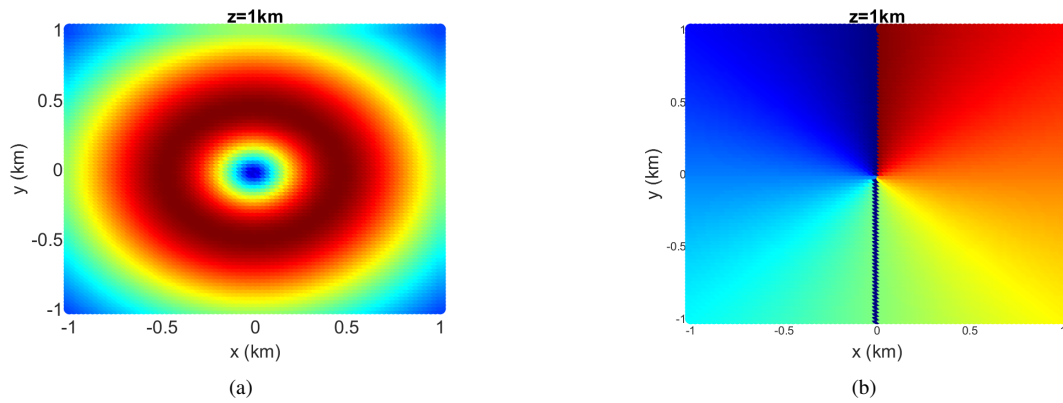


Fig. 4. (a) intensity pattern and (b) helical phase wavefront at $z = 1\text{km}$ of OAM beams produced by UCA with radius $a = 0.7\lambda$ located at the height of $h = 5\lambda$ from the origin for an isolated medium without a ground plane.

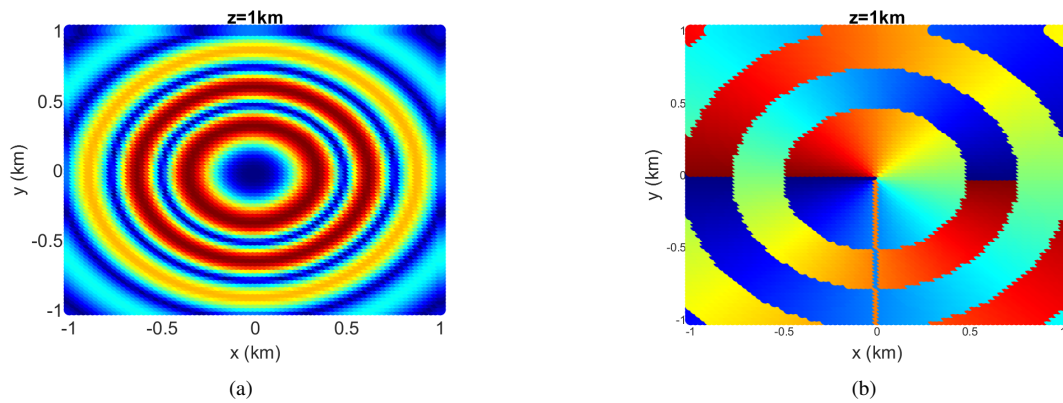


Fig. 5. (a) intensity pattern and (b) helical phase wavefront at $z = 1\text{km}$ of OAM beams produced by the parallel-positioned UCA (radius $a = 0.7\lambda$ and at a height of $h = 5\lambda$) with respect to the infinitely sized superconducting ground plane in the x - y plane.

divides the OAM beam into slices. Figure 9(a) and Figure 9(b) show the half and full OAM beams of the sliced OAM wave as a result of nulls resulting from the multipath effect, respectively. In both Figures, it can be seen that the UCA located uprightly at a height of $h = 5\lambda$ for the horizontal polarization case has $\frac{2(5\lambda)}{\lambda} = 10$ OAM radiation beam separate into segments in the $\theta \in [0, \frac{\pi}{2}]$ range.

Positioned both parallelly and uprightly to a supercon-

ducting ground plane with infinite dimensions, the OAM radiation beam of the UCA is segmented in the elevation plane depending on the height from the ground position. The number and position of nulls that separate into segments of the OAM radiation beam vary depending on the multipath factor.

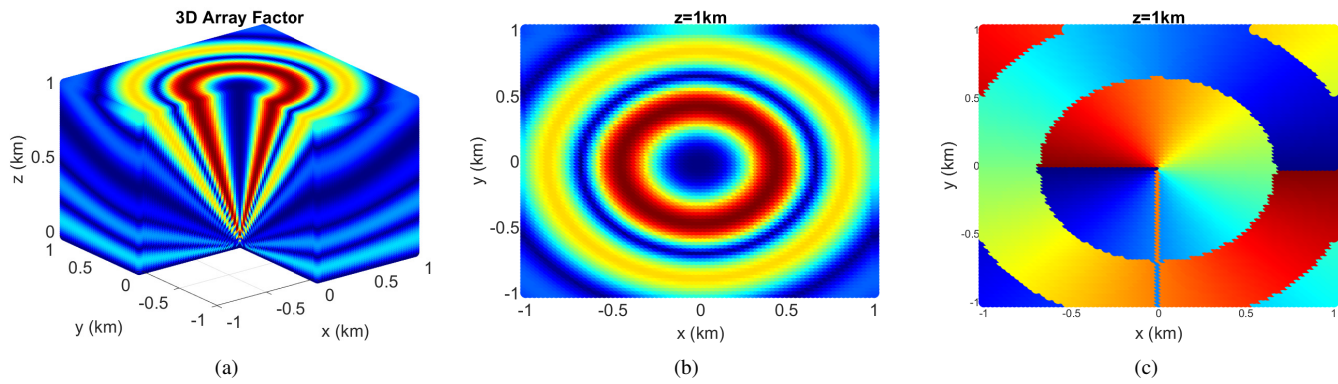


Fig. 6. (a) 3-D OAM beam pattern snapshot graph of the UCA with radius $a = 0.7\lambda$ located parallel to the $h = 3\lambda$ height from the infinitely sized superconducting ground plane in the x-y plane. (b) intensity pattern and (c) helical phase wavefront at $z = 1\text{km}$ of OAM beams produced by UCA located parallel to the $h = 3\lambda$ height from the x-y plane.

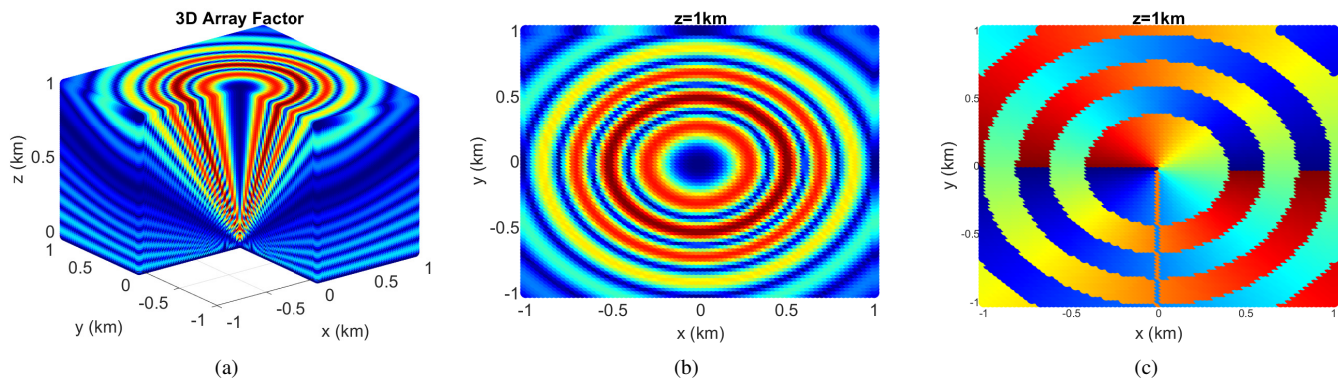


Fig. 7. (a) 3-D OAM beam pattern snapshot graph of the UCA with radius $a = 0.7\lambda$ located parallel to the $h = 7\lambda$ height from the infinitely sized superconducting ground plane in the x-y plane. (b) intensity pattern and (c) helical phase wavefront at $z = 1\text{km}$ of OAM beams produced by UCA located parallel to the $h = 7\lambda$ height from the x-y plane.

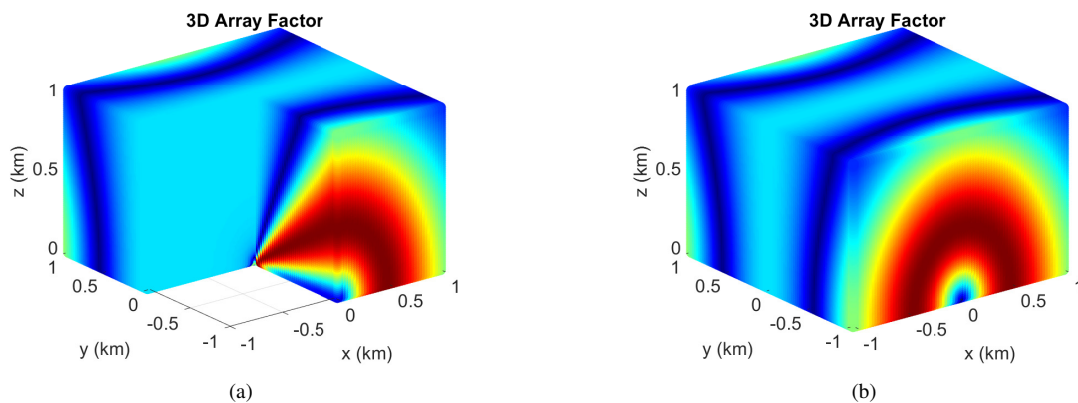


Fig. 8. (a) Half and (b) a full 3-D snapshot graph of the OAM wave formed along the y-axis of the UCA located uprightly and at a $h = 5\lambda$ height from the x-y plane in the absence of the ground plane

IV. CONCLUSION

The multipath characteristic for an OAM beam containing one direct and one reflection path, with a more realistic approach compared to the isolated medium, is investigated in this study. In this sense, the total electric field at the observation point, which includes the direct and most fundamental reflected radiation, is derived from the parallel and upright-positioned UCA with respect to the infinitely sized super-

conducting ground plane. Unlike the electric field expression obtained in an isolated environment, the antenna element's field and the UCA array factor as well as the multipath factor are included. The OAM radiation model is segmented in the elevation plane due to the nulls generated by the multipath factor based on the height between the array and the ground position. As a result, the OAM radiation properties of UCA in an isolated environment and at a given height above the

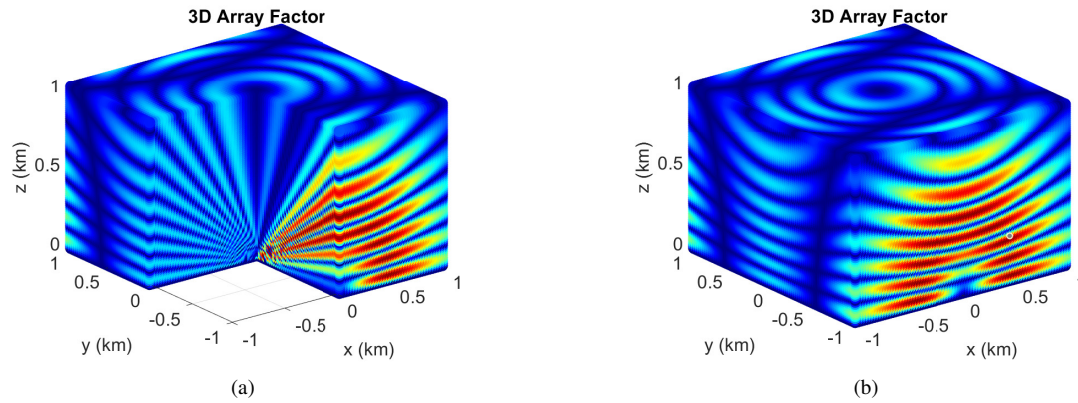


Fig. 9. (a) Half and (b) a full 3-D snapshot graph of the OAM wave formed along the y-axis of the upright-positioned UCA (at a height of $h = 5\lambda$) with respect to the infinitely sized superconducting ground plane in the x-y plane

ground are analytically demonstrated by deriving theoretical expressions and comparative simulation results.

REFERENCES

- [1] F. Tamburini, E. Mari, A. Sponselli, B. Thidé, A. Bianchini, and F. Romanato, "Encoding many channels on the same frequency through radio vorticity: first experimental test," *New Journal of Physics*, vol. 14, no. 3, p. 033001, Mar. 2012.
- [2] F. E. Mahmoudi and S. D. Walker, "4-gbps uncompressed video transmission over a 60-ghz orbital angular momentum wireless channel," *IEEE Wireless Communications Letters*, vol. 2, no. 2, pp. 223–226, 2013.
- [3] A. E. Willner, "Communication with a twist," *IEEE Spectrum*, vol. 53, no. 8, pp. 34–39, 2016.
- [4] R. Gaffoglio, A. Cagliero, G. Vecchi, and F. P. Andriulli, "Vortex waves and channel capacity: Hopes and reality," *IEEE Access*, vol. 6, pp. 19 814–19 822, 2018.
- [5] S. Yu, N. Kou, J. Jiang, Z. Ding, and Z. Zhang, "Beam steering of orbital angular momentum vortex waves with spherical conformal array," *IEEE Antennas and Wireless Propagation Letters*, vol. 20, no. 7, pp. 1244–1248, 2021.
- [6] Z. Yu, C. Han, Y. Zou, and X. Lu, "Location and angular velocity detection using a circular frequency diverse array radar," in *2021 IEEE Asia-Pacific Microwave Conference (APMC)*, 2021, pp. 58–60.
- [7] J. Luo, S. Wang, and F. Wang, "Secure range-dependent transmission with orbital angular momentum," *IEEE Communications Letters*, vol. 23, no. 7, pp. 1178–1181, 2019.
- [8] J. Ma, X. Song, Y. Yao, Z. Zheng, X. Gao, and S. Huang, "Secure transmission of radio orbital angular momentum beams based on the frequency diverse array," *IEEE Access*, vol. 9, pp. 108 924–108 931, 2021.
- [9] G. X. e. a. Yan Yan, Long Li, "Multipath effects in millimetre-wave wireless communication using orbital angular momentum multiplexing," *Scientific Reports*, vol. 6, no. 3348, 2016.
- [10] S. K. N. et al., "A review of orbital angular momentum vortex waves for the next generation wireless communications," in *IEEE Access*, vol. 10, pp. 89 465–89 484, 2022.
- [11] C. F. J. Li, X. Pang, "Electromagnetic wave with oam and its potential applications in iot," in *Lecture Notes of the Institute for Computer Sciences, Social Informatics and Telecommunications Engineering*, vol. 316, 2020.
- [12] L. Allen, M. W. Beijersbergen, R. J. C. Spreeuw, and J. P. Woerdman, "Orbital angular momentum of light and the transformation of laguerre-gaussian laser modes," *Phys. Rev. A*, vol. 45, pp. 8185–8189, Jun 1992. [Online]. Available: <https://link.aps.org/doi/10.1103/PhysRevA.45.8185>
- [13] K. Liu, Y. Cheng, X. Li, Y. Qin, H. Wang, and Y. Jiang, "Generation of orbital angular momentum beams for electromagnetic vortex imaging," *IEEE Antennas and Wireless Propagation Letters*, vol. 15, pp. 1873–1876, 2016.
- [14] R. Chen, H. Zhou, M. Moretti, X. Wang, and J. Li, "Orbital angular momentum waves: Generation, detection, and emerging applications," *IEEE Communications Surveys & Tutorials*, vol. 22, no. 2, pp. 840–868, 2020.
- [15] Y. Wang, X. Sun, and L. Liu, "A concentric array for generating multimode oam waves," *Journal of Communications and Information Networks*, vol. 7, no. 3, pp. 324–332, 2022.
- [16] M. Wulff, T. Zhang, L. Wang, H.-D. Brüns, and C. Schuster, "Simulating aperture coupling of oam waves through an infinite pec plane using efie-mom—part i: Validation and numerical accuracy," *IEEE Transactions on Electromagnetic Compatibility*, vol. 65, no. 5, pp. 1389–1399, 2023.
- [17] B. Thidé, H. Then, J. Sjöholm, K. Palmer, J. Bergman, T. D. Carozzi, Y. N. Istomin, N. H. Ibragimov, and R. Khamitova, "Utilization of photon orbital angular momentum in the low-frequency radio domain," *Phys. Rev. Lett.*, vol. 99, p. 087701, Aug 2007. [Online]. Available: <https://link.aps.org/doi/10.1103/PhysRevLett.99.087701>
- [18] U. M and T. A., "Generation of electron beams carrying orbital angular momentum," *Nature*, vol. 464, no. 7289, pp. 737–739, 2010.
- [19] R. Niemiec, C. Brousseau, K. Mahdjoubi, O. Emile, and A. Ménard, "Characterization of an oam flat-plate antenna in the millimeter frequency band," *IEEE Antennas and Wireless Propagation Letters*, vol. 13, pp. 1011–1014, 2014.
- [20] H.-H. Lv, Q.-L. Huang, X.-J. Yi, J.-Q. Hou, and X.-W. Shi, "Low-profile transmitting metasurface using single dielectric substrate for oam generation," *IEEE Antennas and Wireless Propagation Letters*, vol. 19, no. 5, pp. 881–885, 2020.
- [21] M. Alibakhshi-Kenari, M. Naser-Moghadasi, R. Sadeghzadeh, B. S. Virdee, and E. Limiti, "Traveling-wave antenna based on metamaterial transmission line structure for use in multiple wireless communication applications," *AEU - International Journal of Electronics and Communications*, vol. 70, no. 12, pp. 1645–1650, 2016. [Online]. Available: <https://www.sciencedirect.com/science/article/pii/S1434841116309086>
- [22] M. Wulff, L. Wang, H.-D. Brüns, and C. Schuster, "Simulating aperture coupling of oam waves through an infinite pec plane using efie-mom—part ii: Application and interpretation," *IEEE Transactions on Electromagnetic Compatibility*, vol. 65, no. 5, pp. 1400–1409, 2023.
- [23] T. Yuan, Y. Cheng, H. Wang, and Y. Qin, "Beam steering for electromagnetic vortex imaging using uniform circular arrays," *IEEE Antennas and Wireless Propagation Letters*, vol. 16, pp. 704–707, 2017.
- [24] M. Lin, Y. Gao, P. Liu, and J. Liu, "Theoretical analyses and design of circular array to generate orbital angular momentum," *IEEE Transactions on Antennas and Propagation*, vol. 65, no. 7, pp. 3510–3519, 2017.
- [25] K. Liu, Y. Cheng, X. Li, Y. Qin, H. Wang, and Y. Jiang, "Generation of orbital angular momentum beams for electromagnetic vortex imaging," *IEEE Antennas and Wireless Propagation Letters*, vol. 15, pp. 1873–1876, 2016.
- [26] L. Fang and R. M. Henderson, "Orbital angular momentum uniform circular antenna array design and optimization-based array factor," in *2019 IEEE Texas Symposium on Wireless and Microwave Circuits and Systems (WMCS)*, 2019, pp. 1–4.
- [27] T. Yuan, H. Wang, Y. Qin, and Y. Cheng, "Electromagnetic vortex imaging using uniform concentric circular arrays," *IEEE Antennas and Wireless Propagation Letters*, vol. 15, pp. 1024–1027, 2016.
- [28] Y. Qin, K. Liu, Y. Cheng, X. Li, H. Wang, and Y. Gao, "Sidelobe suppression and beam collimation in the generation of vortex electromagnetic waves for radar imaging," *IEEE Antennas and Wireless Propagation Letters*, vol. 16, pp. 1289–1292, 2017.

- [29] U. Yesilyurt and H. K. Polat, "Helical circular array configurations for generation of orbital angular momentum beams," *IEEE Antennas and Wireless Propagation Letters*, vol. 22, no. 5, pp. 1139–1143, 2023.
- [30] L. Wang, W. Park, C. Yang, H.-D. Brüns, D. G. Kam, and C. Schuster, "Wireless communication of radio waves carrying orbital angular momentum (oam) above an infinite ground plane," *IEEE Transactions on Electromagnetic Compatibility*, vol. 62, no. 5, pp. 2257–2264, 2020.
- [31] U. Yesilyurt, I. Kanbaz, and E. Aksoy, "Effect of ground plane on power losses and efficiency for uniform period time modulated arrays," *IEEE Sensors Journal*, vol. 22, no. 4, pp. 3637–3647, 2022.
- [32] —, "Power losses and efficiency analysis of non-uniform time modulated arrays over a ground plane," *AEU - International Journal of Electronics and Communications*, vol. 146, p. 154106, 2022. [Online]. Available: <https://www.sciencedirect.com/science/article/pii/S1434841122000036>



Ugur Yesilyurt was born in Erzurum, Turkey, in 1990. He received a bachelor's degree from the Department of Electrical and Electronics Engineering, Atatürk University, Erzurum, in 2013, and the M.Sc. and Ph.D. degrees in electrical and electronics engineering from Gazi University, Ankara, Turkey, in 2018 and 2023, respectively. He is currently an Assistant Professor at Erzurum Technical University. His research interests include antenna radiation patterns, time-modulated antenna arrays, frequency-diverse arrays, orbital angular momentum, and antenna design.

antenna design.

Average Wind Speed Prediction in Giresun-Kümbet Plateau Region with Artificial Neural Networks

Ferdi Ozbilgin, Huseyin Calik and Mehmet Cem Dikbas


Abstract— In order to estimate the electricity generation capacity and schedule the supply for vendor needs, wind speed prediction is crucial for wind power plant frameworks. Prior to the installation of the wind power plants, a reliable wind behavior model is necessary. To have such a model, wind data is recorded periodically. In this study, hourly recorded meteorological data of actual pressure, relative humidity, temperature, wind direction and average wind speed for the year 2023 were obtained from the General Directorate of Meteorology for the Kümbet plateau region of Giresun province. The data is used to accurately predict the future wind speed for the region. MATLAB Artificial Neural Networks (ANN) is utilized. Actual pressure, relative humidity, temperature and wind direction parameters are defined as inputs in the prediction process, while the average wind speed is the output parameter. 85% of the data set is used as training data and remaining 15% data set is used for testing data. An optimization process is applied to determine the number of hidden layers to have the prediction value with the smallest error. Bayesian Regularization training process was performed by seeing that the hidden layer has the lowest error at 90 neurons. Performance evaluations are performed with Mean Square Error (MSE), Mean Absolute Error (MAE), Root Mean Square Error (RMSE) and Pearson Correlation Coefficient (R) metrics. The values of the metrics for the test data are 26.7137, 5.1685, 3.5055 and 0.7457 respectively. The results show that, ANN based model is useful for the wind speed prediction over the region.

Index Terms— Wind speed. Artificial neural networks. Forecasting. Giresun.


I. INTRODUCTION

WIND ENERGY has an key role in electricity markets as it is a environmentally safe energy source. According to


Ferdi Özbilgin, is with the department of Electrical and Electronic Engineering, Giresun University, Giresun, Türkiye.
(e-mail: ferdi.ozbilgin@giresun.edu.tr).

 <https://orcid.org/0000-0003-4946-7018>

Hüseyin Çalık, is with the department of Electrical and Electronic Engineering, Giresun University, Giresun, Türkiye.
(e-mail: huseyin.calik@giresun.edu.tr).

 <https://orcid.org/0000-0001-8298-8945>

Mehmet Cem Dikbas, is with the department of Electrical and Electronic Engineering, Giresun University, Giresun, Türkiye.
(e-mail: mehmet.dikbas@giresun.edu.tr).

 <https://orcid.org/0000-0003-4525-7996>

Manuscript received July 12, 2023; accepted Sep 23, 2024.

DOI: [10.17694/bajece.1515244](https://doi.org/10.17694/bajece.1515244)

the 2024 report of the Global Wind Energy Council (GWEC), installed wind power capacity worldwide reached approximately 1,021 GW by the end of 2023. 117 GW of new capacity was added in 2023, which means an increase of 50% compared to the previous year [1]. Turkey, with an installed capacity of 11,643 MW, ranks 10th in the world in annual electricity generation with China at the top and 5th in Europe with Germany at the top [2, 3].

In Figure 1, the Wind Energy Potential Atlas (REPA) prepared by the Ministry of Energy and Natural Resources shows the distribution of annual average wind speeds at a height of 100 meters in Turkey [4]. It can be seen that there is a significant wind energy potential in the coastal regions of Turkey. The regions with the highest wind capacity in Turkey are the Marmara, the Aegean and the Mediterranean coasts where the majority of wind power plants are installed. The Central Anatolian, the Black Sea, the Southeastern Anatolian and the Eastern Anatolian regions are the second most common regions for wind power plant installations [5].

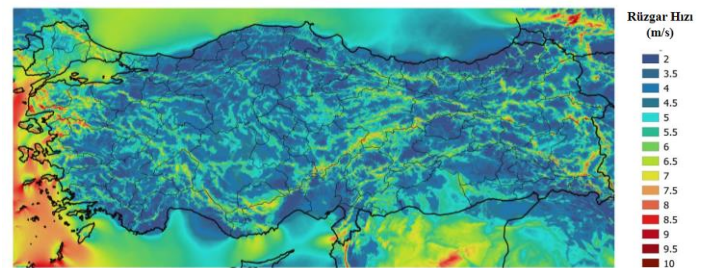


Fig.1. Turkey-wide annual average wind speed distribution at 100 meters [4]

Figure 2 shows the wind speed distributions in 100 meters for Giresun province. The average wind speed is 3.98 m/s throughout the province and reaches approximately 9 m/s in the central parts of the province.

The variability and unpredictability of wind speeds define difficulties in the stable supply of wind energy, therefore cause additional operating costs [6-8]. Thus, it is extremely important to develop effective wind speed forecasting methods to optimize the use of wind energy for electric power systems and minimize the waste of wind resources [9].

Accurate wind speed forecasting is crucial for predicting the energy production of wind turbines in the short, medium and long term. These forecasts can be used to calculate the profitability of power generation facilities and for investors to determine the feasibility of wind energy in a particular region

[10]. In addition, accurate short-term and long-term wind power generation forecasts are very important for maintaining a balanced electricity generation between different sources. Wind speed forecasts can be categorized as short-term and long-term. The most commonly used approaches in the literature for short-term wind speed forecasting for the purpose of determining electricity energy exchange mainly include autoregressive methodologies, autoregressive moving average techniques and wavelet transform methodologies. These methods give better results, especially for a few hours [11]. In case of longer forecasting times, error rates increase and these methods cannot provide reliable results [12]. Long-term wind speed forecasting is used for maintenance planning, unit commitment decisions and optimal operating cost applications.

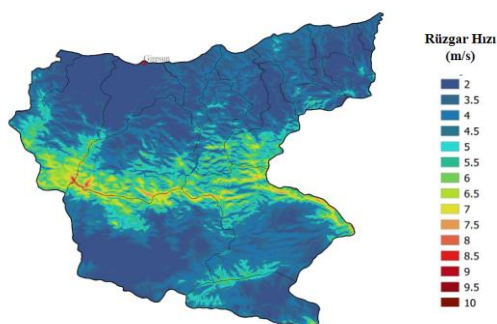


Fig.2. Annual average wind speed distribution at 100 meters in Giresun province [4]

Wind speed values were estimated based on ARIMA and artificial neural network methods using data from TÜBİTAK T60 Observatory meteorological station for the month of April 2016 [13]. In another study, specific to Konya province, 365 previous year data were used and wind speed values were estimated with ANN, based on temperature, pressure and humidity values [12]. Wind speed, humidity, pressure and temperature data of Bozcada district of Çanakkale province in 2014 were estimated by using Linear Regression and ANN. WEKA and MATLAB programming languages comparison was performed, and the correlation coefficient value for test data for ANN was found to be 0.63 [14]. Another study for Istanbul Avclar region was performed. Nonlinear Autoregressive Exogenous (NARX) method was used for this particular study. The data collected for 10 minutes as wind speed, wind direction, temperature, relative humidity and pressure. The R value for the test data was found to be 0.98 [15]. Additional studies using various statistical and artificial neural network methods such as ARIMA, ANN, NARX, RNN, LSTM were performed for the regions of Tokat [16], Bilecik [17], Burdur [18] and Yalova [19] provinces.

Wind speed prediction studies for Turkey were performed mostly for western and southern part of Turkey. Although the coastal line of Black Sea region receive comparatively less wind, the situation is opposite for the highland parts of the region which can be seen from Figure 1. It is observed that, the average wind speed for Giresun province center at the coast of Black Sea is around 3.98 m/s. On the other hand, this value drastically changes to have an average value of 9 m/s in

highland parts of the province. While existing studies focused on different provinces of Turkey, this study stands out by providing the first wind speed prediction for Giresun, an area previously overlooked in the literature. In contrast to other studies that typically rely on data from limited timeframes or specific meteorological stations, this study incorporates comprehensive, hourly recorded data for the entire year 2023.

In this study, wind speed was estimated by using hourly recorded actual pressure, relative humidity, temperature, wind direction and average wind speed data for the year 2023. The data is provided by General Directorate of Meteorology for Giresun province. The analyses are performed with ANN algorithm using MATLAB programming language. As a result of the prediction process in ANN trained with Bayesian regularization, performance evaluation is performed with MSE, RMSE, MAE and R metrics.

II. MATERIALS AND METHOD

A. Data Set and Preprocessing

In this study, the data obtained from Meteorological Station 17686 located at Kümbet Plateau (40°33'33.0 "N 38°26'23.0 "E) within the borders of Giresun Province are used. The location information of the station is given below.



Fig.3. Map image of the station used in the study

The data covering the period between 01.01.2023-31.12.2023 includes hourly actual pressure, relative humidity, temperature, wind direction and average wind speed data. In order for the data to be ready for analysis, it is necessary to go through some preprocess stages. As it is known, since the measurement stations are located in the plateau, there happens transportation and communication problems especially in winter months. Missing data occur as a result of power outage or sensor malfunction. Therefore, it is necessary to eliminate the missing data. The process of removing the missing data was carried out using the 'Data Clean' application in the MATLAB program. While the data for the wind direction parameter was determined according to the closest value, the missing data in other parameters were eliminated using the linear interpolation method.

The location of station 17686 has an altitude of 1724 meters. Since the location of the station is on the foothills of the mountain, and there are structures with trees around it, it was thought that the values of temperature, pressure and wind speed would not represent the location of the wind farm with

sufficient accuracy. For this reason, the measured values were moved to a height of 200 meters. The following formulae were used for the transfer process [20].

$$T = 15.04 - 0.00649 \cdot h \tag{1}$$

$$p = p_0 \left(1 - \frac{L \cdot h}{T_0} \right)^{\frac{g \cdot M}{R_0 L}} \tag{2}$$

$$\frac{V_2}{V_1} = \frac{\ln\left(\frac{h_2}{h_1}\right)}{\ln\left(\frac{h_1}{h_0}\right)} \tag{3}$$

In the equations: T is the temperature (°C), h is the altitude in meters, p is the actual pressure, V₁ and V₂ are the wind speeds at 1724 m and 1924 m altitude respectively, L is the temperature gradient, T₀ is the reference temperature at sea level, g is the gravitational acceleration, M is the mole mass and R₀ is the gas constant.

Table 1 shows the statistical properties of these parameters. Among these parameters, Actual Pressure and Wind Direction are generally distributed in a stable manner, while Relative Humidity has a wide distribution. Temperature shows a significant variability with a large standard deviation, while Mean Wind Speed shows a large variability with high minimum and maximum values. Pearson correlation analysis was performed to determine the relationship between these parameters.

TABLE I
STATISTICAL VALUES OF THE PARAMETERS IN THE DATA SET

Parameter name	Status	Mean	Standard Deviation	Minimum Value	Maximum Value	Median
Actual Pressure [mbar]	Input	0.81	0.01	0.79	0.82	0.81
Relative Humidity [%Rh]	Input	0.78	0.25	0.09	1.00	0.95
Temperature [°C]	Input	6.48	7.04	-14.80	28.80	6.90
Wind Direction	Input	0.47	0.29	0.00	0.94	0.50
Average Wind Speed [m/s]	Output	9.22	7.54	0.00	81.55	7.12

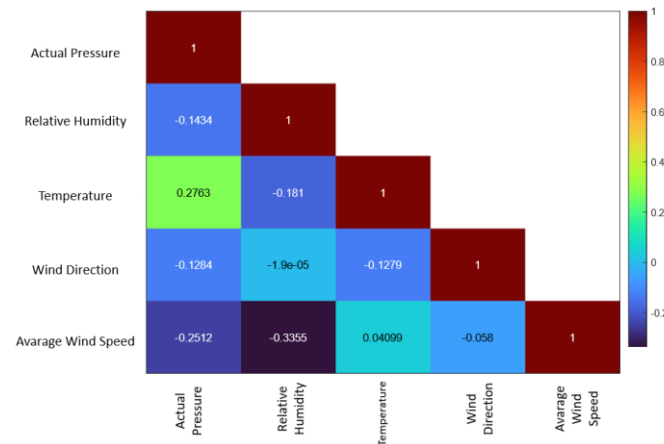


Fig.4. Correlation heat map of the variables in the data set

Figure 4 is a heat map showing the Pearson correlation coefficients between the meteorological parameters in the data set. The color scale represents the strength and direction of these correlations, with red indicating strong positive correlations, blue representing strong negative correlations, and lighter shades indicating weaker correlations. There is a positive correlation between Actual Pressure and Temperature, indicating that as the pressure increases, the temperature also increases (R = 0.2763, moderate correlation). While there are negative correlations between Actual Pressure and Relative Humidity (R = -0.1434), there are also negative correlations between Relative Humidity and Temperature (R = -0.181). There is no significant relationship between Wind Direction and other parameters. There are significant negative correlations between Wind Speed and Actual Pressure (R = -0.2512) and Relative Humidity (R = -0.3355), indicating that as wind speed increases, pressure and relative humidity decrease.

There is a weak positive correlation between Temperature and Mean Wind Speed (R = 0.04099), indicating that wind speed increases slightly as temperature increases. No significant relationship was observed between wind direction and mean wind speed (R = -0.058).

B. Artificial Neural Networks

Artificial neural networks are one of the supervised machine learning methods frequently used in regression problems. Inspired by the behavior of the brain and nerve cells, the algorithm includes data processing and decision-making processes. ANNs basically consist of input layer, hidden layer and output layer. The input layer contains neurons corresponding to the number of features in the data set. Each neuron represents one feature from the data set. The hidden layer(s) are the neurons that process the input data and transmit it to the output layer. The number of neurons in each hidden layer can vary depending on the complexity of the problem and the size of the data set. The output layer contains neurons that represent what the model is trying to predict [21, 22]. The ANN architecture used in the study is shown in Figure 5.

Each neuron in an Artificial Neural Network (ANN) performs information processing by weighting incoming signals and processing them through an activation function. The weights express the strength of synaptic connections and quantitatively determine the strength of the relationship between each input and the corresponding neuron. During the training of the network, these weights are iteratively adjusted to minimize the error rate using the backpropagation algorithm. The activation function is a generally non-linear function used to calculate the output of the neuron. This function determines the potential of the neuron and activates the neuron if it is above

a certain threshold value. Various activation functions such as sigmoid, tanh, ReLU can be preferred according to different problems and network structures [23, 24].

$$y = \sum (w_i \times x_i) + b \tag{4}$$

Where y is the signal of the neuron, w_i is the weight of the i -th input, x_i is the i -th input value and b is the bias value.

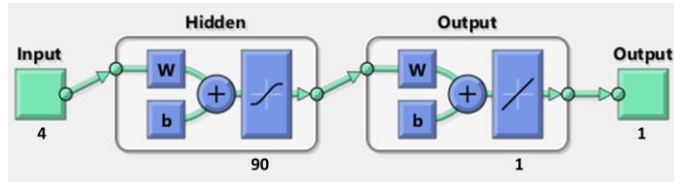


Fig.5. ANN architecture used in the study

In ANNs, two important techniques are the Lavenberg-Marquardt algorithm and Bayesian regularization, which strike a balance between the complexity of the model and the error function, preventing overlearning and increasing the generalization ability of the model. The Lavenberg-Marquardt algorithm uses a combination of steepest descent and Gauss-Newton methods to minimize the error function, while Bayesian regularization updates the weights of the model by adding an additional regularization term to the error term [25].

C. Performance Evaluation

In the study, Mean Square Error (MSE), Mean Absolute Error (MAE), Root Mean Square Error (RMSE) and Pearson Correlation Coefficient (R) metrics, which are frequently used in the literature, were used for performance evaluations as a result of prediction of wind speed values. The mathematical expressions of the performance metrics are as follows.

$$MSE = \frac{1}{N} \sum_{i=1}^N (y_i - \hat{y}_i)^2 \tag{5}$$

$$MAE = \frac{1}{N} \sum_{i=1}^N |y_i - \hat{y}_i| \tag{6}$$

$$RMSE = \sqrt{\frac{\sum_{i=1}^N (y_i - \hat{y}_i)^2}{N}} \tag{7}$$

$$R = \frac{cov(y, \hat{y})}{\sigma_y \sigma_{\hat{y}}} \tag{8}$$

Where y is the actual value of wind speed, \hat{y} is the estimated value of wind speed, σ is the standard deviation, cov is the covariance and N is the number of estimated data.

III. RESULTS

In this section, findings related to wind speed prediction results are presented. Wind speed was predicted by ANN using the values of Actual Pressure, Relative Humidity, Temperature and Wind direction and MSE, MAE, RMSE and R metric

values were calculated as a result of the prediction. The analysis was carried out using MATLAB programming language and a computer system equipped with Intel Core i7-13700H 2.40 GHz Processor, 32 GB RAM and 8 GB RTX4070 Graphics Card.

In the training phase of the ANN, Levenberg-Marquardt and Bayesian regularization algorithms were tested. Bayesian regularization algorithm, which is superior to the Levenberg-Marquardt model, was used. The training was performed using the *trainbr* function in the MATLAB package program. The highest success rate was achieved by using the tangent sigmoid (tansig) function as the activation function.

Figure 6 shows the variation of MSE values of the training data according to the number of neurons in the hidden layer in the ANN architecture. It was determined that the number of neurons with the lowest error was 90 and the MSE value for this case was calculated as 21.2192.

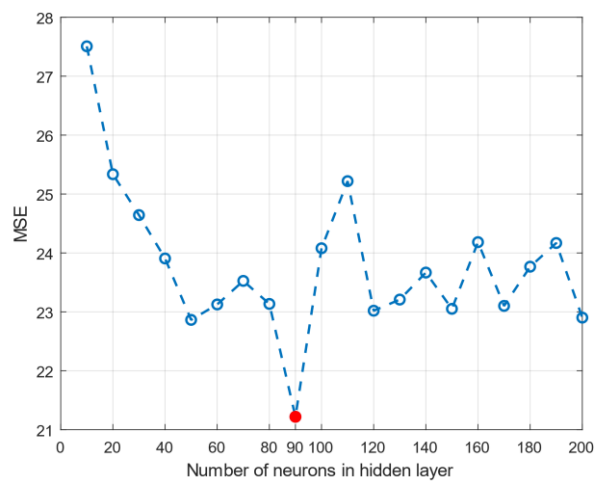


Fig.6. The relationship between the number of neurons in the hidden layer and error

Figure 7 shows the performance information of the network for training and test data during the training process. The X axis represents the number of iterations and the Y axis represents the MSE values calculated for each iteration in the graph. Training outputs are shown in blue and test outputs are shown in red. At epoch 1000, the best performance (MSE 21.2192) was obtained and the training process was finished.

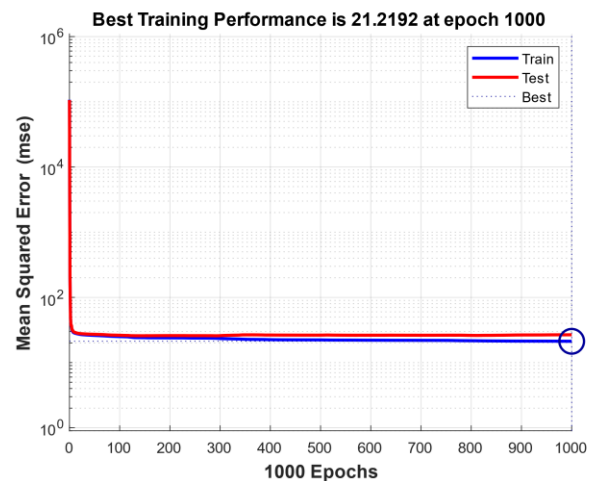


Fig.7. MSE values of training and test data during the training process

Figure 8 shows the values of the parameters in iterations during the training process. X axis represents the number of iterations and Y axis represents the values of the parameters. During the analysis period, some conditions are defined that determine when the training process ends. In this study, the target values of iteration value 1000, *gradient* value 1×10^{-07} , *mu* value 1×10^{10} , *gamk* value 0 and Sum Squared Param (*ssX*) value 0 are the target values and the training process is terminated if any of the above conditions are met. The training process lasted 1 minute and 31 seconds and the training process was terminated because it reached 1000 iterations. In the finalized process, the *gradient* was 7.3295, *mu* 0.5, *gamk* 373.2331, *ssX* 1284.5032. Since the training process is done with the Bayesian Regularization method, there is no validation data and it shows zero values.

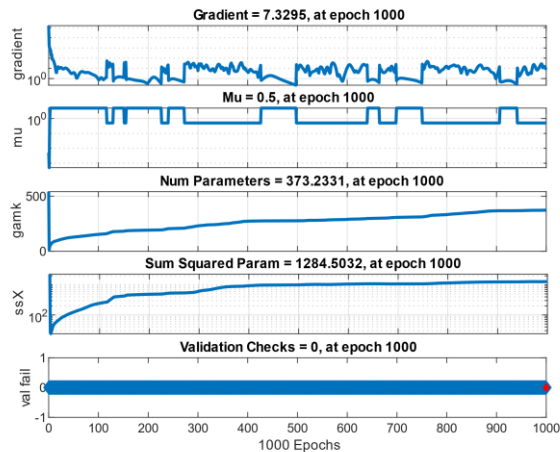


Fig.8. Parameter values in the training process

Figure 9 shows the error histogram showing the cumulative changes of the training and test errors. The vertical line in the graph shows the error at zero points. The majority of the errors are close to this vertical line, which means that the prediction values are consistent with the actual values.

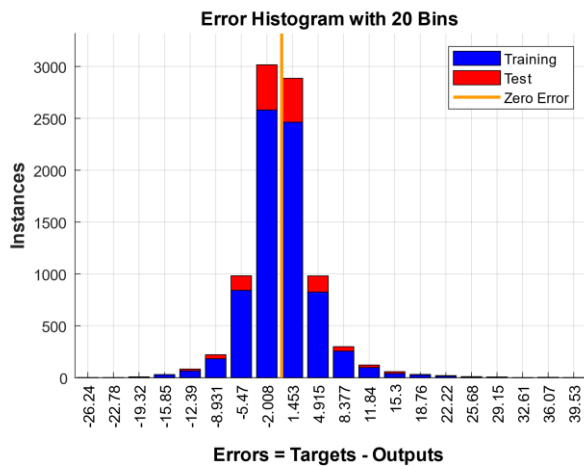


Fig.9. Error histogram at the end of the training process

The regression graphs of the training and test data between the input variables of actual pressure, relative humidity, temperature, and wind direction, and the target variable of wind

speed are given in Figure 10. In these scatter plots, the solid lines represent the linear regression fits for the training and test datasets, while the R-values indicate the strength of the linear relationships between the predicted and actual wind speed values. The training data ($R = 0.78993$) demonstrates a strong correlation, suggesting that the model has learned the relationship between the input variables and wind speed quite effectively. The test data ($R = 0.7457$) also exhibits a strong correlation, although slightly weaker than the training data, indicating that the model performs consistently on unseen data. The "All" graph shows the combined performance ($R = 0.78274$), reinforcing the model's overall reliability in predicting wind speed based on the given meteorological factors.

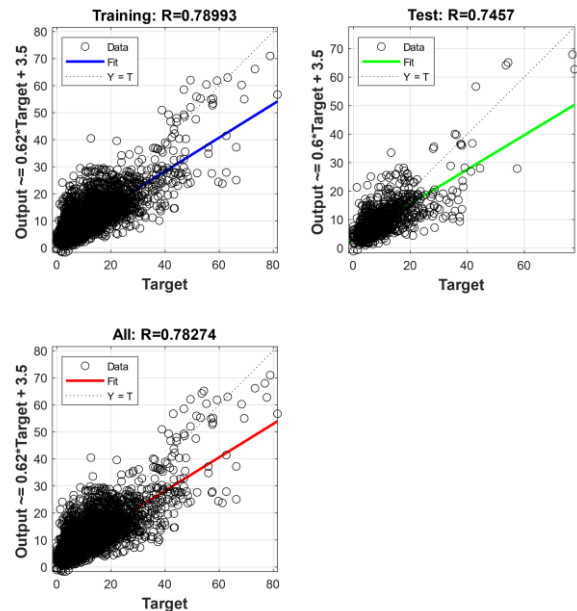


Fig.10. Regression plots for training, test and all data

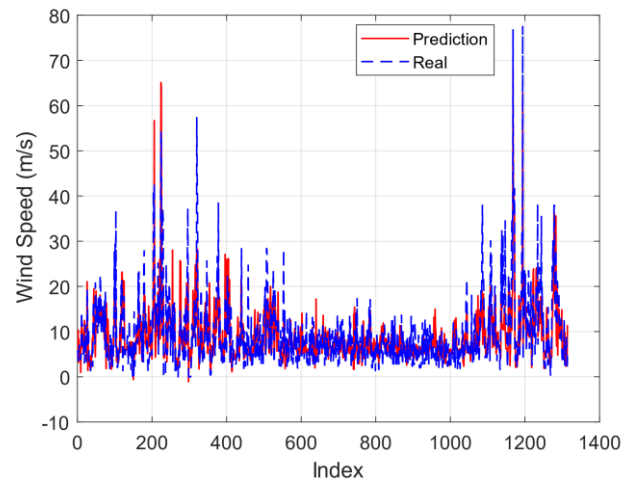


Fig.11. Comparison of test data with prediction values

Figure 11 shows the actual and predicted values of the test data. The red line represents the model's predicted wind speed, while the blue dashed line shows the actual wind speed values over the same period. The close alignment between the

predicted and actual values suggests that the model captures the underlying patterns in the data well. Notable deviations, such as the peaks and troughs, occur in specific intervals, highlighting the challenges of accurately predicting extreme wind speed values. However, the overall trend suggests that the model is effective in tracking wind speed behavior, particularly in moderate conditions. The performance metric values between actual and predicted values for training and test data are given in Table 2.

TABLE II
PERFORMANCE METRIC VALUES FOR TRAINING AND TEST DATA

	Count	MSE	RMSE	MAE	R
Training	7446	21.2192	4.6064	3.1552	0.7899
Test	1314	26.7137	5.1685	3.5055	0.7457

When compared to other studies in the literature, our model's performance metrics, particularly the RMSE and R values, are within an acceptable range for wind speed forecasting in complex terrains. For instance, studies conducted in Bozcaada [14] and Istanbul Avcılar [15] report R values of 0.63 and 0.98, respectively, with varying levels of accuracy based on geographical and climatic conditions. In our case, the R value of 0.7457 for the test data, combined with an RMSE of 5.1685, suggests that the ANN model performs well for the highland conditions of the Kümbet Plateau. This further reinforces the viability of wind energy in this region, where wind speeds are higher compared to coastal areas.

Given these results and the favorable wind conditions in the Kümbet Plateau, the installation of wind power plants in this region is supported. The relatively high wind speeds, along with the model's demonstrated accuracy in predicting wind behavior, make the region a strong candidate for wind energy generation, contributing to the region's energy sustainability.

IV. CONCLUSION

In this study, the average wind speed values in the Kümbet Plateau region of Giresun province were estimated using hourly meteorological data for 2023. Meteorological data consist of five different parameters: actual pressure, relative humidity, temperature, wind direction and average wind speed. In the first stage; the values of the parameters were moved 200 m upwards and the missing data were completed by linear interpolation method.

In the other stage, the model was created and prediction process was carried out by using ANN. Mean wind speed values were predicted by using actual pressure, relative humidity, temperature and wind direction values and performance evaluation was performed by calculating MSE, RMSE, MAE and R values. **MSE**, **RMSE**, **MAE** and **R** values were found to be 21.2192, 4.6064, 3.1552 and 0.7899, respectively, for 7446 training data and 26.7137, 5.1685, 3.5055 and 0.7457, respectively, for 1314 test data. These performance metrics indicate that the model provides a reliable prediction of wind speed based on meteorological variables, with minor deviations between the predicted and actual values. In the light of the findings in Table 2, it is seen that there is no significant difference between meteorological values and predicted values. Therefore, it is predicted that the predicted results can be used

instead of the actual values. The benefits of this study include the ability to forecast wind speed in regions with limited meteorological stations or incomplete data, allowing for better planning in areas such as renewable energy, agriculture, and construction

In future studies, a comprehensive study can be conducted by including various signal decomposition methods, machine learning and deep learning methods. This would further improve prediction accuracy and model generalization, broadening its applicability across different meteorological datasets and regions.

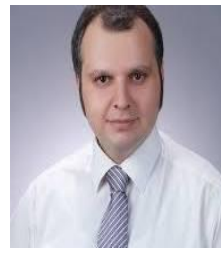
ACKNOWLEDGMENT

This study is supported by Giresun University as a Scientific Research Project numbered FEN-BAP-A-290224-34.

REFERENCES

- [1] Global Wind Energy Council, "Global wind statistics," 2024. [Online]. Available: <https://gwec.net/global-wind-report-2024/>
- [2] Wisevoter. "Wind Power by Country." <https://wisevoter.com/country-rankings/wind-power-by-country/#turkey> (accessed 27.06.2024).
- [3] TEİAŞ, "2023 Kasım Ayı Kurulu Güç Raporu," 2023.
- [4] REPA. "Türkiye Rüzgar Enerjisi Potansiyeli." <https://repa.enerji.gov.tr/REPA/> (accessed 27.06.2024).
- [5] E. Atlası. "Rüzgar Enerji Santralleri." <https://www.enerjiatlası.com/ruzgar/> (accessed 27.06.2024).
- [6] C. Sun, Z. Bie, M. Xie, and J. Jiang, "Assessing wind curtailment under different wind capacity considering the possibilistic uncertainty of wind resources," *Electric Power Systems Research*, vol. 132, pp. 39-46, 2016/03/01/ 2016, doi: <https://doi.org/10.1016/j.epsr.2015.10.028>.
- [7] G.-l. Luo, Y.-l. Li, W.-j. Tang, and X. Wei, "Wind curtailment of China's wind power operation: Evolution, causes and solutions," *Renewable and Sustainable Energy Reviews*, vol. 53, pp. 1190-1201, 2016/01/01/ 2016, doi: <https://doi.org/10.1016/j.rser.2015.09.075>.
- [8] O. Akar, Ü. K. Terzi, B. K. Tunçalp, and T. Sönmezocak, "Determination of the optimum Hybrid renewable power system: a case study of Istanbul Gedik University Gedik Vocational School," *Balkan Journal of Electrical and Computer Engineering*, vol. 7, no. 4, pp. 456-463, 2019.
- [9] W. Zhang, L. Zhang, J. Wang, and X. Niu, "Hybrid system based on a multi-objective optimization and kernel approximation for multi-scale wind speed forecasting," *Applied Energy*, vol. 277, p. 115561, 2020/11/01/ 2020, doi: <https://doi.org/10.1016/j.apenergy.2020.115561>.
- [10] Ş. Fidan, "Wind Energy Forecasting Based on Grammatical Evolution," *European Journal of Technique (EJT)*, vol. 14, no. 1, pp. 23-30.
- [11] A. Costa, A. Crespo, J. Navarro, G. Lizcano, H. Madsen, and E. Feitosa, "A review on the young history of the wind power short-term prediction," *Renewable and Sustainable Energy Reviews*, vol. 12, no. 6, pp. 1725-1744, 2008.
- [12] M. Şen and M. Özcan, "Maximum wind speed forecasting using historical data and artificial neural networks modeling," *International Journal of Energy Applications and Technologies*, vol. 8, no. 1, pp. 6-11, 2021.
- [13] İ. Kırbaş, "İstatistiksel metotlar ve yapay sinir ağları kullanarak kısa dönem çok adımlı rüzgâr hızı tahmini," *Sakarya University Journal of Science*, vol. 22, no. 1, pp. 24-38, 2018.
- [14] A. Demirtop and A. H. Işık, "Yapay Sinir Ağları ile Rüzgâr Enerji Verimliliğine Yönelik Yeni Bir Tahmin Yaklaşımı: Çanakkale ili Bozcaada Örneği," *Uluslararası Mühendislik Tasarım ve Teknoloji Dergisi*, vol. 5, no. 1-2, pp. 25-32, 2023.
- [15] H. Calık, N. Ak, and I. Guney, "Artificial NARX Neural Network Model of Wind Speed: Case of Istanbul-Avcılar," *Journal of*

- Electrical Engineering & Technology*, vol. 16, no. 5, pp. 2553-2560, 2021/09/01 2021, doi: 10.1007/s42835-021-00763-z.
- [16] C. Emeksiz and M. Tan, "Geliştirilmiş EEMD-EWT Tabanlı Yapay Sinir Ağı Modeli Kullanarak Çok Adımlı Rüzgar Hızı Tahmini," *Avrupa Bilim ve Teknoloji Dergisi*, no. 26, pp. 165-173, 2021.
- [17] M. R. Minaz, "Bilecik ilinin uyarlanabilir sinir bulanık çıkarım sistemi ile basınç, sıcaklık ve rüzgar hızı tahmini," Bilecik Üniversitesi, Fen Bilimleri Enstitüsü, 2011.
- [18] E. Dikmen and F. K. Örgen, "AĞLASUN BÖLGESİ İÇİN RÜZGÂR HIZI TAHMİNİ VE EN UYGUN TÜRBİN TESPİTİ," *Niğde Ömer Halisdemir Üniversitesi Mühendislik Bilimleri Dergisi*, vol. 7, no. 2, pp. 871-879, 2018.
- [19] Z. N. Kiriş, Ö. F. Beyca, and F. Kosanoğlu, "Tekrarlayan Sinir Ağları Temelli Rüzgâr Hızı Tahmin Modelleri: Yalova Bölgesinde Bir Uygulama," *Journal of Intelligent Systems: Theory and Applications*, vol. 5, no. 2, pp. 178-188, 2022.
- [20] P. Gipe, "Wind power," *Wind Engineering*, vol. 28, no. 5, pp. 629-631, 2004.
- [21] J. Zou, Y. Han, and S.-S. So, "Overview of artificial neural networks," *Artificial neural networks: methods and applications*, pp. 14-22, 2009.
- [22] B. Yegnanarayana, *Artificial neural networks*. PHI Learning Pvt. Ltd., 2009.
- [23] K. L. Priddy and P. E. Keller, *Artificial neural networks: an introduction*. SPIE press, 2005.
- [24] D. Graupe, *Principles of artificial neural networks*. World Scientific, 2013.
- [25] N. Karayiannis and A. N. Venetsanopoulos, *Artificial neural networks: learning algorithms, performance evaluation, and applications*. Springer Science & Business Media, 2013.



Mehmet Cem Dikbaş was born in 1976. He received B.Sc, M.Sc, and Ph.D. degrees at Yıldız Technical University, Electronics and Communication Engineering Department in 2000, 2004, and 2022 respectively. His research interests are, analog and digital integrated circuit design, active filters, current mode circuit design, artificial intelligence and artificial neural networks. He had worked as research assistant at Yıldız Technical University, Computer Engineering Department from 2003 to 2009. Currently, he is an Assistant Professor at Electric-Electronics Engineering Department at Giresun University.

BIOGRAPHIES



Ferdi Özbilgin was born in Tokat, Türkiye. He received the B.Sc. degree in electrical and electronics engineering from Sivas Cumhuriyet University, Sivas, Turkey, in 2014, and the M.Sc. and Ph.D. degrees in electrical and electronics engineering from Ondokuz Mayıs University, Samsun, Turkey in 2019 and 2023. He has been an Assistant Professor at Giresun University, Giresun, Türkiye. His research interests include biomedical image processing, signal processing and machine learning.



Hüseyin Çalık was born in Giresun, Türkiye in 1967. He received the B.Sc, M.Sc. and degrees in Electrical Engineer from Marmara University, Turkey, in 1999 and 2005. He worked as an Ass. Professor and head of Electric Programme in Vocational School of Technology in Istanbul University Cerrahpasa. He is currently professor, Giresun University, Department of Electrical-Electronics Engineering, Giresun/Türkiye. His research interests are in the areas of industrial automation systems, computer aided design, control of electrical machines, adjustable-speed drives, fuzzy logic and neural network applications

Grid Integration Strategies for Optimizing Renewable Energy Deployment and Grid Resilience

Ercan Aykut* and Ihsan Alshuraida

Abstract— This study explores the integration of renewable energy sources, namely, solar and wind, focusing on strategies to optimize their deployment into the electrical grid, and increasing the resiliency of the grid. Using four-year comprehensive data from Spain, including energy consumption, generation, pricing, and the condition of the weather, advanced statistical analysis, regression models, and optimization methods have been employed. Based on the results, it is clear that solar energy is seasonal, and wind energy is variable, with the weather playing a considerable role in the energy output. The optimization analysis showed that when the renewable capacity was increased to include 30 MW of solar and 120 MW of wind, the energy demand would be met at a significantly lower total system cost of \$12,60 per unit. The costs related to operation and emissions would also decrease notably. However, with the regression models giving modest values of R^2 equal to 0,19 for solar and R^2 equal to 0,21 for wind, the extent of these developments and prediction can be fairly modest.

Index Terms— Renewable Energy Integration, Grid Resilience, Energy Forecasting, Optimization Strategies, Sustainable Energy Infrastructure.

I. INTRODUCTION

THE GLOBAL energy sector faces a critical period caused by the increasing environmental concerns and the imperative for sustainability [1]. Fossil fuels were an engine of economic growth throughout history, playing a significant role in the generation of greenhouse gas emissions this driving global climate change [2], [3]. In the modern age, innovative energy solutions, primarily renewables such as wind and solar become viable to a point of necessity to have an essential grid integration system in place [4]. With the rapid increase in the demand for cleaner energy sources, the transition to renewable energy becomes an environmental imperative and a

technological and economic opportunity to alter the global energy systems of the future [5], [6].


The main challenge of the transition towards a more sustainable power system is the multitude of legal, financial, and technological issues that need to be addressed [7], [8]. Notably, there is a significant challenge of integrating a wide range of renewable energy sources into existing grids, which were constructed to be centralized and more predictable in the scope of power generation [9]. This issue arises because the renewable sources like wind and solar are highly intermittent, introducing variability into the grid, which can make the system less stable and reliable. The integration would require advanced forecasting, advanced methods of optimization as well as sophisticated grid management practices [10].

As modern energy research posits, the cities, and urban areas can decrease their carbon emissions and lower their negative environmental impact through renewable energy grid integration [11]. Additionally, the approach must provide a more detailed understanding of the financial and economic implications of the transition. Now, the policymakers and researchers investigate the economic benefits of reducing reliance on fossil fuels and the environmental benefit of generating fewer greenhouse gas emissions [12]. Such an approach leads to optimal policies that address the environmental issues of the modern age.


Thus, this research aims to analyze renewable energy deployment optimization and grid resilience enhancement through advanced grid integration approaches. The research is multi-disciplinary, utilizing both optimization and computer simulation to ascertain which approach to distributing renewable energy within the grid is the most efficacious. The research will analyze various grid integration methods from the technical, economic, and environmental points of view and will contribute to enhanced grid reliability and resilience. The results will also be used to improve field practices and policies and will hopefully facilitate the transition to a sustainable power system.

Many things have been researched on the integration of renewable energy into power grids [13]. Over the past few decades, the integration of renewable energy sources in power grid has been a topic of research in the energy field. The world today is under pressure of climate change, and the reduction of fossil fuels. The world is now in urgent need of sustainability. Many researchers have already tried to find the feasibility of

Ercan AYKUT, is with Department of Electrical Electronics Engineering Istanbul Gelisim University, Istanbul, Turkey, (e-mail: eykut@gelisim.edu.tr).

 <https://orcid.org/0000-0001-8639-8408>

Ihsan ALSHURIDA, is with Department of Electrical Electronics Engineering Istanbul Gelisim University, Istanbul, Turkey (e-mail: ihsanalshuraida1990@gmail.com).

 <https://orcid.org/0009-0006-6746-1110>

Manuscript received Aug 07, 2024; accepted Sep 23, 2024.

DOI: [10.17694/bajece.1529149](https://doi.org/10.17694/bajece.1529149)

solar and wind energy in replacing conventional energy sources [14]. The researchers confirmed that these two sources of energy have environmental sustainability and economically feasible. However, these energy sources tend to have an unstable nature, and they can be a big problem for the grid. The research utilized advanced forecasting solutions for output prediction and optimization of renewable energy generation and supply [15], [16], [17].

The first problem with the renewable energy source is that they are not stable and predictable. The generation and supply of energy to the grid are also variable and not predictable. The more instability and variation in the networks leading to imbalance energy supply and demand [18]. Many studies have already tried to come up with solutions by coming up with advanced forecasting techniques which will predict the output of renewable energy more accurately and improve the reliability of the grids [19], [20]. For instance, Xie et al. [21] developed models of predict and energy using atmospheric variables for short-term prediction. The model uses machine learning techniques and data of present and past weather to predict the energy. These advanced forecasting solutions are important in the optimization of renewable energy and hence reduce the use of power-reliable bases such as fossil fuels.

In the available literature on renewable energy integration, grid modernization is also identified to be a critical focus area [22]. Given that traditional grids were designed for centralized power generation this approach often lacks the needed flexibility to respond to the intermittent nature of renewable energy sources. A number of scholars emphasize that it is necessary to focus on upgrading grid infrastructures, scaling the implementation of smart grid technologies, and promoting the efficiency of energy storage solutions to improve grid flexibility and resilience. For example, modern grids can be characterized by smart meters, sensors, and other devices for real-time monitoring and management of energy flow, which enables better integration of distributed renewable energy sources and improved overall grid stability [23]. In addition, a number of renewable energy integration problems could be solved by optimization techniques [24].

According to the available literature, the complexity of decision-making in renewable energy integration gives an opportunity to apply various optimization models developed based on linear programming, mixed-integer programming, and stochastic optimization [25]. The primary goal of these models is to find the best balance between energy demand and supply while also minimizing overall operation costs and associated emissions. As such, mathematical models can account for energy production forecasts, the capacity of energy storage devices, and existing grid constraints to identify the best energy mix and operational strategies [26]. Finally, multiple scholarly articles investigate the opportunities for multi-objective optimization, which helps achieve economic, environmental, and technical objectives simultaneously and, therefore, be adopted as a single approach to grid management and renewable energy deployment [27], [28], [29].

Furthermore, the literature also highlights the significant role of policy and regulatory frameworks in enabling the integration

of renewable energy into the grid. On the one hand, effective policy instruments can stimulate the deployment of renewable energy technologies, facilitate grid upgrades, and boost investment in research and development [30]. Regulatory measures, such as feed-in tariffs and renewable energy certificates, are significantly successful in this regard, since provide all essential incentives and reduce relevant market barriers. On the other hand, it is important to recognize that international policy interaction and knowledge sharing are critical to address the global nature of modern renewable energy integration challenges and overcome them on the way to becoming a sustainable energy system [31].

Overall, the literature on the topic of renewable energy integration is an essential resource for those who wish to gain a comprehensive picture of these phenomena. Being thoroughly examined and studied from the most different angles, it highlights a complex, multi-faceted nature of the pivotal role of renewables for world energy. It also shows that this role can only be successfully embraced provided technologic, economic, and policy efforts are closely interconnected and enable comprehensive actions toward a complete energy transition.

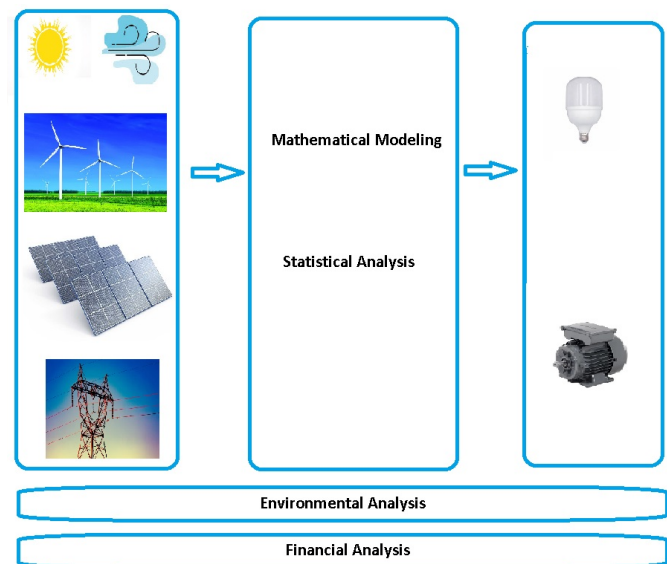


Fig1. Renewable energy system with grid resilience

II. MATERIAL AND METHODS

The methodology for the study adopted a comprehensive research procedure that investigates and optimizes the integration of renewable energy sources within the electrical grid sphere. For instance, it structures the systematic process through which data was collected, the analytical and modeling techniques employed, as well as the optimization methods and scenario analysis. Moreover, by taking a multidiscipline approach, the study is able to minimize the complex challenges of renewable energy variability and the issue of grid resilience. The subsections provide a level of detailed analysis of the processes involved in each approach undertaken. This includes a specialized study of what was done to ensure data accuracy, and the specifics of how predictive models were developed and optimized. This ensures that the best optimization strategies are

utilized as well as a thorough examination of various scenarios. Overall, the methodology plays a vital role in providing the best set of procedures to meet the objective of achieving a sustainable and efficient energy system. Figure 1 shows the schematically representation of hybrid wind solar and grid energy system and the resilience according to the weather conditions.

A. Data Collection and Preparation

The data collection process for this study has been carefully designed to ensure that all relevant variables that affect the inclusion of renewable energy sources in the production of power to the grid were included. The data was collated from a number of authoritative sources – for instance, ENTSOE (European Network of Transmission System Operators for Electricity) has provided records of power consumption and generation in Spain, while REE (Red Eléctrica de España) as the national operator of transmission service has provided a variety of information, including settlement price and operation on the grid. The data on weather was also obtained from relevant sources, such as the Open Weather API. A number of variables – temperature, wind speed, humidity, and cloudiness – had been available for five biggest cities in Spain and had been updated every hour. This arrangement had provided a sufficient basis to analyze the relationship between weather and power generation, supply, and consumption in the country.

In order to prepare the available data for processing, a number of steps to pre-process it had to be taken. The preprocessing effort, however, had begun with the data clean-up, which involved addressing missing values, inconsistencies, and formatting issues. For example, the columns that were missing a substantial number of entries – for instance, the added generation or forecasted wind offshore – had been removed to ensure the reliability of the dataset. The time columns had next been converted to date, time, and the time period that was the same in every dataset was synchronized to facilitate time-series analysis. The gaps in the data had been filled with a variety of interpolate methods, the choice of which also allowed us to keep the data in chronological order and provide continuity – an important prerequisite of rigorous modeling.

During further preparation, the data had been normalized to ensure that the varying scales of measurement do not distort its relation to other datasets. The weather data was matched with the energy and consumption data by timestamp, with energy data corresponding to the weather data on the same time. The matching was important since weather was a crucial variable in the modeling effort and had to correspond to the same time during which the energy was measured. Furthermore, alongside outlier detection and removal to prevent rare and unusual spikes unduly affecting the models, such a matching also allowed to remove or address the data entry occasionally not matching the rest of the values. Such a data preparation effort had laid a significant groundwork for the subsequent analytical and modeling stages, ensuring that the models were operating upon the most relevant and accurate data.

B. Analytical and Modeling Techniques

The analytical approach utilized in this study consists of various statistical analysis and machine learning techniques that

together help to disentangle the complexities of renewable energy integration and determine the optimal performance of the grid. First of all, to characterize the data and get general insights into the data and key statistical features, descriptive statistical methods were employed. These methods helped to understand the degree of data central tendencies, dispersion, and distribution. In this part of the analysis, various variables were considered, including solar and wind generation, temperature, wind speed, and others. This preliminary analysis allowed formulating hypotheses related to the data behaviors and detect significant patterns and anomalies that needed further consideration.

After the preliminary data analysis was performed, the regression analysis was employed to determine the scope of relationships between the weather variables and renewable energy output. Two linear regression models were developed to predict the solar and wind energy generation based on a combination of meteorological data like temperature, cloud cover, humidity, wind speed, and others. The regression models developed were assessed based on such metrics as Mean Absolute Error (MAE), Mean Squared Error (MSE), and R-squared value (R^2). The regression models provide important tools to quantitatively characterize how weather fluctuation affects the production of renewable energy. MAE shows the variation between the actual value and predicted value can be calculated as in (Eq.1) [32].

$$MAE = \frac{1}{n} \sum_{i=1}^n (Y_i - X_i) \quad (1)$$

MSE is another indicator also showing the correlation between the original data and the predicted data which is shown by (Eq.2) [33].

$$MSE = \frac{1}{n} \sum_{i=1}^n (Y_i - X_i)^2 \quad (2)$$

To solve the problem associated with the enhancement of the energy mix and the optimization of system performance, various optimization techniques were employed. A critical component of this part of the analysis was the development of linear programming and mixed-integer programming models. Several mathematical models were developed to optimize the energy mix in order to minimize costs, emissions, and maximize grid performance. The linear programming and mixed programming models specified energy supply, demand, and storage and addressed the constraints associated with the capacity and demand for generation and storage of energy. In addition to that, different scenarios were developed to consider the worst and best-case scenarios for energy mix. These scenarios included cases related to changes in renewable energy penetration and severe weather conditions. Overall, the models used in this study offered tools for a comprehensive strategy that could contribute to the effective integration of renewable energy into the grid.

The findings of the study helped to determine a strategy that could be utilized to optimize the performance of the developed model. However, the model used to optimize grid performance and develop an energy mix could have some limitations. First of all, it is critical to consider the data variability in planning the operations related to the detection of different trends and

anomalies. In this case, the data from the previous five years were not utilized to analyze the variability of the data in a long-term perspective. In the future, it could be implemented in a similar analysis to align the results with the data variability structure and get a comprehensive understanding of the data trends. Secondly, it is important to consider that the factors that impact climate change and the structure of data and weather variables can be manifold. Thirdly, the optimization models considered a rather simplified structure of constraints that can be impacted by other factors that should be considered in planning operations. Overall, the models utilized in this study offer an effective approach and a suitable tool for further development and optimization.

C. Optimization and Scenario Analysis

The optimization phase of the current study research was dedicated to the development of models that could be used for the definition of the most efficient strategies for incorporating renewable energy sources in the grid. Specifically, the goal was to ensure that the supply of energy would meet the demand as closely as possible while minimizing the cost of operation and carbon emissions. Linear programming and mixed-integer linear programming were used for the formulation of the optimization problems. The models included decision variables reflecting the level of generation of solar and wind energy and of storage or discharge from the storage systems. The goal function aimed at minimizing costs relating to energy generation as well as gaining and storage while meeting the limits and demands. Scenario analysis was conducted based on the variety of scenarios aimed at capturing the alterations in the use of renewable energy as such, the weather, and the demand. Specifically, based on the simulation, the current study included the scenarios reflecting the base, moderate, and high increases in the use of solar and wind energy and the scenarios of the extensive cloudy days or days with no wind.

The optimization models resulted in the valuable insights into the optimal approaches to incorporate renewable energy within the grid. Specifically, the analysis of the optimized grid systems revealed the optimal mixes that included the use of both generated solar and wind energy and the rest that was put in storage with no exceeding limits of the latter. The use of the optimization data in combination with the scenario analysis demonstrated the immense value of the increased use of renewable energy considering the potential savings for the baseline scenarios and the emissions. For the weather scenarios, the relevant implications concerning the development of the grid were as follows: the increased use of renewable energy sources is beneficial in extreme weather conditions as long as there is less or no sunlight and wind with the latter to be less stable than the former; the daily rise of the energy demand up to 60% will require dynamic storage systems; the constant energy demand should be met by monitoring the demand and pulling heavier during the days with inadequate generation.

III. APPLICATION

The analytical findings of the study were based on different types of approaches, discussing peculiar aspects of the energy environment. The bell-shaped curve that depicts the temperature distribution of the dataset is seen in Figure 2. This

curve is indicative of a normal distribution as it is bell-shaped. Temperature data is an essential variable for the subsequent analysis because it has a significant impact on energy output, especially solar energy. This visualization was important in checking whether the data was genuine.

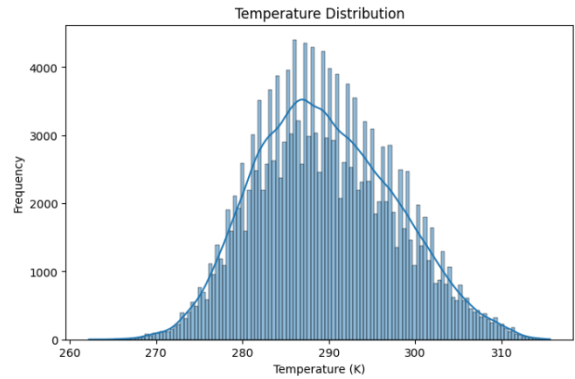


Fig2. Temperature Distribution

The correlation analysis demonstrated that temperature and solar generation were linked by the sufficiently favorable relationship while the minor negative correlation was established between wind generation and these two parameters. The heat map of the correlation analysis is presented in Figure 3. These findings not only provided more information on the impact of weather on the dynamics of energy but also indicated the nature of the relationship between the renewal forms of power and the natural environment. In the framework of the exercise, optimization needs to be emphasized, and even if the process was rather theoretical or abstract, it produced the basis for costs and emissions minimization. The latter was supposed to be reached with the help of a more profound consumption of solar and wind energy, with the help of which the grid would be driven into a more sustainable and secure future.

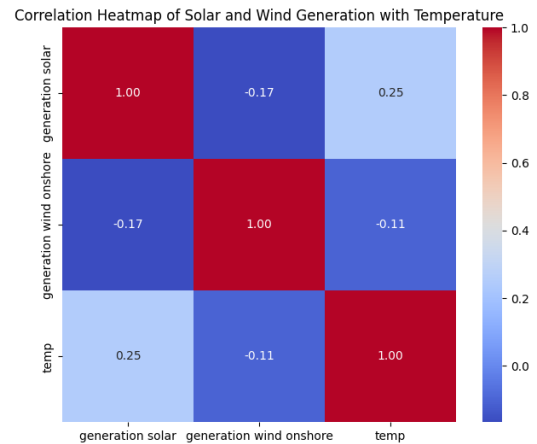


Fig3. Correlation Heat map of Solar and Wind Generation with Temperature

The time series graphs for solar and wind power generation illustrated that these alternatives to the more conventional forms of energy are all cyclical. The solar power generation over time, as seen in Figure 4, had what were quite obvious peaks or high points at certain hours of the day when it is expected because of the day light.

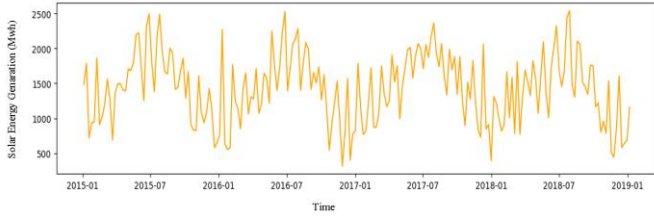


Fig4. Solar Generation Over Time

The presented data in Figure 5 indicated that the wind generation was significantly more variable than anticipated. This is correctly depicted, because in reality wind speeds and patterns are significantly less predictable.

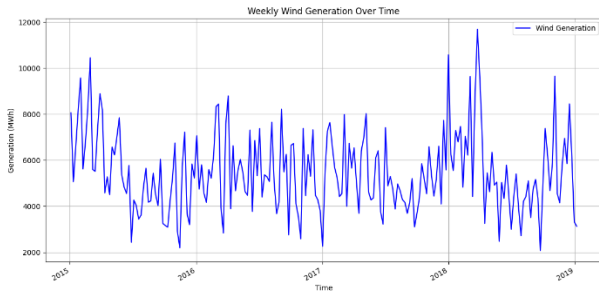


Fig5. Weekly Wind Generation Over Time

Figure 6 illustrates the energy mix that can meet the energy demand at a total cost of \$12,60. The combination maximizes the utilization of renewable energy sources, resulting in a reduction of costs. To come up with the solution, 30MW of the solar plant and 120 MW of the wind plant have been added.

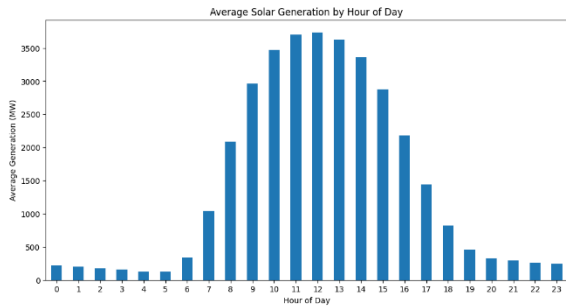


Fig6. Optimal Energy Mix Visualization

Moreover, the results of the regression analysis can allow people to better understand the exact relationships that exist between climate and the electricity generation. As per the Figure 7 and Figure 8, the coefficients of determination of both the solar and wind model were 0,08, and the mean squared errors produced from the models above equate to 25.68143,77 and 945.7315,25 respectively. Thus, the results imply that the generated models can only predict a meager percentage of the generation produced. However, they also offer a simplistic mathematical model that can be employed to forecast generation using weather data.

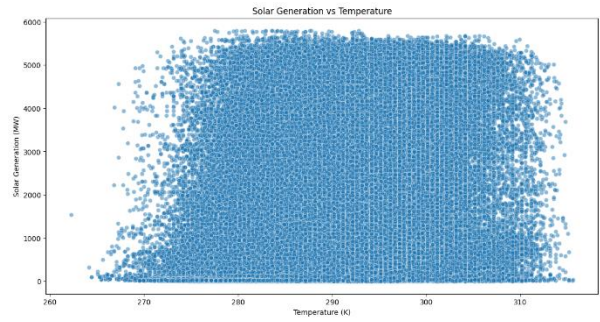


Fig7. Scatter Plot of Solar Generation vs. Temperature

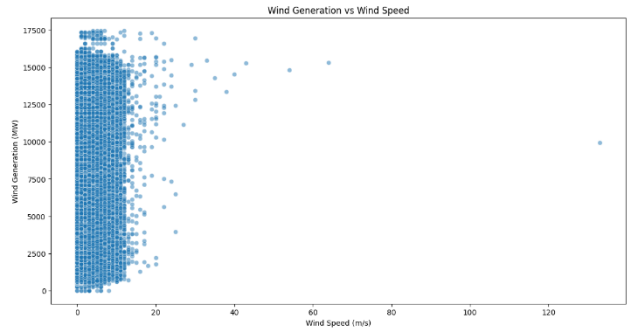


Fig8 Scatter Plot of Wind Generation vs. Wind Speed

The regression models, in their turn, are of more statistical views, and hence, lay the major ground for describing and forecasting the future generation of energy. As these models are developed to forecast dichotomous outcomes, the models of solar kinetics and wind generation need to be involved with several meteorological variables as predictors. Consequently, the weather and environment turn to be major interventions on the renewable energy outcomes, depicting the hopes and opportunities of modelling for further grid optimization. Besides, there is the correlation analysis or regression models, depicting even more statistically evident approaches to the relationships between the weather and energy. In comparison with the correlation analysis, the regression models have presented the same findings concerning the presence of a positive correlation between temperature and solar generation in the up-mentioned correlation heat map: in most incidents the higher the temperature, the higher the solar generation. On the other hand, for wind generation, the negative correlation was seen, as the higher was the temperature, the lower would be the wind generation.

The chart in Figure 9 shows how the cost and expenditure change for both systems. The second chart shows that the CO2 emissions are decreased for each system. The third chart shows the increase in energy generated when the solar capacity is increased to moderate and high levels. All these systems changes are indicated by the produced amount of system capacity by atmospheric conditions. The depicted implication can be brought to light by a rise in the capacity of solar production.

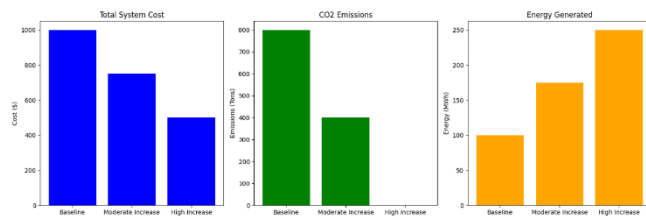


Fig9. Impact of Increased Solar Capacity on Grid Economics and Sustainability

IV. EVALUATION

Given the substantial difficulties and opportunities related to the implementation of renewable energy sources into the existing electrical grids revealed by a profound study of the solar and wind power generation based on the substantial environmental variations, it is pivotal to consider the multiple facets of grid integration and the implications that the present study has for the sustainability and vulnerability of the future grids.

The Solar Generation Model had an R^2 value of 0,19 and an MAE of about 1163,14 MW in terms of the model's predictability. For this reason, the model, though maybe not too accurate, does account for some of the variations observed in the data. Furthermore, the Wind Generation Model also has a similar prediction capacity – further tuning can allow it to make more accurate estimates of the wind energy that can be generated. The model has a 2191,01MW EAM and an R^2 value of 0,21.

The outcomes describe the complex relationships between the renewable energy sources and their environmental generation, illustrating the necessity of better forecasting for grid approaches. Moreover, the outcomes of the optimization analysis emphasize the opportunities for savings or reducing emissions. The figure plots for the wind and solar generation for a total cost of 12.6 dollars per unit of energy generated demonstrate that the optimal solar and wind capacities should have been increased by 30 and 120 units, respectively, to minimize costs and maximize generation (Figure 6). The regression analysis presents the outcomes of the developed models (Figures 7 and 8). The obtained R-squared values are relatively modest, as the necessity of a simple model and minimum predictors was needed. Thus, for the Solar Generation Model, this R-squared is 0,19, for the Wind Generation Model – 0,21. The MAEs are about 1163,14 MW and 2191,01 MW, respectively.

For Spain, the scenario analysis reveals the considerable benefits of increasing the capacity of renewable energy. The first scenario, representing current situation, shows the highest system cost of almost \$13.000 and highest CO2 emissions nearing 20.000 tons with energy generation around 2.500 MWh. In comparison, moderate increase scenario, where capacity of solar and wind energy is increased by 50 MW each, sees cost reduced to about \$8.000, emissions to 12.000 tons, and energy generation grow to 4.000 MWh. Finally, in high increase scenario, where capacity increases by 100 MW, cost are reduced to about \$2.000, emissions to 3.000 tons, and energy generation is at 5.500 MWh. Overall, the results show

that increasing capacity of renewable energy would provide benefit in both economic and environmental ways, seeing costs being cut in half, emissions reduced by up to almost 85% and improved energy production capabilities. The comparative analysis of renewable energy scenarios is shown in Figure 10.

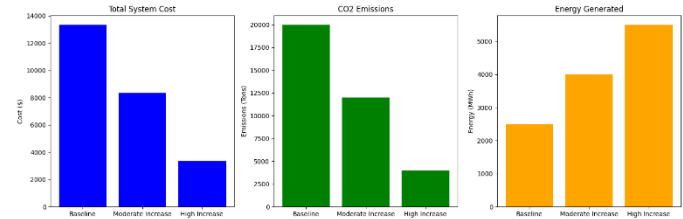


Fig10. Comparative Analysis of Renewable Energy Scenarios for Spain

V. CONCLUSION

The overall outcomes of the study confirm the feasibility of solar and wind renewable energy sources within and connected to the grid. The scenario analysis has shown, that the greater number of solar capacity increases the effectiveness and economic and sustainability outcomes of the grid. The MAEs of the developed regression models are modest, and to improve the forecasting options, the present models demand an increasing number of predictors. Finally, blueprints show that the data models do describe the direct diagonal line, telling about the non-statistical manners of generation in both cases. Notwithstanding the modest accuracy of the present models, definite interventions present the greatest opportunities for future forecasting.

This study provides valuable insights into the urgent need for incorporating renewable sources of energy, primarily solar and wind, into the existing electrical grid to enhance sustainability and resilience. Conclusively, it was established that, if the energy demand is met based on the specified combination of solar and wind energy, the total system cost will amount to \$12,60 per unit of energy, which is considerably lower compared to traditional sources of energy. The regression analysis conducted, even though it produced relatively unimpressive outcomes concerning the level of solar coefficients, and the wind one, respectively, sets the foundation for predicting the output of energy based on a given weather condition.

In order to increase the accuracy of the prediction, advanced methods such as machine learning can be used.

REFERENCES

- [1] E. Papadis and G. Tsatsaronis, "Challenges in the decarbonization of the energy sector," *Energy*, vol. 205, p. 118025, Aug. 2020, doi: 10.1016/j.energy.2020.118025.
- [2] G. O. Atedhor, "Greenhouse gases emissions and their reduction strategies: Perspectives of Africa's largest economy," *Scientific African*, vol. 20, p. e01705, Jul. 2023, doi: 10.1016/j.sciaf.2023.e01705.
- [3] O. Akar, Ü. K. Terzi, B. K. Tunçalp, and T. Sönmezocak, "Determination of the Optimum Hybrid Renewable Power System: A case study of Istanbul Gedik University Gedik Vocational School," *Balkan Journal of Electrical and Computer Engineering*, vol. 7, no. 4, pp. 456–463, Oct. 2019, doi: 10.17694/bajece.623632.

- [4] A. T. Hoang, V. V. Pham, and X. P. Nguyen, "Integrating renewable sources into energy system for smart city as a sagacious strategy towards clean and sustainable process," *Journal of Cleaner Production*, vol. 305, p. 127161, Jul. 2021, doi: 10.1016/j.jclepro.2021.127161.
- [5] K. Moustakas, M. Loizidou, M. Rehan, and A. S. Nizami, "A review of recent developments in renewable and sustainable energy systems: Key challenges and future perspective," *Renewable and Sustainable Energy Reviews*, vol. 119, p. 109418, Mar. 2020, doi: 10.1016/j.rser.2019.109418.
- [6] E. Aykut and Ü. K. Terzi, "Techno-economic and environmental analysis of grid connected hybrid wind/photovoltaic/biomass system for Marmara University Goztepe campus," *International Journal of Green Energy*, vol. 17, no. 15, pp. 1036–1043, Dec. 2020, doi: 10.1080/15435075.2020.1821691.
- [7] M. J. B. Kabeyi and O. A. Olanrewaju, "Sustainable Energy Transition for Renewable and Low Carbon Grid Electricity Generation and Supply," *Front. Energy Res.*, vol. 9, p. 743114, Mar. 2022, doi: 10.3389/fenrg.2021.743114.
- [8] O. Çiçek, M. A. M. Millad, and F. Erken, "ENERGY PREDICTION BASED ON MODELLING AND SIMULATION ANALYSIS OF AN ACTUAL GRID-CONNECTED PHOTOVOLTAIC POWER PLANT IN TURKEY," *European Journal of Technic*, Dec. 2019, doi: 10.36222/ejt.593250.
- [9] D. Mahmood, N. Javaid, G. Ahmed, S. Khan, and V. Monteiro, "A review on optimization strategies integrating renewable energy sources focusing uncertainty factor – Paving path to eco-friendly smart cities," *Sustainable Computing: Informatics and Systems*, vol. 30, p. 100559, Jun. 2021, doi: 10.1016/j.suscom.2021.100559.
- [10] D. Yang *et al.*, "A review of solar forecasting, its dependence on atmospheric sciences and implications for grid integration: Towards carbon neutrality," *Renewable and Sustainable Energy Reviews*, vol. 161, p. 112348, Jun. 2022, doi: 10.1016/j.rser.2022.112348.
- [11] Y. Lin, M. K. Anser, M. Y.-P. Peng, and M. Irfan, "Assessment of renewable energy, financial growth and in accomplishing targets of China's cities carbon neutrality," *Renewable Energy*, vol. 205, pp. 1082–1091, Mar. 2023, doi: 10.1016/j.renene.2022.11.026.
- [12] J. Wang and W. Azam, "Natural resource scarcity, fossil fuel energy consumption, and total greenhouse gas emissions in top emitting countries," *Geoscience Frontiers*, vol. 15, no. 2, p. 101757, Mar. 2024, doi: 10.1016/j.gsf.2023.101757.
- [13] Erdiwansyah, Mahidin, H. Husin, Nasaruddin, M. Zaki, and Muhibuddin, "A critical review of the integration of renewable energy sources with various technologies," *Prot Control Mod Power Syst*, vol. 6, no. 1, p. 3, Dec. 2021, doi: 10.1186/s41601-021-00181-3.
- [14] A. Razmjoo, L. Gakenia Kaigutha, M. A. Vaziri Rad, M. Marzband, A. Davarpanah, and M. Denai, "A Technical analysis investigating energy sustainability utilizing reliable renewable energy sources to reduce CO₂ emissions in a high potential area," *Renewable Energy*, vol. 164, pp. 46–57, Feb. 2021, doi: 10.1016/j.renene.2020.09.042.
- [15] S. Aslam, H. Herodotou, S. M. Mohsin, N. Javaid, N. Ashraf, and S. Aslam, "A survey on deep learning methods for power load and renewable energy forecasting in smart microgrids," *Renewable and Sustainable Energy Reviews*, vol. 144, p. 110992, Jul. 2021, doi: 10.1016/j.rser.2021.110992.
- [16] L. Abualigah *et al.*, "Wind, Solar, and Photovoltaic Renewable Energy Systems with and without Energy Storage Optimization: A Survey of Advanced Machine Learning and Deep Learning Techniques," *Energies*, vol. 15, no. 2, p. 578, Jan. 2022, doi: 10.3390/en15020578.
- [17] C. Sweeney, R. J. Bessa, J. Browell, and P. Pinson, "The future of forecasting for renewable energy," *WIREs Energy & Environment*, vol. 9, no. 2, p. e365, Mar. 2020, doi: 10.1002/wene.365.
- [18] "Review of distribution network phase imbalance: Scale, causes, consequences, solutions, and future research direction," *CSEE JPES*, 2020, doi: 10.17775/CSEEJPES.2019.03280.
- [19] D. Rangel-Martinez, K. D. P. Nigam, and L. A. Ricardez-Sandoval, "Machine learning on sustainable energy: A review and outlook on renewable energy systems, catalysis, smart grid and energy storage," *Chemical Engineering Research and Design*, vol. 174, pp. 414–441, Oct. 2021, doi: 10.1016/j.cherd.2021.08.013.
- [20] I. Alotaibi, M. A. Abido, M. Khalid, and A. V. Savkin, "A Comprehensive Review of Recent Advances in Smart Grids: A Sustainable Future with Renewable Energy Resources," *Energies*, vol. 13, no. 23, p. 6269, Nov. 2020, doi: 10.3390/en13236269.
- [21] A. Xie, H. Yang, J. Chen, L. Sheng, and Q. Zhang, "A Short-Term Wind Speed Forecasting Model Based on a Multi-Variable Long Short-Term Memory Network," *Atmosphere*, vol. 12, no. 5, p. 651, May 2021, doi: 10.3390/atmos12050651.
- [22] S. Rahim and P. Siano, "A survey and comparison of leading-edge uncertainty handling methods for power grid modernization," *Expert Systems with Applications*, vol. 204, p. 117590, Oct. 2022, doi: 10.1016/j.eswa.2022.117590.
- [23] I. Diahovchenko, M. Kolcun, Z. Čonka, V. Savkiv, and R. Mykhailyshyn, "Progress and Challenges in Smart Grids: Distributed Generation, Smart Metering, Energy Storage and Smart Loads," *Iran J Sci Technol Trans Electr Eng*, vol. 44, no. 4, pp. 1319–1333, Dec. 2020, doi: 10.1007/s40998-020-00322-8.
- [24] O. A. Al-Shahri *et al.*, "Solar photovoltaic energy optimization methods, challenges and issues: A comprehensive review," *Journal of Cleaner Production*, vol. 284, p. 125465, Feb. 2021, doi: 10.1016/j.jclepro.2020.125465.
- [25] A. Cosic, M. Stadler, M. Mansoor, and M. Zellinger, "Mixed-integer linear programming based optimization strategies for renewable energy communities," *Energy*, vol. 237, p. 121559, Dec. 2021, doi: 10.1016/j.energy.2021.121559.
- [26] J. Bistline *et al.*, "Energy storage in long-term system models: a review of considerations, best practices, and research needs," *Prog. Energy*, vol. 2, no. 3, p. 032001, Jul. 2020, doi: 10.1088/2516-1083/ab9894.
- [27] M. Parvin, H. Yousefi, and Y. Noorollahi, "Techno-economic optimization of a renewable micro grid using multi-objective particle swarm optimization algorithm," *Energy Conversion and Management*, vol. 277, p. 116639, Feb. 2023, doi: 10.1016/j.enconman.2022.116639.
- [28] R. Das *et al.*, "Multi-objective techno-economic-environmental optimisation of electric vehicle for energy services," *Applied Energy*, vol. 257, p. 113965, Jan. 2020, doi: 10.1016/j.apenergy.2019.113965.
- [29] K. Ullah, G. Hafeez, I. Khan, S. Jan, and N. Javaid, "A multi-objective energy optimization in smart grid with high penetration of renewable energy sources," *Applied Energy*, vol. 299, p. 117104, Oct. 2021, doi: 10.1016/j.apenergy.2021.117104.
- [30] J. P. Painuly and N. Wohlgenuth, "Renewable energy technologies: barriers and policy implications," in *Renewable-Energy-Driven Future*, Elsevier, 2021, pp. 539–562. doi: 10.1016/B978-0-12-820539-6.00018-2.
- [31] R. M. Elavarasan *et al.*, "A Comprehensive Review on Renewable Energy Development, Challenges, and Policies of Leading Indian States With an International Perspective," *IEEE Access*, vol. 8, pp. 74432–74457, 2020, doi: 10.1109/ACCESS.2020.2988011.
- [32] A. Demirtop and O. Sevli, "Wind speed prediction using LSTM and ARIMA time series analysis models: A case study of Gelibolu," *Turkish Journal of Engineering*, vol. 8, no. 3, pp. 524–536, Jul. 2024, doi: 10.31127/tuje.1431629.
- [33] M. Madhiarasan, "Accurate prediction of different forecast horizons wind speed using a recursive radial basis function neural network," *Prot Control Mod Power Syst*, vol. 5, no. 1, p. 22, Dec. 2020, doi: 10.1186/s41601-020-00166-8.

BIOGRAPHIES



Ercan AYKUT was born in Istanbul in 1979. He received his B.S. degree from Electrical Education Department of Technical Education Faculty of University of Marmara, Istanbul, in 2002 and his M.Sc. and Ph.D. degree from Electrical Education Department of Institute of Pure and Applied Sciences, University of Marmara, Istanbul, in 2007 and 2019 respectively. He has been an Assistant Professor at Istanbul Gelişim University since 2021. His research interests include renewable energy systems, automation, hybrid energy systems, industrial control and installation systems.



Ihsan Alshuraida was born in 1990 in Basra, Iraq. He received the B.S. degree in electrical power engineering from the Technical University of Basra, in 2013 and received M.S. degree in electrical electronics engineering from Istanbul Gelişim University, in 2024. He works as electrical engineer in energy sector. His research interests include energy systems, energy transmission, renewable energy with grid resilience and machine control.

Research Article

Comparative Analysis of Deep Learning Algorithms in Fire Detection

Remzi Gocmen, Musa Cibuk and Erdal Akin

Abstract—As technology rapidly advances, deep learning applications, a subset of machine learning, are becoming increasingly relevant in various aspects of our lives. Essential daily applications like license plate recognition and optical character recognition are now commonplace. Alongside current technological progress, the development of future-integrated technologies such as suspicious situation detection from security cameras and autonomous vehicles is also accelerating. The success and accuracy of these technologies have reached impressive levels. This study focuses on the early and accurate detection of forest fires before they cause severe damage. Using primarily forest fire images from datasets obtained from Kaggle, various deep learning algorithms were trained via transfer learning using MATLAB. This approach allowed for comparing different deep learning algorithms based on their efficiency and accuracy in detecting forest fires. High success rates, generally exceeding 90%, were achieved.

Index Terms—Fire Detection, Image Processing, Deep Learning, Convolutional Neural Networks, Deep Learning Algorithms

I. INTRODUCTION

FIRE HAS contributed to human development in many areas since its discovery. However, when a fire goes out of control, it can cause serious damage, making preventing loss of life and property critically important [1]. Early detection and intervention can significantly reduce the damage caused by fires. Despite the efforts of fire departments, timely intervention is sometimes hindered by factors such as traffic, delayed notifications, and the fire's location being unsuitable for immediate access. This tragic reality has driven researchers to

develop and improve firefighting systems.

When it comes to forest fires, time constraints are the most significant obstacle, rather than urban factors like traffic or fire location. Forest fires spread rapidly and are often the last type of fire to be noticed. In our region, the frequent late detection and delayed intervention of forest fires are shrinking the green areas daily. This reduction in green spaces, combined with increased greenhouse gas emissions, accelerates global warming, climate change, environmental pollution, drought, and other undesirable negative effects, making our country and the world increasingly uninhabitable.

Today, firefighting units actively use computerized fire detection systems. Nevertheless, effective intervention remains challenging. Considering the physical structure of forest lands and the rapid spread of forest fires, early and accurate detection is essential for timely intervention and preventing major damage. Confirming fire notifications with computer vision and artificial intelligence systems can also prevent false alarms, providing significant benefits.


Point-type thermal and smoke sensors are commonly used, but they are often located close to the fire zone, making them susceptible to malfunction or damage. Advances in computer image processing have introduced video and image-based fire detection methods, which offer fast response times and wide detection areas compared to traditional methods [2]. High sensitivity, accurate and early detection, and prompt alarms are necessary to reduce fire losses. However, traditional fire detection technologies like smoke and heat detectors are unsuitable for large areas, complex buildings, or many disadvantaged areas. Due to these limitations, missed detections, false alarms, and detection delays often occur, complicating early fire warnings [3].

Recently, visual fire detection has become a popular research topic due to its many advantages, such as early detection, high accuracy, flexible system installation, and effective detection in large areas [4]. Deep learning (DL) algorithms analyze image data from cameras to determine the presence of fire or fire risk. Therefore, the detection algorithm is the core of this technology and directly affects the performance of visual fire detectors.


The main objective of this study is to compare Deep Learning (DL) Algorithms, which are essentially Artificial Neural Networks (ANNs), using different datasets, primarily forest fire images, to evaluate their performance. This comparison will enable the assessment of fire detection accuracy, detection speed, and sensitivity of the DL Algorithms used.

In this study, the structure, function, and working principles of Convolutional Neural Networks (CNN) systems were first


Remzi GÖÇMEN, is with Department of Valide Sultan Vocational and Anatolian High School in the Ministry of National Education, Bitlis, Turkey, (e-mail: r.gocmen2012@gmail.com).

 <https://orcid.org/0009-0004-3653-2831>

Musa ÇIBUK^(*), is with Department of Computer Engineering, Bitlis Eren University, Bitlis, Turkey, (e-mail: mucibuk@beu.edu.tr)

 <https://orcid.org/0000-0001-9028-2221>

Erdal AKIN, is with 1 - Department of Computer Engineering, Bitlis Eren University, Bitlis, Turkey, 2 - Department of Computer Science and Media Technology, Malmö University, Malmö, Sweden, 3 - Internet of Things and People Centre, Malmö University, Malmö, Sweden (e-mail: e.akin@beu.edu.tr)

 <https://orcid.org/0000-0002-2223-3927>

Manuscript received Aug 19, 2024; accepted Sep 12, 2024.

DOI: [10.17694/bajece.1533966](https://doi.org/10.17694/bajece.1533966)

examined. A detailed literature review was then conducted on using these systems in fire recognition systems, investigating similar studies. Additionally, the use of datasets in fire recognition systems and their application in recognition processes were explored, with deep learning algorithms being examined in detail. The MATLAB [5] program, which offers many conveniences in coding and image processing, was used for these processes and algorithms. This program was also utilized to compare results, as well as to train and test the datasets. The five-fold cross-validation method was applied for verification in this study. Specifically, 20% of the dataset was used for testing, while the remaining 80% was used for training.

The rest of the paper is organized as follows: In Section 3, DL models used in this study are presented. In Section 4, we provided methods used for testing and training parameters of the compared algorithms. In Section 4, the results of the algorithms used in training are given with the details of the table graph and accuracy-time bubble graph. In Section 5, the conclusion section, the CNN architectural network with the fastest fire detection time and the best accuracy rate sensitivity is determined, and comments about the algorithm are given.

II. LITERATURE REVIEW

This section discusses DL-based CCN algorithms and datasets that will be used for this study

II.I. DL-based CNN algorithms

The emergence of DL algorithms is the result of the interest and concern for AI. CNNs, one of the deep learning algorithms, are used in many areas such as classification [6] and object recognition [7]. In this study, 20 DL-based CNNs with different features and capabilities, developed to solve different problems,

were preferred. These Algorithms are AlexNet [8-10], VGG-16 [11], VGG-19 [12, 13], GoogLeNet [14-18], Places-365 [19], ResNET-18 [20], ResNET-50 [21], ResNET-101 [22], ShuffleNET [23, 24], MobileNET [25], NASNET-Mobile [26], EfficientNET-B0 [27], Inception-v3 [28, 29], DarkNET-19 [30, 31], DarkNET-53 [32-34], Xception [35], Inception-ResNet [36], DenseNET-201 [37, 38], SqueezeNET [39, 40], and NASNet-Large [41, 42].

II.II. Dataset

In this study, we used two different datasets obtained from Kaggle [43, 44]. The images are in JPG and PNG formats with varying sizes. One dataset contains only fire images, 110 of which are in JPG format. The other dataset includes images categorized as either fire or non-fire, with 755 fire images and 244 non-fire images in PNG format. The combined dataset is summarized in Table 1.

The data is organized into two folders: the "fire" folder contains 865 fire images, some of which include heavy smoke, while the "no fire" folder contains 244 images of natural scenes (e.g., forest, grass, river, people, foggy forest, lake and animal). For comparative analysis of deep learning algorithms in fire detection, both fire and non-fire images are needed. To measure the accuracy, speed, and sensitivity of fire detection algorithms, we utilized the Fire Images and Non-Fire Images datasets from the Fire Dataset, which are publicly available.

The dataset comprises a total of 1,109 images: 865 fire images and 244 non-fire images. In this study, 80% of the images (both fire and non-fire) were used for training, while the remaining 20% were used as test data. As the dataset size increases, the training process for the model also lengthens, which is a disadvantage of having a larger and more diverse dataset.

TABLE I.
FIRE DATASET INFORMATION

	Percent	Dataset	Fire	Non-Fire	Total
Training Data	80%	Kaggle	865	244	1109
Test Data	20%				

III. METHODOLOGY

A hybrid dataset was created using the images described in Section II.2. The images in this dataset were trained with the 5-fold cross-validation technique for each algorithm using MATLAB. In transfer learning, the fully connected and classification layers of a previously trained network were

adapted to match the number of classes in the new dataset. Additionally, since the input dimensions of each network may vary, the images in the dataset were resized (preprocessed) to be compatible with the respective network. These operations were performed for each CNN used in the study. Fig. 1 illustrates the training of artificial neural networks via transfer learning.

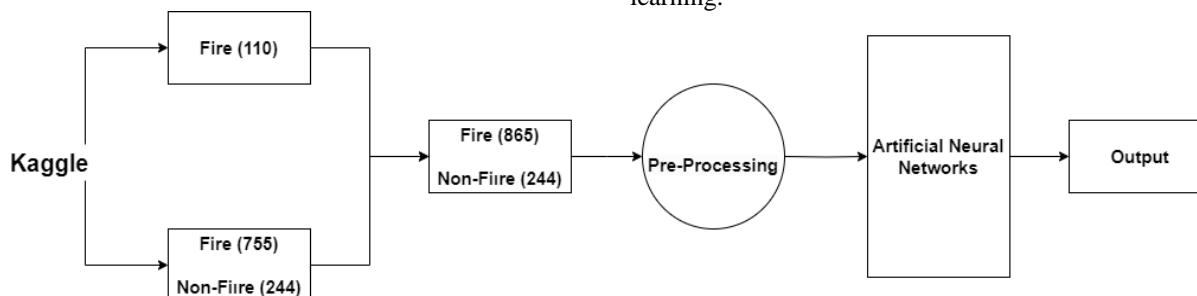


Fig. 1. Training ANNs with Transfer Learning

It has been observed that the 5-fold cross-validation technique used in the classification phase provides better performance in ensemble learning classifiers [45]. The cross-validation technique is a model validation method that tests how a statistical analysis will yield a result on an independent data set [46]. Its main use is to estimate how accurately a prediction system will work in practice. The cross-validation technique involves dividing the original data set into training and test sets. In this study, the data set was divided into five parts. One of these five parts is used for testing, and the other for training. If we train once with the training set after dividing and measuring its accuracy with the test set, it may not give accurate results. Therefore, cross-validation is used as a more robust method. We obtain results by training on the other parts, excluding one of the divided training sets in each iteration. We find our verified training success by averaging these results. The main purpose of this process is to obtain a more general performance result by eliminating random errors or successes that may occur during the random division of the data set into training and test sets.

IV. EVALUATION

In this section, we present a comparative analysis of the twenty models mentioned above on the fire dataset. First, we introduce the environmental setup, training parameters, and comparison metrics. Then, we discuss the experimental results.

IV.I. Setup

The computer used in this work has an AMD Ryzen Threadripper PRO 3975WX 32 processor, 128 GB RAM, and an NVIDIA RTX 3090 GPU. The algorithms are programmed, trained, and tested using MatLab programming language.

IV.II. Training Parameters

All training and testing processes in this thesis were carried out using the parameters shown in Table II.

TABLE II.
TRAINING PARAMETERS

Training Options	Value
Solver	sgdm
MaxEpoch	100
MiniBatch	64
InitialLearnRate	0.001
VerboseFrequency	20
ExecutionEnvironment	gpu
InitialLearnRate	0.001
LearnRateDropFactor	30
LearnRateSchedule	Piecewise

IV.III. Evaluation Metric

In this study, some basic evaluation metrics were used to compare the success of the CNNs in fire detection. These can be explained using confusion matrix expressions. A confusion matrix summarizes the number of correctly or incorrectly predicted examples made by a classification model [47]. In our study, we compared the algorithms using the accuracy metric derived from the confusion matrix.

The calculation relies on a confusion matrix that consists of four key components. True Positives (TP) indicate instances where the predicted label correctly aligns with the ground truth label. True Negatives (TN) occur when an object is present in the image but is not labeled in either the ground truth or the model's prediction. Conversely, False Positives (FP) refer to cases where the predicted label does not exist in the ground truth, while False Negatives (FN) represent instances where the ground truth label is missed. Accordingly, accuracy can be calculated as followed Eq.(1)

$$Accuracy = \frac{TP + TN}{TP + TN + FP + FN} \quad (1)$$

IV.IV. Results and Discussion

In this study, the aim is to compare architectures used for the fast and accurate detection and classification of fire images. Transfer learning and CNN architectures from deep learning tools were utilized to classify fire images. The 5-fold cross-validation method was employed to train the fire images in the dataset used in the thesis. This method aimed to increase performance accuracy. Transfer learning was applied using various CNN architectures during training. The correct prediction rates of the CNN architectures used are given in Table III. Additionally, the minimum, maximum and average accuracy rates are determined and shown. Upon examining these results, it is evident that CNN models provide accuracy rates above 95%, with the best-performing model being Places365, which achieved 98.92% accuracy. Therefore, training with 0 success (numbers 1 and 4) are not included in the average success calculation.

TABLE III.
PERFORMANCE RESULTS OBTAINED AFTER THE TRAINING

Arch. Name	Train Nr.	Accuracy Rate	Min. Accuracy Rate	Max. Accuracy Rate	Average Accuracy Rate
AlexNet	1	0,977	0,968	1,000	0,980
	2	1,000			
	3	0,977			
	4	0,968			
	5	0,977			
VGG-16	1	0,982	0,982	1,000	0,988
	2	1,000			
	3	0,986			
	4	0,982			
	5	0,991			
VGG-19	1	0	0,779	0,986	0,917
	2	0,779			
	3	0,986			
	4	0			
	5	0,986			
GoogleNet	1	0,986	0,986	0,991	0,988
	2	0,991			
	3	0,986			
	4	0,986			
	5	0,991			
Places365	1	0,977	0,977	1,000	0,989
	2	0,991			
	3	0,991			
	4	0,986			
	5	1,000			
ResNet-18	1	0,973	0,973	0,991	0,984
	2	0,991			
	3	0,982			
	4	0,986			
	5	0,986			

TABLE IV.
TRANSFER LEARNING TIME OF CNNs

ResNet-50	1	0,964	0,964	0,995	0,984
	2	0,986			
	3	0,995			
	4	0,986			
	5	0,986			
ResNet-101	1	0,968	0,968	0,991	0,984
	2	0,991			
	3	0,991			
	4	0,982			
	5	0,986			
Inception ResNetV2	1	0,968	0,941	0,982	0,959
	2	0,946			
	3	0,955			
	4	0,982			
	5	0,941			
Inception V3	1	0,959	0,959	0,986	0,974
	2	0,986			
	3	0,973			
	4	0,977			
	5	0,973			
Xception	1	0,977	0,973	0,986	0,980
	2	0,982			
	3	0,982			
	4	0,986			
	5	0,973			
MobileNet V2	1	0,955	0,955	0,995	0,978
	2	0,977			
	3	0,982			
	4	0,995			
	5	0,982			
DenseNet 201	1	0,964	0,964	0,991	0,981
	2	0,986			
	3	0,977			
	4	0,991			
	5	0,986			
ShuffleNet	1	0,968	0,968	0,995	0,984
	2	0,986			
	3	0,986			
	4	0,982			
	5	0,995			
DarkNet-19	1	0,982	0,977	1,000	0,986
	2	0,991			
	3	0,982			
	4	0,977			
	5	1,000			
DarkNet-53	1	0,977	0,973	0,991	0,982
	2	0,991			
	3	0,982			
	4	0,973			
	5	0,986			
Squeeze Net	1	0,968	0,968	0,991	0,980
	2	0,991			
	3	0,986			
	4	0,973			
	5	0,982			
Efficient Netb0	1	0,964	0,964	0,991	0,981
	2	0,991			
	3	0,977			
	4	0,982			
	5	0,991			
Nasnet Mobile	1	0,955	0,955	0,977	0,964
	2	0,968			
	3	0,964			
	4	0,977			
	5	0,955			
Nasnet Large	1	0,973	0,964	0,977	0,971
	2	0,968			
	3	0,964			
	4	0,973			
	5	0,977			

Architecture Name	Train Nr.	Train Time (sec)	Min. Train Time(sec)	Max. Train Time(sec)	Average Train Time(sec)
AlexNet	1	1491,388	1197,836	1491,388	1363,152
	2	1304,289			
	3	1410,524			
	4	1197,836			
	5	1411,724			
VGG-16	1	1635,139	1375,095	1635,139	1552,484
	2	1375,095			
	3	1599,697			
	4	1565,348			
	5	1587,144			
VGG-19	1	102,502	1505,025	1662,549	1592,657
	2	1610,398			
	3	1662,549			
	4	56,179			
	5	1505,025			
Google Net	1	1240,027	1190,833	1301,264	1247,654
	2	1190,833			
	3	1290,660			
	4	1301,264			
	5	1215,483			
Places365	1	1437,911	1313,062	2013,673	1714,209
	2	2013,673			
	3	2001,327			
	4	1805,073			
	5	1313,062			
ResNet-18	1	1300,322	1289,123	1485,557	1354,328
	2	1311,404			
	3	1289,123			
	4	1485,557			
	5	1385,236			
ResNet-50	1	1645,830	1623,943	1667,269	1651,649
	2	1661,276			
	3	1659,924			
	4	1667,269			
	5	1623,943			
ResNet-101	1	2879,792	2780,590	2965,620	2868,681
	2	2780,590			
	3	2851,332			
	4	2866,070			
	5	2965,620			
Inception ResNetV2	1	6976,200	5199,917	6976,200	5825,375
	2	5344,980			
	3	5199,917			
	4	5611,612			
	5	5994,166			
Inception V3	1	2619,109	2498,057	2619,109	2539,804
	2	2505,140			
	3	2546,038			
	4	2498,057			
	5	2530,675			
Xception	1	2808,732	2808,732	2899,488	2853,818
	2	2899,379			
	3	2899,488			
	4	2823,931			
	5	2837,557			
MobileNet V2	1	1500,697	1471,133	1910,811	1651,502
	2	1471,133			
	3	1910,811			
	4	1582,319			
	5	1792,549			
DenseNet 201	1	6037,628	6037,628	6168,289	6121,425
	2	6093,988			
	3	6168,289			
	4	6157,341			
	5	6149,883			
ShuffleNet	1	1517,110	1336,175	1711,300	1519,916
	2	1472,689			
	3	1562,304			
	4	1336,175			
	5	1711,300			
DarkNet -19	1	1277,612	1277,612	1526,030	1426,151
	2	1444,860			
	3	1526,030			
	4	1379,137			
	5	1503,114			

DarkNet-53	1	2492,582	2433,511	2554,308	2490,212
	2	2486,306			
	3	2554,308			
	4	2484,351			
	5	2433,511			
SqueezeNet	1	1363,345	1278,258	1564,867	1391,218
	2	1278,258			
	3	1445,699			
	4	1303,923			
	5	1564,867			
EfficientNetB0	1	3425,724	3352,167	3566,620	3440,623
	2	3566,620			
	3	3355,723			
	4	3502,878			
	5	3352,167			
Nasnet Mobile	1	4083,264	3862,247	4117,353	4039,916
	2	4088,674			
	3	4117,353			
	4	4048,043			
	5	3862,247			
Nasnet Large	1	64203,660	50707,532	64203,660	55155,781
	2	53066,790			
	3	56133,841			
	4	50707,532			
	5	51667,084			

The transfer learning times of the CNNs on which the dataset was trained in this study are shown in Table IV. The table provides the minimum, maximum, and average learning times of 5 different CNNs in seconds. Although the most successful architecture according to the learning time results was VGG-19 (987.33 seconds), it was not taken into consideration due to the computational problems in VGG-19 (training numbered 1 and 4). When considering the learning

times, it is evident that the CNN architecture with the most successful average results is GoogLeNet.

The accuracy-time bubble graph in Figure II allows us to comment on the performance rates and learning times of the CNN architectures used in the study by presenting both data together. This figure is essentially a visual combination of Table 3 and Table 4. When examining the accuracy-time bubble graph, it is evident that the fire detection times and correct prediction rates of CNN architecture models such as Place365, GoogLeNet, VGG-16, and DarkNet are quite high. Although 100% accuracy rates were obtained, this can be attributed to the ease of the selected dataset pieces. Therefore, the 5-fold cross-validation results are more significant.

Another notable point is that the VGG-19 architecture showed 0 success in 2 trainings. This can be explained by a computational error or a procedural error in the learning of VGG-19 for those distributions in the dataset. On the other hand, the fact that almost all CNN models (except VGG-19) have an average performance above 95% can be attributed to the small number of classes (2 classes) and the dataset adequately representing the purpose. As a result, in this study conducted using transfer learning for fire detection, it is seen that the GoogLeNet architecture stands out in terms of duration, and the Place365 architecture, based on GoogLeNet, stands out in terms of performance. With its complex and advanced structure, NasNet architectures did not perform as expected (specifically for this dataset) in terms of duration and performance.

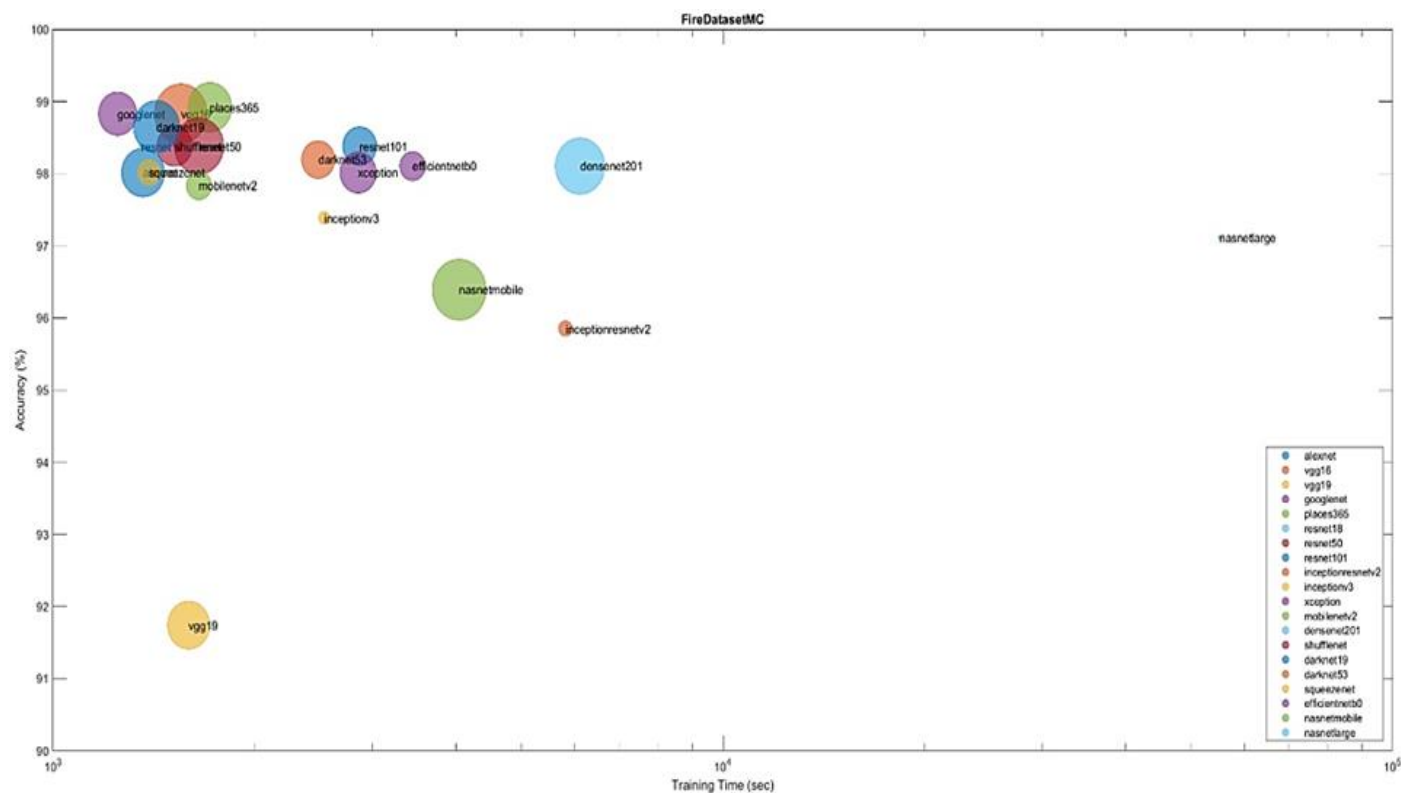


Fig. 2. Accuracy-Time Bubble Chart of Used Algorithms

V. CONCLUSION

In this study, although the performances (accuracy, training time) of CNNs, which we used for the development of fire detection technology from images and which are essentially ANNs, achieved 100% accuracy rates, this can be attributed to the ease of the selected dataset pieces. Therefore, the 5-fold cross-validation results are more significant. Another notable point is that the VGG-19 architecture (numbered 1 and 4) showed 0 performance in 2 trainings. This can be explained by a computational problem or an error in learning VGG-19 for those distributions in the dataset. On the other hand, the fact that almost all CNN models (except VGG-19) showed an average performance above 95% can be attributed to the small number of classes (2 classes) and the dataset adequately representing the purpose. Detailed accuracy-time bubble charts in Table 3, Table 4, and Figure 2 illustrate this.

According to the results obtained from 20 different CNN architectures, almost all algorithms demonstrate over 95% accuracy (generally around 98%) in detecting fire. If we compare the test results in the study, the algorithm with the highest success rate was Place365, with 98.92%. GoogLeNet was the best network, with an average training time of 1247.65 seconds.

The high performance of these algorithms highlights that the use of deep learning-based CNN architectures is an important alternative solution for preventing or minimizing loss of life and property by detecting fire early. This study has demonstrated that GoogLeNet-based CNN architectures (GoogLeNet and Place365) provide more effective results in fire detection. For future studies, it is recommended to further enhance the performance of these GoogLeNet-based deep learning architectures by customizing them specifically for fire detection purposes.

REFERENCES

- [1]. K. Avazov, M. Mukhiddinov, F. Makhmudov, and Y. I. Cho, "Fire detection method in smart city environments using a deep-learning-based approach," *Electron.*, vol. 11, no. 1, pp. 1–17, 2022, doi: 10.3390/electronics11010073.
- [2]. C. Tao, J. Zhang, and P. Wang, "Smoke Detection Based on Deep Convolutional Neural Networks," in *2016 International Conference on Industrial Informatics - Computing Technology, Intelligent Technology, Industrial Information Integration (ICIICII)*, Dec. 2016, pp. 150–153. doi: 10.1109/ICIICII.2016.0045.
- [3]. P. Li and W. Zhao, "Image fire detection algorithms based on convolutional neural networks," *Case Stud. Therm. Eng.*, vol. 19, p. 100625, Jun. 2020, doi: 10.1016/j.csite.2020.100625.
- [4]. K. Muhammad, J. Ahmad, I. Mehmood, S. Rho, and S. W. Baik, "Convolutional Neural Networks Based Fire Detection in Surveillance Videos," *IEEE Access*, vol. 6, pp. 18174–18183, 2018, doi: 10.1109/ACCESS.2018.2812835.
- [5]. G. Lindfield and J. Penny, "Numerical methods: Using MATLAB," *Numer. Methods Using MATLAB*, pp. 1–608, 2018, doi: 10.1016/C2016-0-00395-9.
- [6]. M. Cibuk, U. Budak, Y. Guo, M. Cevdet Ince, and A. Sengur, "Efficient deep features selections and classification for flower species recognition," *Meas. J. Int. Meas. Confed.*, vol. 137, pp. 7–13, 2019, doi: 10.1016/j.measurement.2019.01.041
- [7]. R. Daş, B. Polat, and G. Tuna, "Derin Öğrenme ile Resim ve Videolarda Nesnelerin Tanınması ve Takibi," *Fırat Üniversitesi Mühendislik Bilim. Derg.*, vol. 31, no. 2, pp. 571–581, 2019, doi: 10.35234/fumbd.608778.
- [8]. C. Alippi, S. Disabato, and M. Roveri, "Moving Convolutional Neural Networks to Embedded Systems: The AlexNet and VGG-16 Case," in *2018 17th ACM/IEEE International Conference on Information Processing in Sensor Networks (IPSN)*, Apr. 2018, vol. 30, no. 2010, pp. 212–223. doi: 10.1109/IPSN.2018.00049.
- [9]. H. Ismail Fawaz *et al.*, "InceptionTime: Finding AlexNet for time series classification," *Data Min. Knowl. Discov.*, vol. 34, no. 6, pp. 1936–1962, 2020, doi: 10.1007/s10618-020-00710-y.
- [10]. A. LeNail, "NN-SVG: Publication-Ready Neural Network Architecture Schematics," *J. Open Source Softw.*, vol. 4, no. 33, p. 747, Jan. 2019, doi: 10.21105/joss.00747.
- [11]. S. Tammina, "Transfer learning using VGG-16 with Deep Convolutional Neural Network for Classifying Images," *Int. J. Sci. Res. Publ.*, vol. 9, no. 10, p. p9420, 2019, doi: 10.29322/ijrsp.9.10.2019.p9420.
- [12]. K. Simonyan and A. Zisserman, "Very deep convolutional networks for large-scale image recognition," *3rd Int. Conf. Learn. Represent. ICLR 2015 - Conf. Track Proc.*, pp. 1–14, 2015.
- [13]. M. Mateen, J. Wen, Nasrullah, S. Song, and Z. Huang, "Fundus Image Classification Using VGG-19 Architecture with PCA and SVD," *Symmetry (Basel)*, vol. 11, no. 1, p. 1, Dec. 2018, doi: 10.3390/sym11010001.
- [14]. G. Zeng, Y. He, Z. Yu, X. Yang, R. Yang, and L. Zhang, "Preparation of novel high copper ions removal membranes by embedding organosilane-functionalized multi-walled carbon nanotube," *J. Chem. Technol. Biotechnol.*, vol. 91, no. 8, pp. 2322–2330, 2016, doi: 10.1002/jctb.4820.
- [15]. M. Långkvist, L. Karlsson, and A. Loutfi, "Inception-v4, Inception-ResNet and the Impact of Residual Connections on Learning," *Pattern Recognit. Lett.*, vol. 42, no. 1, pp. 11–24, 2014, [Online]. Available: <http://arxiv.org/abs/1512.00567>
- [16]. H.-J. Yoo, "Deep Convolution Neural Networks in Computer Vision: a Review," *IEIE Trans. Smart Process. Comput.*, vol. 4, no. 1, pp. 35–43, 2015, doi: 10.5573/ieiespc.2015.4.1.035.
- [17]. C. Szegedy, V. Vanhoucke, S. Ioffe, J. Shlens, and Z. Wojna, "Rethinking the Inception Architecture for Computer Vision," *Proc. IEEE Comput. Soc. Conf. Comput. Vis. Pattern Recognit.*, vol. 2016-Decem, pp. 2818–2826, 2016, doi: 10.1109/CVPR.2016.308.
- [18]. C. Szegedy *et al.*, "Going deeper with convolutions," *Proc. IEEE Comput. Soc. Conf. Comput. Vis. Pattern Recognit.*, vol. 07-12-June, pp. 1–9, 2015, doi: 10.1109/CVPR.2015.7298594.
- [19]. "GoogLeNet evrişimli sinir ağı-MATLAB googlenet." [Online]. Available: https://www.mathworks.com/help/deeplearning/ref/googlenet.html#mw_d60d4ed6-a2c9-44f1-93b8-977191c6cfea
- [20]. M. Guo and Y. Du, "Classification of Thyroid Ultrasound Standard Plane Images using ResNet-18 Networks," in *2019 IEEE 13th International Conference on Anti-counterfeiting, Security, and Identification (ASID)*, Oct. 2019, pp. 324–328. doi: 10.1109/ICASID.2019.8925267.
- [21]. I. Z. Mukti and D. Biswas, "Transfer Learning Based Plant Diseases Detection Using ResNet50," in *2019 4th International Conference on Electrical Information and Communication Technology (EICT)*, Dec. 2019, pp. 1–6. doi: 10.1109/EICT48899.2019.9068805.
- [22]. P. Ghosal, L. Nandanwar, S. Kanchan, A. Bhadra, J. Chakraborty, and D. Nandi, "Brain Tumor Classification Using ResNet-101 Based Squeeze and Excitation Deep Neural Network," in *2019 Second International Conference on Advanced Computational and Communication Paradigms (ICACCP)*, Feb. 2019, pp. 1–6. doi: 10.1109/ICACCP.2019.8882973.
- [23]. J. Bobo, C. Hudley, and C. Michel, "The Black studies reader," *Black Stud. Read.*, pp. 1–488, 2004, doi: 10.4324/9780203491348.
- [24]. R. Zhang *et al.*, "Automatic Segmentation of Acute Ischemic Stroke From DWI Using 3-D Fully Convolutional DenseNets," *IEEE Trans. Med. Imaging*, vol. 37, no. 9, pp. 2149–2160, 2018, doi: 10.1109/TMI.2018.2821244.
- [25]. B. Khasoggi, E. Ermatita, and S. Samsuryadi, "Efficient mobilenet architecture as image recognition on mobile and embedded devices," *Indones. J. Electr. Eng. Comput. Sci.*, vol. 16, no. 1, p. 389, Oct. 2019, doi: 10.11591/ijeecs.v16.i1.pp389-394.
- [26]. F. Saxen, P. Werner, S. Handrich, E. Othman, L. Dinges, and A. Al-Hamadi, "Face Attribute Detection with MobileNetV2 and NasNet-Mobile," in *2019 11th International Symposium on Image and Signal*

- Processing and Analysis (ISPA)*, Sep. 2019, pp. 176–180. doi: 10.1109/ISPA.2019.8868585.
- [27]. R. H. Hridoy, F. Akter, M. Mahfuzullah, and F. Ferdowsy, "A Computer Vision Based Food Recognition Approach for Controlling Inflammation to Enhance Quality of Life of Psoriasis Patients," in *2021 International Conference on Information Technology (ICIT)*, Jul. 2021, pp. 543–548. doi: 10.1109/ICIT52682.2021.9491783.
- [28]. M. Nikhitha, S. Roopa Sri, and B. Uma Maheswari, "Fruit Recognition and Grade of Disease Detection using Inception V3 Model," in *2019 3rd International conference on Electronics, Communication and Aerospace Technology (ICECA)*, Jun. 2019, vol. 9, pp. 1040–1043. doi: 10.1109/ICECA.2019.8822095.
- [29]. Xiaoling Xia, Cui Xu, and Bing Nan, "Inception-v3 for flower classification," in *2017 2nd International Conference on Image, Vision and Computing (ICIVC)*, Jun. 2017, pp. 783–787. doi: 10.1109/ICIVC.2017.7984661.
- [30]. Redmon, Joseph, and Ali Farhadi. "YOLO9000: better, faster, stronger." In *Proceedings of the IEEE conference on computer vision and pattern recognition*, pp. 7263–7271. 2017.
- [31]. J. Redmon and A. Farhadi, "YOLOv3: An Incremental Improvement," Apr. 2018, doi: 10.11772/j.issn.1001-9081.2018102190.
- [32]. Huang, Xin, Xinxin Wang, Wenyu Lv, Xiaying Bai, Xiang Long, Kaipeng Deng, Qingqing Dang et al. "PP-YOLOv2: A practical object detector." arXiv preprint arXiv:2104.10419 (2021).
- [33]. J. Deng, W. Dong, R. Socher, L.-J. Li, Kai Li, and Li Fei-Fei, "ImageNet: A large-scale hierarchical image database," in *2009 IEEE Conference on Computer Vision and Pattern Recognition*, Jun. 2009, pp. 248–255. doi: 10.7287/peerj.preprints.27880v1.
- [34]. R. S. T. De Menezes, J. V. A. Luiz, A. M. Henrique-Alves, R. M. Santa Cruz, and H. Maia, "Mice Tracking Using The YOLO Algorithm," pp. 162–173, 2020, doi: 10.5753/semish.2020.11326.
- [35]. F. Chollet, "Xception: Deep Learning with Depthwise Separable Convolutions," in *2017 IEEE Conference on Computer Vision and Pattern Recognition (CVPR)*, Jul. 2017, pp. 1800–1807. doi: 10.1109/CVPR.2017.195.
- [36]. Y. Bhatia, A. Bajpayee, D. Raghuvanshi, and H. Mittal, "Image Captioning using Google's Inception-resnet-v2 and Recurrent Neural Network," in *2019 Twelfth International Conference on Contemporary Computing (IC3)*, Aug. 2019, pp. 1–6. doi: 10.1109/IC3.2019.8844921.
- [37]. G. Huang, Z. Liu, L. Van Der Maaten, and K. Q. Weinberger, "Densely connected convolutional networks," *Proc. - 30th IEEE Conf. Comput. Vis. Pattern Recognition, CVPR 2017*, vol. 2017-Janua, pp. 2261–2269, 2017, doi: 10.1109/CVPR.2017.243.
- [38]. K. Zhang, Y. Guo, X. Yuan, and Q. Ding, "Multiple Feature Reweight DenseNet for Image Classification," *IEEE Access*, vol. 7, pp. 9872–9880, 2019, doi: 10.1109/ACCESS.2018.2890127.
- [39]. F. Iandola, A. Shaw, R. Krishna, and K. Keutzer, "SqueezeBERT: What can computer vision teach NLP about efficient neural networks?," in *Proceedings of SustainNLP: Workshop on Simple and Efficient Natural Language Processing*, 2020, pp. 124–135. doi: 10.18653/v1/2020.sustainlp-1.17.
- [40]. F. Özyurt, E. Sert, E. Avci, and E. Dogantekin, "Brain tumor detection based on Convolutional Neural Network with neutrosophic expert maximum fuzzy sure entropy," *Measurement*, vol. 147, p. 106830, Dec. 2019, doi: 10.1016/j.measurement.2019.07.058.
- [41]. D. Ghimire, D. Kil, and S. Kim, "A Survey on Efficient Convolutional Neural Networks and Hardware Acceleration," *Electronics*, vol. 11, no. 6, p. 945, Mar. 2022, doi: 10.3390/electronics11060945.
- [42]. S. I. Hossain et al., "Exploring convolutional neural networks with transfer learning for diagnosing Lyme disease from skin lesion images," *Comput. Methods Programs Biomed.*, vol. 215, p. 106624, Mar. 2022, doi: 10.1016/j.cmpb.2022.106624.
- [43]. A. Saied, "FIRE Dataset," *Kaggle.com*, 2018. <https://www.kaggle.com/datasets/phyllake1337/fire-dataset> (accessed Jul. 30, 2024).
- [44]. A. Kumar, "Fire Detection Dataset," *Kaggle.com*, 2024. <https://www.kaggle.com/datasets/atulyakumar98/test-dataset> (accessed Jul. 30, 2024).
- [45]. M. Burukanli, M. Çibuk, and Ü. Budak, "Saldırı Tespiti için Makine Öğrenme Yöntemlerinin Karşılaştırmalı Analizi Comparative Analysis of Machine Learning Methods for Intrusion Detection," *BEU J. Sci.*, vol. 10, no. 2, pp. 613–624, 2021.
- [46]. R. Kohavi, "A Study of Cross-Validation and Bootstrap for Accuracy Estimation and Model Selection," *Int. Jt. Conf. Artif. Intell.*, no. March 2001, 1995.
- [47]. F. Uyanık and M. C. and Kasapbaşı, "Telekomünikasyon Sektörü için Veri Madenciliği ve Makine Öğrenmesi Teknikleri ile Ayrılan Müşteri Analizi," *Düzce Üniversitesi Bilim ve Teknoloji Dergisi*, 2021.

BIOGRAPHIES



Remzi GÖÇMEN, He received his undergraduate degree from Marmara University Istanbul Department of Electrical and Electronics Education in 1998, and his master's degree from Bitlis Eren University Department of Electrical and Electronics Engineering in 2023. He currently works within the Ministry of National Education. His main areas of interest are: Deep Learning, Artificial Neural Networks



Musa ÇIBUK, He got his bachelors' degree in the Electrical-Electronic Engineering Department at Fırat University, Elazığ/Turkey in 1997, his master degree in the Electrical-Electronic Engineering Department at Fırat University, Elazığ/Turkey in 2002 and PhD degree in the Electrical-Electronic Engineering Department at Fırat University, Elazığ/Turkey in 2009. He is still an academic member of the Computer Engineering Department at Bitlis Eren University. His major areas of interests are: Protocol Design, Sensor Networks, Artificial Neural Networks and Image Processing



Erdal AKIN was born in Ceyhan, Adana, Turkey. He received the degree from the Department of Mathematics, Yıldız Technical University, Istanbul, in 2008, and the master's and Ph.D. degrees from the Department of Computer Science, The University of Texas at San Antonio (UTSA), San Antonio, TX, USA, in 2014 and 2018, respectively. His research interests include deep reinforcement learning, software-defined networks, security, the IoT, computer vision, and blockchain. In 2009, he received the Republic of Turkey Ministry of National Education Scholarship to study in the USA.

Research Article

A Comparison Study of Some Metaheuristic Methods for Field Oriented Control Based Induction Motors

Hersh Hasan Taha Al-Dawoodi and Huseyin Aygun


Abstract—Thanks to the accuracy, high reliability and excellent performance, field-oriented control (FOC) based induction motor (IM) drives are used in power applications. Generally, three PI controllers are used for speed control, and decoupling control of torque and flux provided by control of d-q components of stator current in FOC based IM. The common practice for tuning PI controller gains involves trial and error or the Ziegler-Nichols method. Unfortunately, these methods tend to lack effectiveness in achieving a robust dynamic response. In this paper, to overcome the drawbacks of classical PI tuning methods, some metaheuristic methods such as Grey Wolf Optimization (GWO), Artificial Bee Colony (ABC) and Particle Swarm Optimization (PSO) algorithms are used to determine the optimal values of the PI controller parameters to improve the dynamic performance of FOC based IM. A multi-objective function based on sum of absolute errors (SAE) is selected for this purpose. A detail comparison of methods is given in terms of convergence factor and control performance considering the transient response parameters. Control performance is evaluated under 3 operating conditions (constant reference speed at no load condition, variable reference speed at nominal load operation, and sudden load change condition). The simulation results indicate that, despite its slower convergence speed compared to other algorithms, the GWO algorithm achieves the best dynamic performance.

Index Terms—ABC, Field Oriented Control, GWO, Induction Motor, Metaheuristic, PSO.


I. INTRODUCTION

Induction motors (IMs) are widely utilized across various applications, including household appliances, industrial facilities, automation systems, and even electric vehicles,

HERSH HASAN TAHA AL-DAWOODI, is with Department of Electrical-Electronics Engineering University of Karabuk, Karabuk, Turkey, (e-mail: herieshhassan@gmail.com).

 <https://orcid.org/0009-0002-4158-7226>

HILMI AYGUN, is with Department of Mechatronics Engineering University of Karabuk, Karabuk, Turkey, (e-mail: hilmiaygun@karabuk.edu.tr).

 <https://orcid.org/0000-0002-9073-2322>

Manuscript received Aug 20, 2023; accepted Feb 22, 2024.
DOI: 10.17694/bajece.1346432

owing to their straightforward design, cost-effectiveness, minimal maintenance requirements, high power density, and resilience in challenging environments [1]. Fig. 1 illustrates the cross-sectional structure of a squirrel cage IM. Stator windings are supplied with three-phase AC voltages, generating three-phase currents that produce a rotating magnetic field. This field induces a magnetic field in the rotor due to the short-circuited rotor bars. Consequently, a slip occurs between the speed of the rotating magnetic field, known as synchronous speed, and the rotor speed. The synchronous speed, as defined in Eq. (1), depends on the stator frequency and the number of poles. Therefore, the speed of an IM can be controlled by adjusting the stator frequency.

$$N_s = \frac{120f}{P} \quad (1)$$

Where N_s is the synchronous speed, f is the stator frequency and P is the pole number.

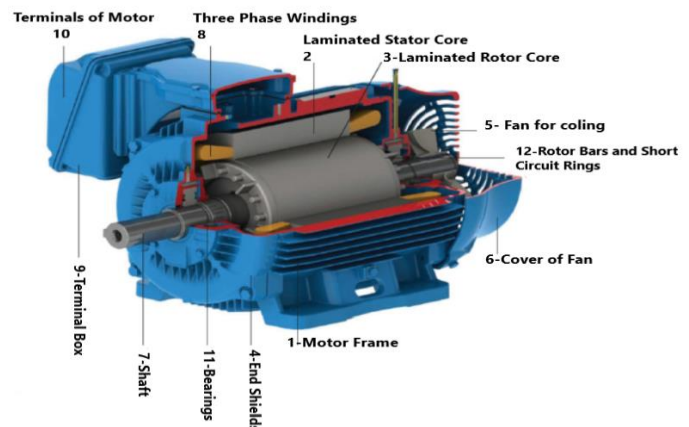


Fig. 1. Cross sectional structure of squirrel cage IM

Fast and precise torque response with effective flux regulation is a critical requirement for high-performance applications like robotics, rolling mills, and electric vehicles. Several methods such as field-oriented control (FOC), direct torque control (DTC) and space vector modulated direct torque control (DTC-SVM) have been proposed to obtain these requirements [2, 22-24]. This paper focuses on the FOC of IM drives.

In FOC based drives, the decoupling control of torque and flux provides a high dynamic response. It is realized by control of d - q components of stator current individually. Generally, FOC method consists of three PI controllers used for speed control and d - q components control of stator current. The tuning of PI controller parameters presents a challenging problem, commonly addressed through trial and error or the Ziegler-Nichols method based on step response characteristics. Regrettably, these methods frequently lead to a diminished dynamic response, particularly in scenarios involving variable speed references and sudden load changes. In the literature, some controllers such as neuro-fuzzy controller [25], neural network controller [26], fuzzy logic controller [27], fuzzy logic-based PI controller [28], sliding mode controller [29] and backstepping controller [30] have been used for FOC of IM instead of conventional PI controllers. In contemporary research, there is a growing trend of employing metaheuristic optimization algorithms as alternative tools for optimizing PI controller parameters. This shift is driven by the need to overcome the drawbacks of traditional PI controllers.

In [3], Particle Swarm Optimization (PSO) was used to determine the optimal parameters of PI and PID controllers for the speed control. The findings indicate that PSO proved to be more effective in enhancing speed response and delivering greater stability compared to the Ziegler-Nichols method. In [4], Ant Colony Optimization (ACO) algorithm was used to tune online identification of the controller parameters in the vector control of IM during operation such as changes in mechanical and electrical parameters of IM. It improved the steady state characteristics and dynamic performance. In [5], a vector-control based IM drive was designed to improve efficiency and to decrease torque fluctuations. The PSO algorithm was employed to optimize the parameters of the PI controller. The outcomes demonstrated a notable reduction in torque fluctuations when these fluctuations were taken into account as part of the objective function. In [18], a self-tuned PID speed controller was designed by Artificial Bee Colony (ABC) algorithm to improve the robustness. In [19], indirect vector control of IM was realized by a Genetic Algorithm (GA) based PI controller. The speed response with the proposed controller was better than that with PI and PI-Fuzzy Hybrid controller in terms of settling time, rising time and overshoot.

In [6], the quantum-behaved lightning search algorithm (QLSA) was utilized to develop an optimal fuzzy speed controller and optimal PI current controllers. The results demonstrated that QLSA outperformed the lightning search algorithm (LSA), backtracking search algorithm (BSA), gravitational search algorithm (GSA), and PSO in terms of damping capability and enhancing transient responses during sudden changes in speed and load torque. In [7], a combination of Kharitonov's theorem and PSO was applied to design the PI controllers against parameters uncertainty.

In [8], a comparison study using PSO, JAYA algorithm and Teacher Learner based Optimization (TLBO) algorithm was presented for optimizing the parameters of Fractional-order PI (FOPI) and PI controllers. The results showed that JAYA algorithm provided a better response in steady state than the other algorithms.

Nomenclature

i_a, i_b, i_c	three-phase stator currents, A
i_d, i_q	two-phase stator currents, A
i_α, i_β	stator current components along α and β axes, A
V_d, V_q	two-phase stator voltages, V
V_α, V_β	stator voltage components along α and β axes, V
Ψ_d, Ψ_q	two-phase stator fluxes, Wb
R_s, R_r	stator and rotor resistances, Ω
L_s, L_r	stator and rotor inductances, H
L_m	mutual inductance, H
n_p	number of pole pair
J	inertia torque, kg m^2
f_d	friction coefficient, Nm s/rad
T_e	electromagnetic torque, Nm
K_t	torque constant
ω_s, ω_r	stator and rotor angular speeds, rad/s
ω_{sl}	slip angular speed, rad/s
τ_r	rotor time constant

In [9], population extremal optimization (PEO) algorithm was used to tune PID controller of speed control loop which had a two-degree-of-freedom (2-DOF) structure to provide smoother torque response.

In [20], PSO and GA algorithms based Parallel Proportional Integral (PPI) controllers were used to control the speed of FOC based IM. PSO based PPI controller exhibited a better dynamic response at high speeds. However, at low speeds, GA based PPI controller exhibited better results. In [21], the PI controllers were optimized by Grey Wolf Optimization (GWO) and TLBO. For the evaluation, several objective functions such as the integral time-multiplied absolute error (ITAE), Zwe-Lee Gaing's parameter (ZLG) and Mean Squared Error (MSE) were used. The best performance was obtained by GWO algorithm using ZLG objective function. Developed optimization algorithms for FOC based IM are listed in Table 1.

In this study, some metaheuristic methods such as GWO, ABC and PSO algorithms were used to obtain the optimal PI controller parameters not only for speed control loop but also for d - q component control loops of stator current to improve the dynamic performance of FOC based IM and the results were compared.

TABLE I
METAHEURISTIC ALGORITHMS FOR FOC BASED IM IN LITERATURE

Algorithm	Optimization	Performance
PSO [3]	Optimization of PI/PID speed controller	improved speed response and more stable results than Ziegler-Nichols method
ACO [4]	Optimization of PID speed controller	Improved dynamic performance and steady state characteristics
PSO [5]	Optimization of PI speed controller and flux controllers	Reduced torque fluctuations
QLSA [6]	Optimization of fuzzy speed controller and PI current controllers	Better performance in terms of damping capability, robustness, and improvement in transient responses than LSA, BSA, GSA and PSO
Combination of PSO and Kharitonov's theorem [7]	Optimization of PI speed controller and PI current controllers	A high level of stability against parameter uncertainty
Comparison of PSO, TLBO and JAYA [8]	Optimization of PI/FOPI speed controller and PI/FOPI current controllers	Better response in steady state by JAYA than other algorithms
PEO [9]	Optimization of 2-DOF PID speed controller	Superior performances of the 2-DOF control over the 1-DOF one in terms of torque smoothing and speed tracking
ABC [18]	Optimization of PID speed controller	Excellent dynamic response and robustness with self-tuned parameters
GA [19]	Optimization of PID speed controller	Better performance than PI and PI-Fuzzy Hybrid Controllers in terms of settling time, rising time and peak overshoot
Comparison of PSO and GA [20]	Optimization of PPI speed controller	At high speeds, better dynamic response with PPI-PSO. At low speeds, better dynamic response with PPI-GA.
Comparison of GWO and TLBO [21]	Optimization of PI speed controller and PI current controllers	Best performance by GWO using ZLG objective function

II. FIELD ORIENTED CONTROL METHOD

In the field-oriented control (FOC) of induction motor, a decoupling control of flux and torque provided by d - q components control of stator current is applied to obtain high dynamic performance. The operations are realized through the d - q rotating frame with the rotor flux vector. The field flux linkage component is aligned with the d -axis, and the torque component is aligned with the q -axis [10]. The electromagnetic torque can be expressed by Eq. (2).

$$T_e = \frac{3}{2} n_p \frac{L_m}{L_r} (\Psi_d i_q - \Psi_q i_d) \quad (2)$$

Where n_p is the number of pole pair, L_m is the mutual inductance, L_r is the rotor inductance, Ψ_d and Ψ_q are the d - q components of rotor flux, i_d and i_q are the d - q components of stator current. In the FOC method, d -axis of the reference frame is locked onto the rotor flux vector, so $\Psi_q=0$. Therefore,

the torque equation given in Eq. (3) becomes like that of DC motors.

$$T_e = \frac{3}{2} n_p \frac{L_m}{L_r} \Psi_d^* i_q \quad (3)$$

Fig. 2 shows the general block diagram of FOC based IM. To control the speed, PI speed controller determines torque reference value (T_e^*) by using the speed error as the input. If the torque constant value (K_t) is defined as shown in Eq. (4) by utilizing from Eq. (3), the reference value of q -component of stator current (i_q^*) is obtained as shown in Eq. (5). Here, Ψ_d^* is the reference value of rotor flux which is determined by the user.

$$K_t = \frac{3}{2} n_p \frac{L_m}{L_r} \Psi_d^* \quad (4)$$

$$i_q^* = T_e^* / K_t \tag{5}$$

Also, the reference value of d -component of stator current is determined as shown in Eq. (6).

$$i_d^* = \Psi_d^* / L_m \tag{6}$$

To control the reference values of d - q components of stator current, two PI current controllers determine the reference values of d - q components of stator voltage (V_d^* and V_q^*). After the V_d^* and V_q^* are converted to the reference values of α - β components of stator voltage (V_α^* and V_β^*) by inverse park transformation, space vector pulse width modulation (SVPWM) is applied to the voltage source inverter (VSI) [11].

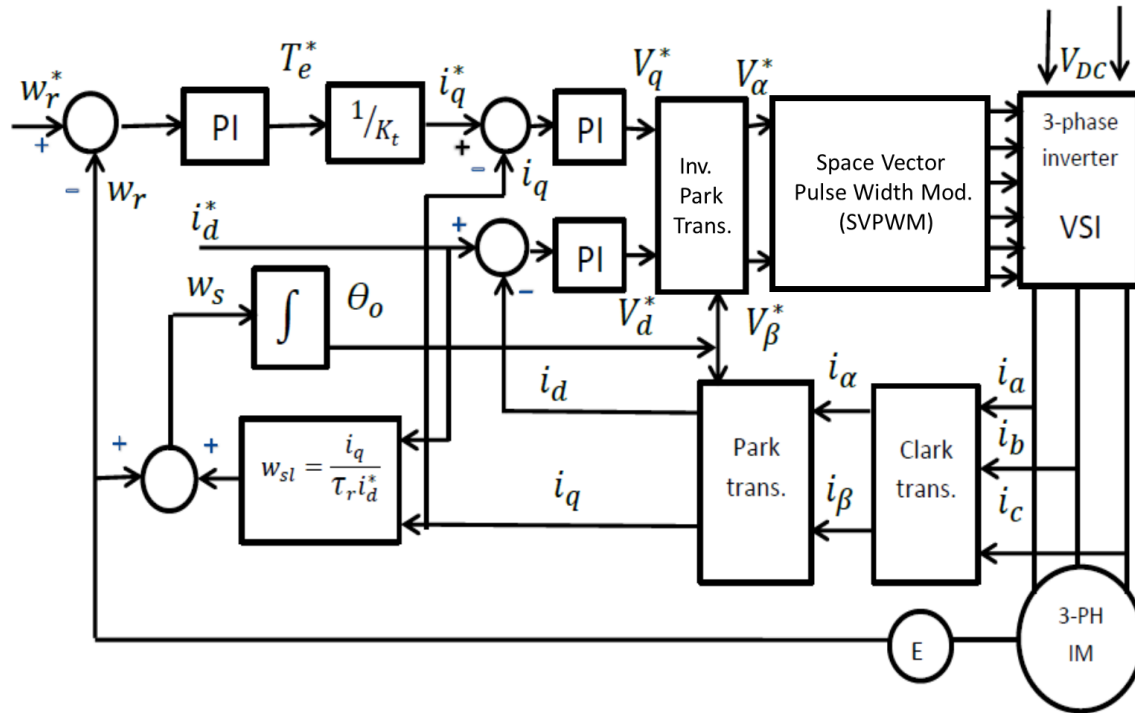


Fig. 2. Block Diagram of FOC based IM

III. METAHEURISTIC OPTIMIZATION METHODS

A. Grey Wolf Optimization Algorithm

In recent years, Grey Wolf Optimization (GWO) algorithm has been widely used in the optimization problems. This algorithm simulates the hunting behavior observed in grey wolves in their natural environment. The hierarchical structure consists of four distinct types of grey wolves: alpha, beta, delta, and omega, as illustrated in Fig. 3. The alpha wolves hold key responsibilities, including decisions related to hunting strategies, selection of sleeping locations, wake-up times, and other critical matters. Despite not being the physically strongest members, alphas excel in managerial abilities. The beta wolves play a supportive role by assisting the alphas in decision-making processes and contributing to various group activities. The lowest level in the hierarchy of the grey wolves is omega. In case of losing the omega, the group can have problems such as internal fighting. The rest of the grey wolves are called deltas. They have to submit to alphas and betas, but they dominate the omegas [12].

The main phases of hunting are shown in Fig. 3. The first one is approaching the prey. The second one is pursuing, harassing, and encircling the prey until the prey stops moving. The last one is attacking towards the prey. The encircling prey behaviour of grey wolves is mathematically modelled by the following equations.

$$\vec{D} = |\vec{C} \cdot \vec{X}_p(t) - \vec{X}(t)| \tag{7}$$

$$\vec{X}(t+1) = \vec{X}_p(t) - \vec{A} \cdot \vec{D} \tag{8}$$

Where t is the current iteration, \vec{X}_p is the position vector of the prey, \vec{X} is the position vector of any grey wolf. \vec{A} and \vec{C} coefficient vectors are given by the following equations.

$$\vec{A} = 2\vec{a} \cdot \vec{r}_1 - \vec{a} \tag{9}$$

$$\vec{C} = 2 \cdot \vec{r}_2 \tag{10}$$

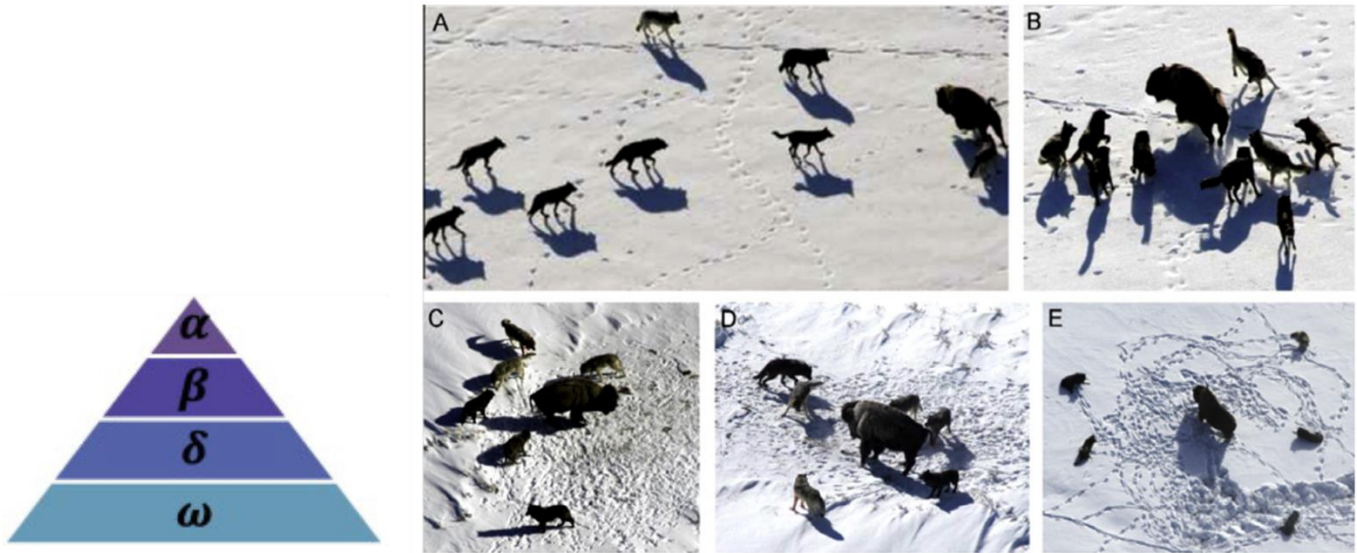


Fig. 3. Hierarchy and Hunting Behaviour of Grey Wolves: (A) Approaching the Prey (B-D) Pursuing, Harassing, and Encircling (E) Attacking [14]

Where \vec{a} is reduced linearly from 2 to 0 during the iterations to model approaching the prey, \vec{r}_1 and \vec{r}_2 have random values in [0,1] range. To model the hunting behaviour of the grey wolves, the best three solutions are designated as alpha (α), beta (β), and delta (δ), respectively in every iteration, and they are used to update the positions of the other wolves including the omega (ω) by the following equations.

$$\vec{D}_\alpha = \left| \vec{C}_1 \cdot \vec{X}_\alpha - \vec{X} \right| \quad (11)$$

$$\vec{D}_\beta = \left| \vec{C}_2 \cdot \vec{X}_\beta - \vec{X} \right| \quad (12)$$

$$\vec{D}_\delta = \left| \vec{C}_3 \cdot \vec{X}_\delta - \vec{X} \right| \quad (13)$$

$$\vec{X}_1 = \vec{X}_\alpha - \vec{A}_1 \cdot \vec{D}_\alpha \quad (14)$$

$$\vec{X}_2 = \vec{X}_\beta - \vec{A}_2 \cdot \vec{D}_\beta \quad (15)$$

$$\vec{X}_3 = \vec{X}_\delta - \vec{A}_3 \cdot \vec{D}_\delta \quad (16)$$

$$\vec{X}(t+1) = \left(\vec{X}_1 + \vec{X}_2 + \vec{X}_3 \right) / 3 \quad (17)$$

Attacking the prey behaviour of the grey wolves depends on the \vec{A} value. If $|\vec{A}| < 1$, it means that the wolves must attack the prey. Otherwise, if $|\vec{A}| > 1$, it means that the wolves must search a fitter prey. The flowchart depicting the GWO algorithm is illustrated in Fig. 4 [13].

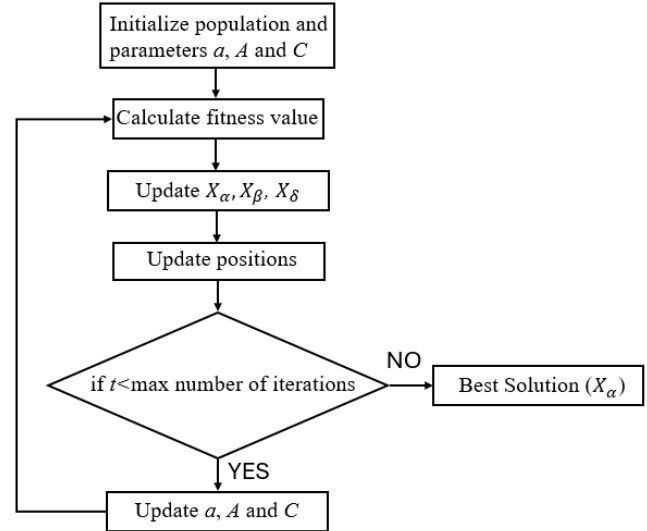


Fig. 4. The Flowchart of GWO Algorithm

B. Artificial Bee Colony Algorithm

Artificial Bee Colony (ABC) algorithm is an effective method for optimization problems. It models the foraging behavior of honeybees mathematically. There are three kinds of bees in the colony which are scout bees, employed bees, and onlooker bees. Scout bees search for undiscovered food sources by scanning the environment randomly. Employed bees exploit discovered food sources and share their position with onlooker bees. Onlooker bees go to the food sources for evaluating the quality of food [14].

In the ABC algorithm, the position of each food source corresponds to a potential solution of any optimization problem. The initial population is determined randomly in the search space. A selection process of food source is performed by onlooker bees by using the probability value given by Eq. (18) which depends on the fitness value of potential solutions.

$$p_i = \frac{fit_i}{\sum_{n=1}^{SN} fit_n} \quad (18)$$

Where fit_i is the fitness value of solution i , SN is the number of food sources. The fitness value corresponds to the quality of food source. To produce new solutions v_i in the neighborhood of x_i , the ABC uses the Eq. (19).

$$v_{ij} = x_{ij} + \phi_{ij} (x_{ij} - x_{kj}) \quad (19)$$

Where $k \in \{1, 2, \dots, SN\}$ and $j \in \{1, 2, \dots, D\}$ are the indexes. D indicates the dimensional size of the problem. Although k is selected randomly, it cannot be equal to i . ϕ_{ij} is a randomly determined number in the range of $[-1, 1]$. In this algorithm, if a position cannot be improved during a predetermined number of cycles, the employed bee abandons that food source and the scout bee discovers a new food source to replace with the abandoned one. The discovered new food sources are determined in the search space randomly. The flowchart depicting the ABC algorithm is shown in Fig. 5 [15].

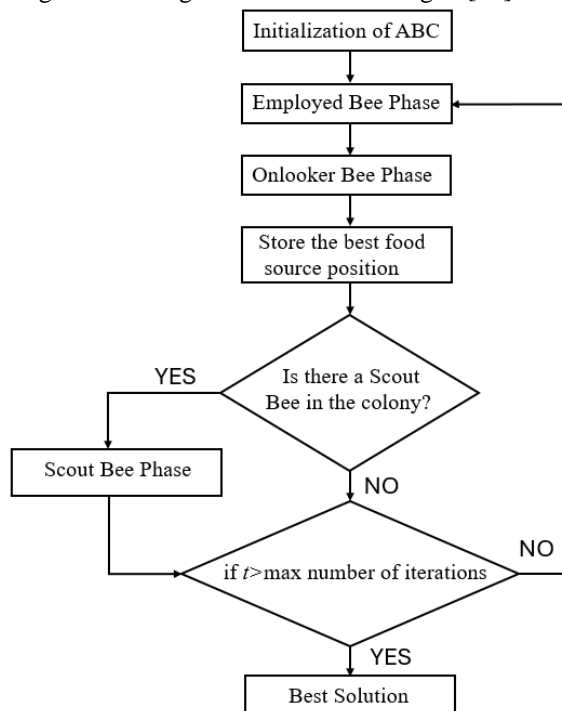


Fig. 5. The Flowchart of ABC Algorithm

C. Particle Swarm Optimization Algorithm

The Particle Swarm Optimization (PSO) algorithm stands as one of the most widely employed methods for optimization problems. Renowned for its ease of implementation, explorative capabilities, global convergence prowess, and robustness, PSO offers several advantages in tackling diverse optimization challenges. It models the behavior of birds to search the food [16].

In this algorithm the birds called particles have a position and a velocity. In every iteration, the fitness values of the particles are calculated due to the objective function. The best position

of each particle is called the local best position of associated particle. The best position between the positions of all particles is called the global best position. The new velocity and position of each particle are calculated using the following equations, incorporating both the local and global best positions:

$$v_i(t+1) = \omega v_i(t) + c_1 r_1 (p_i(t) - x_i(t)) + c_2 r_2 (g(t) - x_i(t)) \quad (20)$$

$$x_i(t+1) = x_i(t) + v_i(t+1) \quad (21)$$

Where t represents the current iteration, i denotes the current particle, x is the position of the particle, v is the velocity of the particle, r_1 and r_2 are random values in the range of $[0, 1]$, c_1 and c_2 are the constants influencing the particle's attraction to local and global best positions, p is the local best position of associated particle, g denotes the global best position and ω is the inertial weight. The PSO algorithm's flowchart is illustrated in Fig. 6 [17].

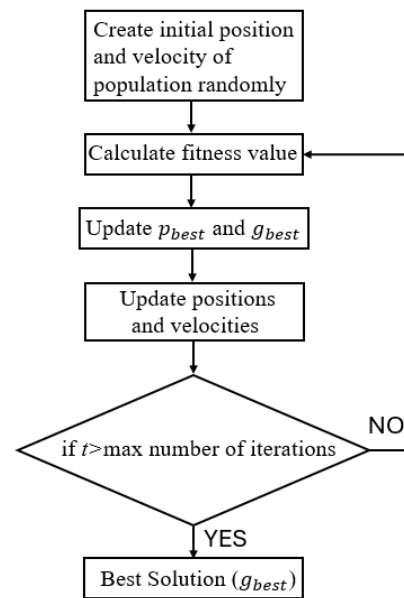


Fig. 6. The Flowchart of PSO Algorithm

IV. SIMULATION RESULTS

This paper employs metaheuristic algorithms such as PSO, GWO, and ABC to optimize the proportional and integral gains of PI controllers with the aim of enhancing the performance of FOC based IM. The model of the proposed method is illustrated in Fig. 7. Simulation results obtained using MATLAB are presented for three distinct operating conditions: no-load condition, speed change condition, and sudden load change condition. The parameters of the utilized induction motor are detailed in Table 2.

As the performance of FOC based IM is determined due to the three control loops (speed control loop and d - q component control loops of stator current), a multi-objective function is selected as given by Eq. (22) which consists of three terms

based on Sum of Absolute Errors (SAE) index, being related to minimizing errors (e_ω , e_{isd} and e_{isq}) belong to mentioned control loops. SAE function for any variable is given by Eq. (23).

$$f_{cost} = \omega_1 SAE_\omega + \omega_2 SAE_{i_{sd}} + \omega_3 SAE_{i_{sq}} \quad (22)$$

$$SAE_x = \sum_{i=1}^N |x_r(i) - x_m(i)| \quad (23)$$

TABLE II
INDUCTION MOTOR PARAMETERS

Parameter	Value
Power	5.5 kW
Number of pole (P)	4
Stator resistance (R_s)	1.28333 Ω
Rotor resistance (R_r)	0.9233 Ω
Stator inductance (L_s)	0.141833 H
Rotor inductance (L_r)	0.143033 H
Mutual inductance (L_m)	0.137333 H
Inertia torque (J)	0.1 kg m ²
Friction coefficient (f_d)	0.0028 Nm s/rad

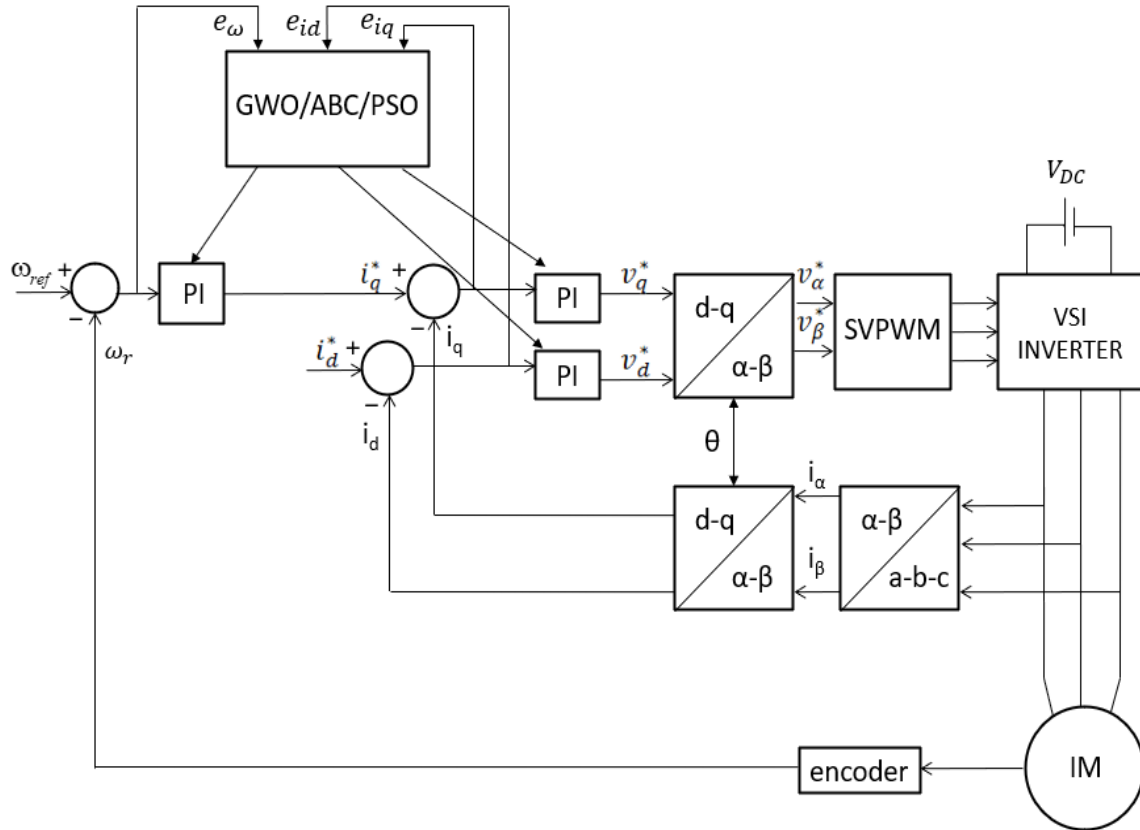


Fig. 7. Model of the Proposed Method

Where ω_1 , ω_2 and ω_3 are weighting factors used to equalize the three terms in the same magnitude order, x_r and x_m show the reference and measured values respectively for x variable, and N is the element number of x variable.

The obtained PI controller gains by used metaheuristic algorithms are given in Table 3.

TABLE III
OPTIMIZED CONTROLLER GAINS

Controller	K_p			K_i		
	PSO	ABC	GWO	PSO	ABC	GWO
Speed Controller	5.76	6.36	6.60	500	500	500
i_{sq} controller	3.99	4.19	4.21	1700	1672.5	1663.9
i_{sd} controller	6.95	6.90	6.83	1170.13	1144.8	1163.2

In the initial phase, the FOC based IM was operated under no-load conditions with a reference speed of 75 rad/s. The speed responses generated by the metaheuristic algorithms are depicted in Fig. 8-a. Table 4 presents the performances of the utilized metaheuristic methods. The motor speed reaches the desired speed during no-load operation after approximately 0.183 seconds with the GWO and ABC methods, while the corresponding time with the PSO method is about 0.198 seconds. The settling time with GWO and ABC is 0.015 seconds shorter than that with PSO. Although the maximum overshoot (2.05%) is observed with PSO, the minimum overshoot (1.15%) is observed with GWO. However, the rise times of the methods are identical. Therefore, the performance of the speed controller based on GWO is superior. Additionally, it can be asserted that the ABC method outperforms the PSO method.

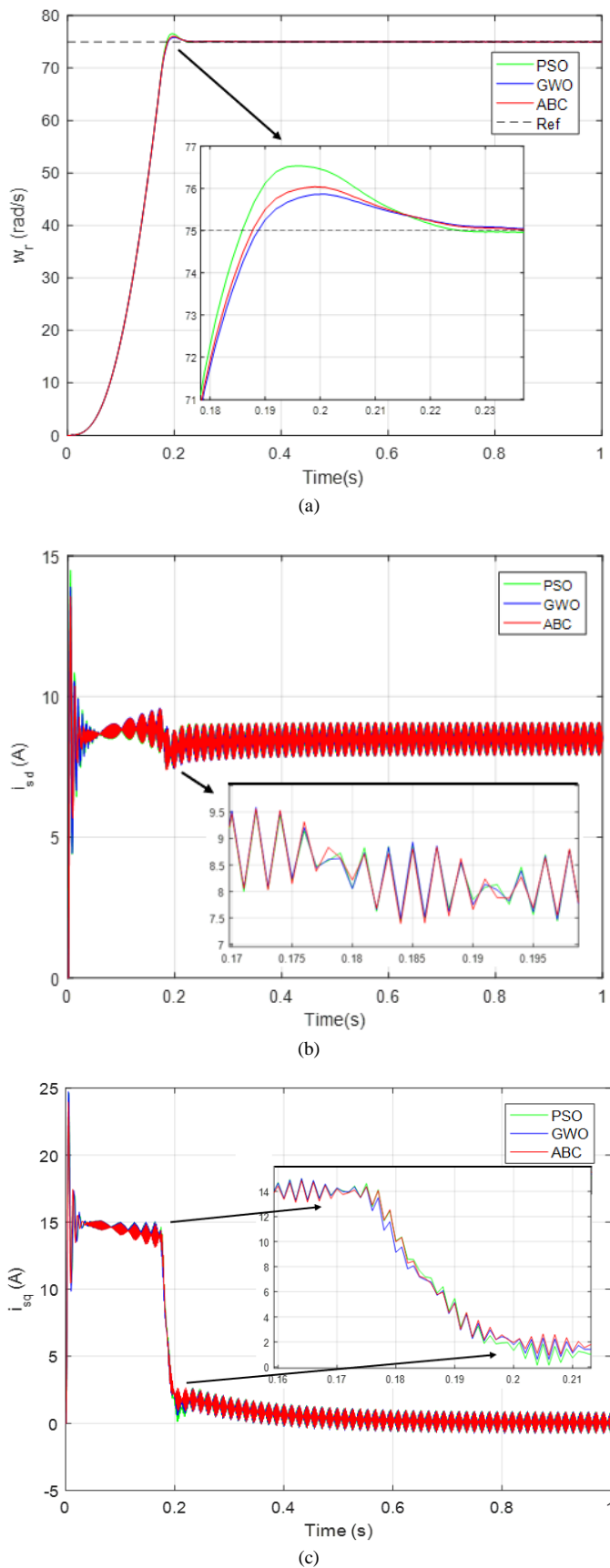


Fig. 8. No load condition test with a constant reference speed
 a) speed response b) i_{sd} current response c) i_{sq} current response

TABLE IV
 COMPARISON OF METHODS AT NO LOAD CONDITION

Algorithm	Rising time (s)	Settling time (s)	Maximum overshoot (%)
PSO	0.1024	0.1988	2.05
GWO	0.1024	0.1838	1.15
ABC	0.1024	0.1833	1.39

Under identical conditions, the performance of the i_{sd} current controller is depicted in Fig. 8-b, while the performance of the i_{sq} current controller is illustrated in Fig. 8-c. It is observed that, for both current controllers, the outcomes of the three optimization methods do not exhibit significant differences. Secondly, the performances of the methods are assessed under variable reference speed conditions at nominal load as depicted in Fig. 9. The reference speed is increased from 75 rad/sec to 150 rad/sec at the 1st second. Subsequently, at the 4th second, the reference speed is decreased from 150 rad/sec to -150 rad/sec to evaluate performance under reverse rotation conditions. Based on the speed response depicted in Fig. 9-a, it can be asserted that the control capability of the methods is effective under variable reference speed conditions, and the PI speed controller utilizing metaheuristic methods can effectively control the IM even when the rotation direction changes. This test comprises three transient cases, and in all instances, the GWO algorithm outperforms the other two methods. The minimum overshoot is 0.51% in the second transient case with GWO, while it is 0.64% in the third transient case using the same algorithm. On the other hand, the i_{sd} current response is depicted in Fig. 9-b. When the speed of the IM is increased from 75 rad/sec to 150 rad/sec, there is an increase in i_{sd} current ripple. According to the i_{sq} current response illustrated in Fig. 9-c, there is no significant difference among the three curves, even in transient conditions. As the speed of the IM increases, i_{sq} current ripple also increases.

Finally, a sudden load change test was conducted using the methods employed for FOC based IM. The load torque was increased from 0 Nm to 25 Nm in the 1st second and decreased from 25 Nm to 10 Nm in the 2nd second. Fig. 10-a illustrates the speed response of the IM. In the 1st second, the IM experiences a decrease in speed due to an increase in load torque, reaching the reference speed after a brief transient period. By the 2nd second, the IM speed increases due to a reduced load, stabilizing at the desired speed. Consequently, successful speed control is achieved by all methods. During sudden load changes, it is observed that the speed response is less influenced by the GWO and ABC algorithms. In the second transient case, following a load disturbance, the IM speed reaches the reference speed after 0.084 seconds and 0.088 seconds with ABC and GWO, respectively, while PSO achieves this in 0.074 seconds. In the third transient case, these times are 0.081 seconds, 0.085 seconds, and 0.074 seconds for ABC, GWO, and PSO, respectively. Hence, it can be asserted that the settling time in transient cases caused by load disturbances is minimized with PSO.

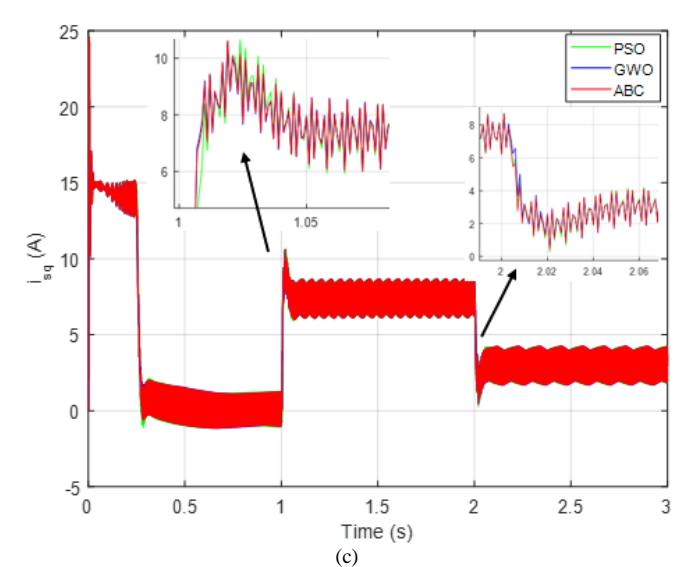
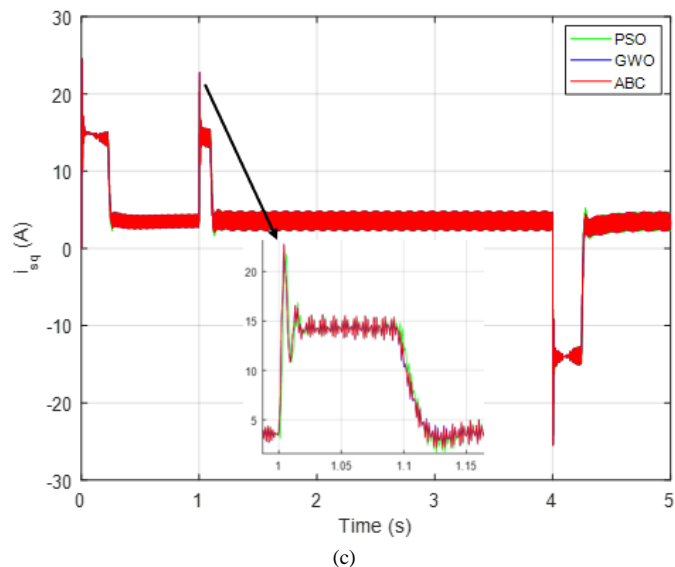
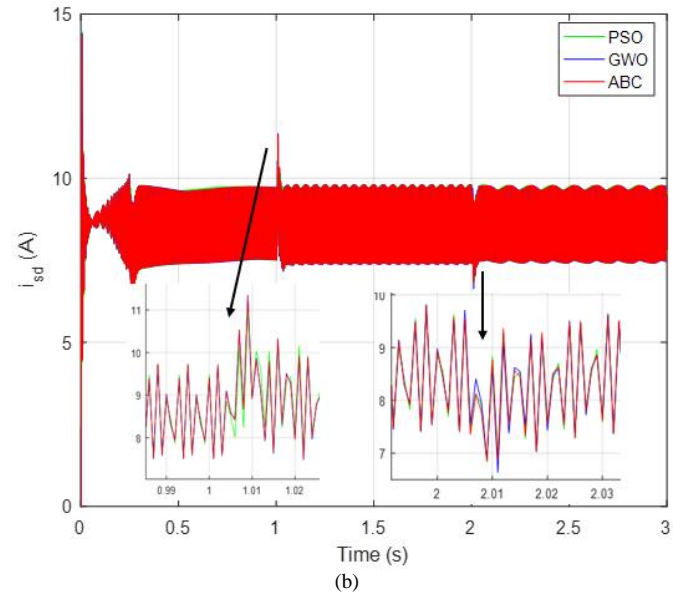
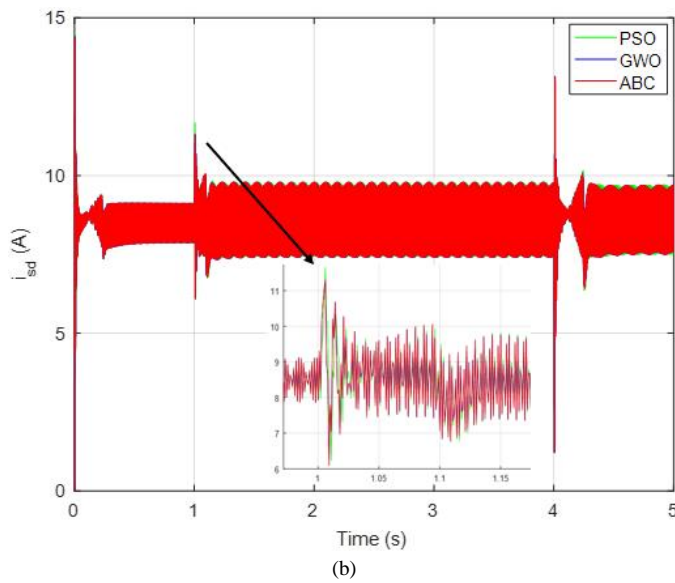
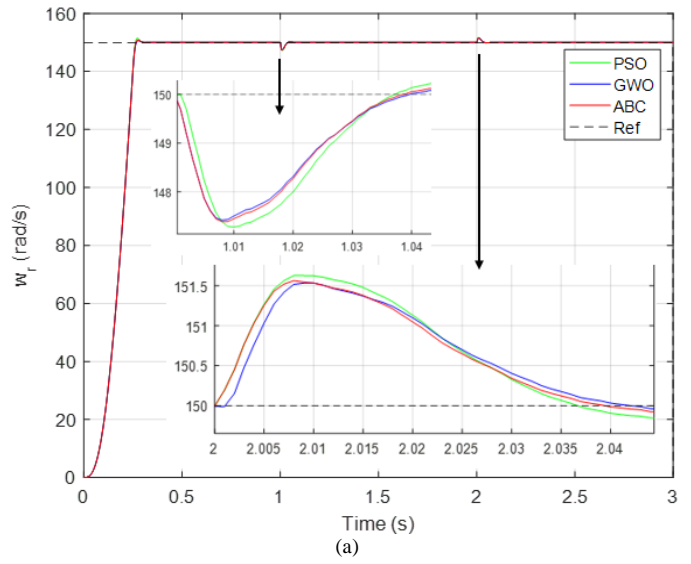
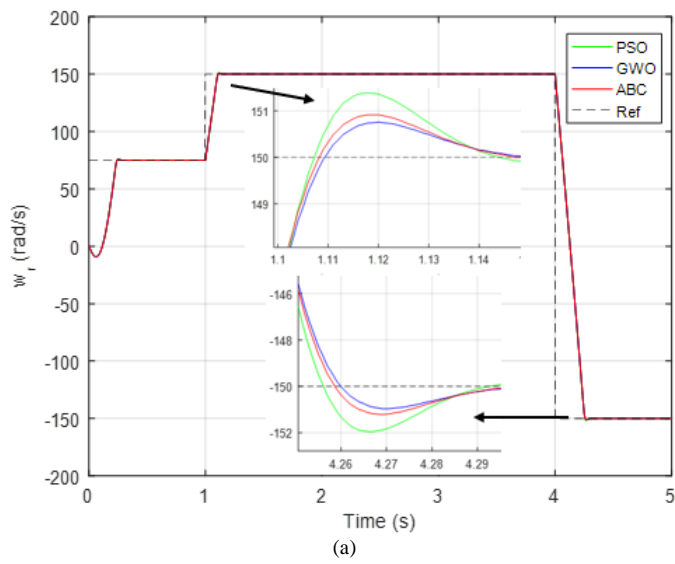


Fig. 9. Variable reference speed test under nominal operating condition
 a) speed response b) i_{sd} current response c) i_{sq} current response

Fig. 10. Sudden load change test
 a) speed response b) i_{sd} current response c) i_{sq} current response

The d - q current responses depicted by Figures 10-b and 10-c are nearly identical across all metaheuristic methods. Analyzing the steady-state values reveals that the i_{sd} current remains relatively stable, while the i_{sq} current undergoes significant changes. This is attributed to the impact of increased load torque on electromagnetic torque. In the FOC of the IM, the i_{sq} current governs the electromagnetic torque, leading to an increase in i_{sq} current with higher load torque, as illustrated in Fig. 10-c. Consequently, a decrease in load torque results in a lower i_{sq} current.

Fig. 11 illustrates the convergence speed of the applied metaheuristic algorithms. Notably, the ABC algorithm achieves optimal convergence by the 34th iteration, while the GWO algorithm converges by the 72nd iteration and PSO converges by the 41st iteration. Consequently, it can be concluded that the ABC algorithm exhibits the best convergence speed, with GWO being the least efficient in this regard.

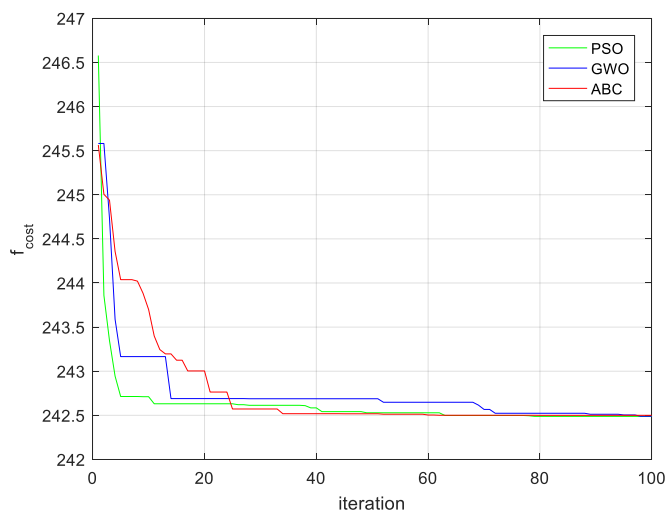


Fig. 11. Convergence speed of metaheuristic algorithms

Table 5 is given for a detail analysis of methods comparatively in terms of speed control performance by the transient response parameters and, convergence.

TABLE V
COMPARISON OF METHODS IN TERMS OF CONTROL PERFORMANCE AND CONVERGENCE

Condition	Parameters	PSO	GWO	ABC
Constant reference speed for no load operation	Rising time	same	same	Same
	Settling time	highest	same	Same
	Overshoot	highest	lowest	-
Variable reference speed for nominal load condition	Settling time	same	same	Same
	Overshoot	highest	lowest	-
Sudden load change test	Instant dropping in the speed	highest	same	Same
	Settling time	lowest	highest	-
Any condition	Convergence speed	-	slowest	Fastest

V. CONCLUSION

In this paper, the results of FOC based IM realized by optimization of PI controllers using the metaheuristic algorithms (PSO, GWO and ABC) are presented comparatively. The assessment is conducted based on the responses of the IM under three operational conditions: no-load, speed change at nominal load, and sudden load change. Under no-load and speed change conditions, the GWO algorithm yields the best dynamic performance, particularly in terms of maximum overshoot. Despite a change in the rotation direction during the speed change test, the control capability of the utilized controllers remains commendable. However, the d - q current responses are nearly identical across all methods. During load change conditions, the speed response is less impacted by the GWO and ABC algorithms due to load disturbances. Nevertheless, the settling time in transient cases is minimized with PSO. Consequently, the optimization of PI controllers in FOC-based IM is successfully accomplished through the application of metaheuristic methods. The findings indicate that the dynamic performance with the GWO algorithm surpasses that of PSO and ABC in FOC-based IM, although the convergence speed of the GWO algorithm to optimal results is slower compared to PSO and ABC algorithms.

ACKNOWLEDGEMENT

This paper was derived from the thesis called “Field oriented control of induction motor by metaheuristic methods” which is realized in Karabuk University in 2023.

REFERENCES

- [1] I. Ferdiansyah, M.R. Rusli, B. Praharsena, H. Toar, E. Purwanto. "Speed control of three phase induction motor using indirect field oriented control based on real-time control system." 10th International Conference on Information Technology and Electrical Engineering (ICITEE), Bali, Indonesia, 2018.
- [2] A.Y. Yousef, S.M. Abdelmaksoud. "Review on field oriented control of induction motor." International Journal for Research in Emerging Science and Technology, vol. 2, 7, 2015, pp 5–16.
- [3] T. Banerjee, S. Choudhuri, J. Bera, A. Maity. "Off-line optimization of PI and PID controller for a vector controlled induction motor drive using PSO." 6th International Conference on Electrical and Computer Engineering (ICECE), Dhaka, Bangladesh, 2010.
- [4] C. Lai, K. Peng, G. Cao. "Vector control of induction motor based on online identification and ant colony optimization." 2nd International Conference on Industrial and Information Systems, Dalian, China, 2010.
- [5] M.B.B. Sharifian, S. Galvani, M.B. Kouhshahi. "Torque fluctuations reducing in a vector-controlled induction motor drive by PI controller tuning using particle swarm optimization." International Conference on Electrical Machines and Systems, Beijing, China, 2011.
- [6] M.A. Hannan, J.A. Ali, A. Mohamed, U.A.U. Amirulddin, N.M.L. Tan, M. N. Uddin. "Quantum-behaved lightning search algorithm to improve indirect field-oriented Fuzzy-PI control for IM drive." IEEE Industry Applications Society Annual Meeting, Cincinnati, OH, USA, 2017.
- [7] F.A. Hasan, A.T. Humod, L.J. Rashad. "Robust decoupled controller of induction motor by combining PSO and Kharitonov's theorem." Engineering Science and Technology, an International Journal, vol. 23, 6, 2020, pp 1415–1424.
- [8] A. Raj, Y.A. Khan, V. Verma. "Comparative evaluation of PSO, TLBO, and JAYA based adaptive PI and FOPI controllers for vector controlled induction motor drive." IEEE 4th International Conference

- on Computing, Power and Communication Technologies (GUCON), Kuala Lumpur, Malaysia, 2021.
- [9] M.M. Hasan, M.S. Hussain, M.S. Rana, M.H.K. Roni. "Population extremal optimization based 2-DOF control strategy for field oriented control of induction motor." 3rd International Conference on Electrical & Electronic Engineering (ICEEE), Rajshahi, Bangladesh, 2021.
- [10] M.J. Cheerangal, A.K. Jain, A. Das. "Control of rotor field-oriented induction motor drive during input supply voltage sag." IEEE Journal of Emerging and Selected Topics in Power Electronics, vol. 9. 3, 2021, pp 2789-2796.
- [11] R. Rai, S. Shukla, B. Singh. "Sensorless field oriented SMCC based integral sliding mode for solar PV based induction motor drive for water pumping." IEEE Transactions on Industry Applications, vol. 56. 5, 2020, pp 5056-5064.
- [12] S. Mirjalili, S.M. Mirjalili, A. Lewis. "Grey wolf optimizer." Advances in Engineering Software, vol. 69, 2014, pp 46-61.
- [13] M.A. Şen, M. Kalyoncu. "Optimal tuning of PID controller using grey wolf optimizer algorithm for quadruped robot." Balkan Journal of Electrical & Computer Engineering, vol. 6. 1, 2018, pp 29-35.
- [14] D. Karaboga, B. Basturk. "On the performance of artificial bee colony (ABC) algorithm." Applied Soft Computing, vol. 8, 2008, pp 687-697.
- [15] D. Karaboga, C. Ozturk. "A novel clustering approach: Artificial Bee Colony (ABC) algorithm." Applied Soft Computing, vol. 11, 2011, pp 652-657.
- [16] J. Kennedy, R. Eberhart. "Particle swarm optimization." International Conference on Neural Networks, Perth, WA, Australia, 1995.
- [17] A. Iqbal, G.K. Singh. "PSO based controlled six-phase grid connected induction generator for wind energy generation." CES Transactions on Electrical Machines and Systems, vol. 5. 1, 2021, pp 41-49.
- [18] E. Ebrahim. "Artificial bee colony-based design of optimal on-line self-tuning PID-controller fed AC drives." International Journal of Engineering Research, vol. 3. 12, 2015, pp 807-811.
- [19] S. R. Ahamed, J. N. Chandra Sekhar, D. P. Reddy P. "Speed control of induction motor by using intelligence techniques." International Journal of Engineering Research and Applications, vol. 5. 1, 2015, pp 130-135.
- [20] T. G. Workineh, Y. B. Jember, A. T. Kassie. "Evaluation of intelligent PPI controller for the performance enhancement of speed control of induction motor." Scientific African, vol. 22, 2023, pp 1-16.
- [21] P. J. Shaija, A. E. Daniel. "Optimal tuning of PI controllers for IM drive using GWO and TLBO algorithms." 5th International Conference on Electrical, Computer and Communication Technologies (ICECCT), Erode, India, 2023.
- [22] B. Çavuş, M. Aktaş. "MPC-based flux weakening control for induction motor drive with DTC for electric vehicles." IEEE Transactions on Power Electronics, vol. 38. 4, 2023, pp 4430-4439.
- [23] K. V. B. Singh. "Optimized reference points based vector control of induction motor drive for electric vehicle." IEEE Transactions on Industry Applications, vol. 59. 4, 2023, pp 4164-4174.
- [24] A. Benhammou, H. Tedjini, Y. Guettaf, M. A. Soumeur, M. A. Hartani, O. Hafsi, A. Benabdelkader. "Exploitation of vehicle's kinetic energy in power management of tow -wheel drive electric vehicles based on ANFIS DTC-SVM comparative study." International Journal of Hydrogen Energy, vol. 46, 2021, pp 27758-2769.
- [25] H. Sathishkumar, S. S. Parthasarathy. "A novel neuro-fuzzy controller for vector controlled induction motor drive." Energy Procedia, vol. 138, 2017, pp 698-703.
- [26] H. Sathishkumar, S. S. Parthasarathy. "A novel neural network intelligent controller for vector controlled induction motor drive." Energy Procedia, vol. 138, 2017, pp 692-697.
- [27] Z. Tir, O. P. Malik, A. M. Eltamaly. "Fuzzy logic based speed control of indirect field oriented controlled double star induction motors connected in parallel to a single six-phase inverter supply." Electric Power Systems Research, vol. 134, 2016, pp 126-133.
- [28] S. Pravalika, J. N. Chandra sekhar, D. P. Reddy P. "Optimization of Speed Control of Induction Motor Using Self Tuned PI plus Fuzzy Hybrid Controller." International Journal of Emerging Technology and Advanced Engineering, vol. 5. 1, 2015, pp 258-262.
- [29] S. P J, A. E. Daniel. "Robust sliding mode control strategy applied to IFOC induction motor drive." 4th International Conference on Electrical, Computer and Communication Technologies (ICECCT), Erode, India, 2021.
- [30] A. Zaafouri, C. B. Regaya, H. B. Azza, A. Châari. "DSP-based adaptive backstepping using the tracking errors for high-performance sensorless

speed control of induction motor drive." ISA Transactions, vol. 60, 2016, pp 333-347.

BIOGRAPHIES

HERSH HASAN TAHA AL-DAWOODI joined the College of Engineering, Department of Electrical at Tikrit University in 2008. He also received the M.S. degree in electrical and electronics engineering from Karabuk University, Karabuk, Turkey, in 2023. His research interests include control of synchronize generator, PV system control, power factor correction.



HILMI AYGUN received the B.S. degree in electrical and electronics engineering from Kirikkale University, Kirikkale, in 2007. He also received the M.S. and Ph.D. degrees in electrical and electronics engineering from Karabuk University, Karabuk, Turkey, in 2011 and 2019, respectively. From 2009 to 2019, he was a Research Assistant at Karabuk University. Since 2019, he has been an Assistant Professor with the Mechatronics Engineering Department, Karabuk University. His research interests include control of electrical machines, electric vehicles, optimization by metaheuristic algorithms.



Publication Ethics

The journal publishes original papers in the extensive field of Electrical-electronics and Computer engineering. To that end, it is essential that all who participate in producing the journal conduct themselves as authors, reviewers, editors, and publishers in accord with the highest level of professional ethics and standards. Plagiarism or self-plagiarism constitutes unethical scientific behavior and is never acceptable.

By submitting a manuscript to this journal, each author explicitly confirms that the manuscript meets the highest ethical standards for authors and coauthors

The undersigned hereby assign(s) to *Balkan Journal of Electrical & Computer Engineering* (BAJECE) copyright ownership in the above Paper, effective if and when the Paper is accepted for publication by BAJECE and to the extent transferable under applicable national law. This assignment gives BAJECE the right to register copyright to the Paper in its name as claimant and to publish the Paper in any print or electronic medium.

Authors, or their employers in the case of works made for hire, retain the following rights:

1. All proprietary rights other than copyright, including patent rights.
2. The right to make and distribute copies of the Paper for internal purposes.
3. The right to use the material for lecture or classroom purposes.
4. The right to prepare derivative publications based on the Paper, including books or book chapters, journal papers, and magazine articles, provided that publication of a derivative work occurs subsequent to the official date of publication by BAJECE.
5. The right to post an author-prepared version or an official version (preferred version) of the published paper on an internal or external server controlled exclusively by the author/employer, provided that (a) such posting is noncommercial in nature and the paper is made available to users without charge; (b) a copyright notice and full citation appear with the paper, and (c) a link to BAJECE's official online version of the abstract is provided using the DOI (Document Object Identifier) link.



ISSN: 2147- 284X
Year: September 2024
Volume: 12
Issue: 3

CONTENTS

Research Article	Onur Akar; Estimation of the Effect of Electric Vehicles on the Aging of Distribution Transformers Using Fuzzy Logic, 199-205
Research Article	Zeynep Özpolat, Özal Yıldırım, Murat Karabatak; The Effect of Linear Discriminant Analysis and Quantum Feature Maps on QSVM Performance for Obesity Diagnosis, 206-213
Research Article	Muhammed Cihad Arslanoğlu, Hüseyin Acar, Abdülkadir Albayrak; Face Expression Recognition via transformer-based classification models, 214-223
Research Article	Nezihe Yıldırım; Hardware Implementation of Fully Controlled Bridge Rectifier with Rapid Control Prototyping Approach, 224-230
Research Article	Uğur Yeşilyurt; Multipath Characteristics of Orbital Angular Momentum Vortex Electromagnetic Radio Waves Over an Infinite Ground Plane, 231-239
Research Article	Ferdi Özbilgin, Hüseyin Çalık, Mehmet Cem Dikbaş; Average Wind Speed Prediction in Giresun-Kümbet Plateau Region with Artificial Neural Networks, 240-246
Research Article	Ercan Aykut, Ihsan Alshuraida; Grid Integration Strategies for Optimizing Renewable Energy Deployment and Grid Resilience, 247-254
Research Article	Remzi Göçmen, Musa Çıbuk, Erdal Akin; Comparative Analysis of Deep Learning Algorithms in Fire Detection, 255-261
Research Article	Hersh Hasan Taha Al-dawoodi, Hilmi Aygün; A Comparison Study of Some Metaheuristic Methods for Field Oriented Control Based Induction Motors, 262-272

BALKAN JOURNAL OF ELECTRICAL & COMPUTER ENGINEERING

(An International Peer Reviewed, Indexed and Open Access Journal)

Contact

Batman University
Department of Electrical-Electronics Engineering
Bati Raman Campus Batman-Turkey

Web: <https://dergipark.org.tr/en/pub/bajece>
<http://www.bajece.com>
e-mail: bajece@hotmail.com

